# Annual Progress Report for the LIBRA Light Ion Beam Fusion Reactor Project for the Period 1 October 1984 – 31 December 1985

B. Badger, T.J. Bartel, M.L. Corradini, R.L. Engelstad, B.P. Goel, G.L. Kulcinski, E.G. Lovell, G.A. Moses, R.R. Peterson, M.E. Sawan, I.N. Sviatoslavsky and J.J. Watrous

December 1985

FPA-85-5

FUSION POWER ASSOCIATES

2 Professional Drive, Suite 248
Gaithersburg, Maryland 20879
(301) 258-0545

1500 Engineering Drive
Madison, Wisconsin 53706
(608) 263-2308

# ANNUAL PROGRESS REPORT FOR THE LIBRA LIGHT ION BEAM FUSION REACTOR PROJECT FOR THE PERIOD 1 OCTOBER 1984 - 31 DECEMBER 1985

B. Badger, T.J. Bartel, M.L. Corradini, R.L. Engelstad, B.P. Goel, G.L. Kulcinski, E.G. Lovell, G.A. Moses, R.R. Peterson, M.E. Sawan, I.N. Sviatoslavsky, J.J. Watrous

Fusion Power Associates
6519 Grand Teton Plaza
Madison, WI 53719

December 1985

FPA-85-5

## 1. INTRODUCTION

This is a progress report for work done between October 1, 1984 and December 31, 1985 by Fusion Power Associates (FPA) under contract to Kernforschungszentrum Karlsruhe (KfK). The purpose of this work has been to study issues related to Light Ion Beam Fusion. The work can be broken down into three areas: computer simulation of light ion deposition in thin targets, improvements to the Z-PINCH computer code, and continued work on the LIBRA light ion fusion power plant design concept. A list of publications and presentations related to this work in 1985 is given in Table 1.1.

Computer simulations of the deposition of light ions in matter have been performed for parameters that are achievable by a future upgrade of the KALIF light ion accelerator at KfK. This work has been done in collaboration with Dr. Balbir P. Goel of KfK, who has been visiting the University of Wisconsin (UW) and FPA during the period April 1, 1985 to January 15, 1986. In an effort to better understand the physics of ion deposition and of the heated material, results from the MEDUSA code, brought to Madison by Dr. Goel, and PHD-IV, a UW code, have been compared with each other and with results from the Naval Research Laboratory (NRL).

The Z-PINCH computer code simulates the behavior of the plasma channels that have been proposed as a means of propagating ion beams from ion diodes to fusion targets. Improvements have been made to the code that make it easier to define the external driving circuit parameters and the injected ion beam, and that include the channels themselves as elements in the external circuit. Sample calculations have been completed that show the effects of these improvements.

The LIBRA design concept has undergone some modification during 1985. The main parameters, listed in Table 1.2, are unchanged from 1984. However, the geometry of the design has changed, as have some of the major details. Pulse Sciences, Inc. (PSI) has provided KfK with a new design of the pulsed power machinery for LIBRA, which has lead to the new design and layout shown in Fig. 1.1. Also, choice of ion species has been changed to 20 MeV $D^+$. The distance from the target to the first row of INPORT tubes has been reduced to 3 meters from 5 meters, which has allowed the distance from the diodes to the target to be lowered to 6 meters from about 11 meters. The reduction in the size of the reactor cavity has allowed the tritium breeding ratio to be increased to 1.16 from 1.09. The dynamics of the target generated fireball and the mechanical response of the INPORT tubes have been reconsidered for the new geometry, as has the behavior of the plasma channels. In general, the design concept has been improved by these modifications.

Table 1.1. Publications and Presentations Related to LIBRA

1. L. Pong, M.L. Corradini, R.R. Peterson and G.A. Moses, "Liquid Metal Condensation in the Cavity of the HIBALL Heavy Ion Fusion Reactor," Fusion Power Associates Report FPA-85-1, and Nucl. Engr. and Design/Fusion 3, 47 (1985).

2. R.L. Engelstad and E.G. Lovell, "Vibration Analysis of LIBRA INPORTs," Fusion Power Associates Report FPA-85-2 (February, 1985) [presented at Sixth Topical Meeting on the Technology of Fusion Energy, San Francisco, CA, 3-7 March 1985].

3. J.J. Watrous, G.A. Moses and R.R. Peterson, "Z-PINCH - A Multifrequency Radiative Transfer Magnetohydrodynamics Computer Code," Fusion Power Associates Report FPA-85-3 (March, 1985).

4. B.P. Goel, G.A. Moses and R.R. Peterson, "Computer Simulation of Light Ion Energy Deposition Experiments on KALIF," 1985 Meeting of the Division of Plasma Physics of the American Physical Society, San Diego, CA, 4-8 November 1985.

5. B.P. Goel, R.R. Peterson and G.A. Moses, "Pre-Experimental Analysis of Proton Stopping Measurements in Hot Aluminum Plasmas on KALIF," Fusion Power Associates Report FPA-86-1 (January, 1986).

6. R.L. Engelstad and E.G. Lovell, "Nonlinear Vibration and Dynamic Instability of LIBRA INPORT Tubes," Fusion Power Associates Report FPA-86-2 (January, 1986).

Table 1.2. Major Parameters for LIBRA

| | |
|---|---|
| Reactor type | Demonstration, electricity production |
| Cost goal | Less than $10^9$ $ |
| Ion accelerator type | Helia pulsed power/diode |
| First wall protection | HIBALL-like INPORT units |
| Ion propagation mode | Preformed channels |
| Target yield | 320 MJ |
| Power on target | 240 TW |
| Energy on target | 4 MJ |
| Target gain | 80 |
| Repetition rate | 1.5 Hz |
| Fusion power | 480 MW |
| Thermal power | 612 MWe |
| Gross electrical power | 245 MW |
| Net electrical power | 215 MW |

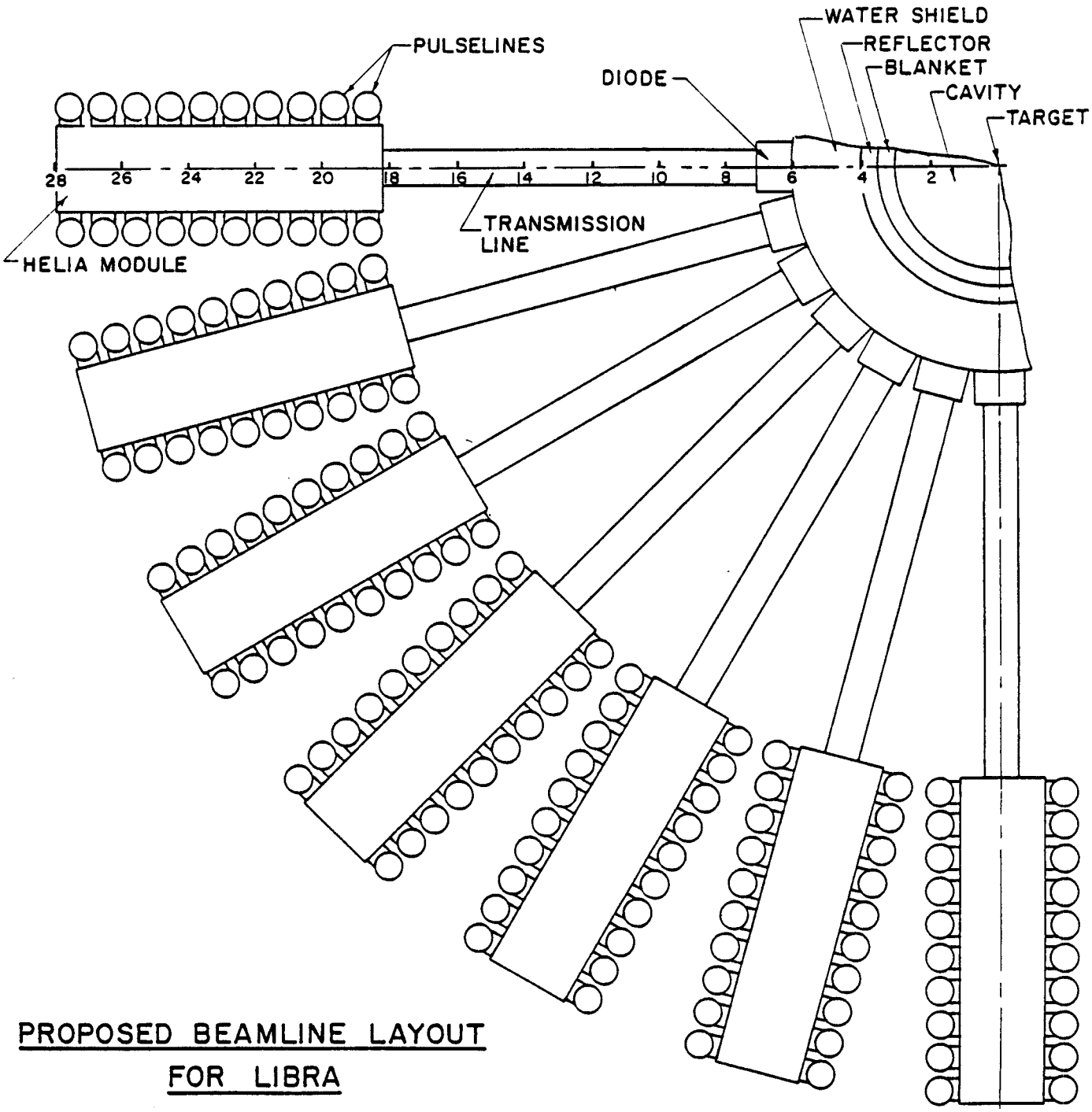


Fig. 1.1. Overhead view of LIBRA layout.

## 2. ION STOPPING CALCULATIONS

Ion beam-target interaction is a key issue for the successful design of inertial confinement fusion (ICF) targets. The particle range must be known to an accuracy of better than 10% to optimize target designs. Too short a range will cause a larger amount of material to implode, thereby reducing the implosion velocity. On the other hand if the range is larger than that computed by target design codes the beam will penetrate deeper into the target, reducing the amount of pusher and preheating the fuel. A fair amount of theoretical and experimental work is required to achieve an adequate understanding of energy deposition of intense particle beams in hot plasma. Experimentally the work is rendered difficult by the fact that the intense particle beam whose stopping power is to be measured also is the source of energy heating the matter. The heated matter expands and during the course of beam deposition considerable hydrodynamic motion occurs. Hence, a measurement of the stopping power of intense ion beams requires a simultaneous analysis of the transient thermodynamical behavior of the target.

At the nuclear research center Karlsruhe a pulse power machine (KALIF) has been installed. Using a 6 cm pinch reflex diode, a 1.5 MeV proton beam has been focused to 0.3 $TW/cm^2$ on a target.[1] A peak power of 0.7 TW was observed. Higher power densities may be obtained in the near future by optimizing the diodes and improving the machine performance. The ion beam pulse is about 60 ns long (FWHM). With these characteristics KALIF can serve as a suitable tool to measure energy deposition of light ions in the temperature range of a few 10's of eV. We have examined the range in which meaningful dE/dx measurements can be performed on KALIF with its present operating characteristics. Figure 2.1 sketches an experiment being proposed for the

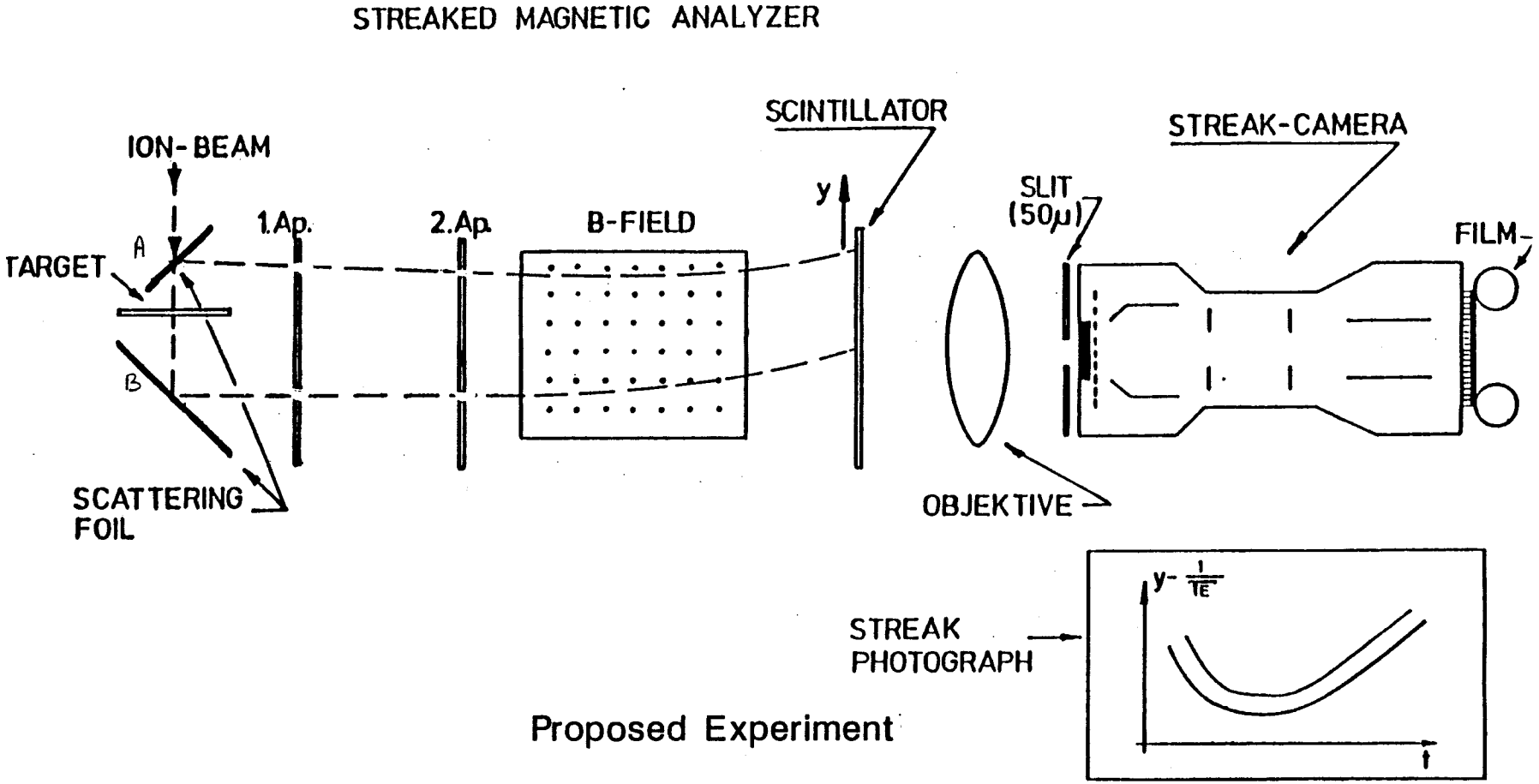


Fig. 2.1. Sketch of dE/dx experiment on KALIF.

dE/dx measurement at KALIF. The ion beam comes from the top. The scattering foil "A" will absorb the carbon ions and scatter a part of the beam into the magnetic analyzer. After undergoing interaction in the target, scattering foil "B" scatters the beam again into the analyzing magnets. Apertures 1 and 2 collimate the beam. The scintillation signals are registered in a streak camera. This arrangement would allow the measurement of both incoming and outgoing beam energy. We compare the results of our codes with recently published results from NRL.[2] Since the ion coupling model and the hydrodynamics treatment are different in the NRL calculations from our own codes, this comparison serves as a good check on the soundness of our results.

## 2.1 Hydrodynamics Model

Calculations are performed using two different Lagrangian hydrodynamics codes: MEDUSA-KA[3-5] and PHD-IV.[6,7] Details of these codes have been reported previously. In the following only a brief summary of the main features relevant to the present work is given.

Both of the programs are one-dimensional, Lagrangian hydrodynamics codes written initially to study laser driven ICF implosions. The basic equations solved are the one fluid-two temperature equations of plasma hydrodynamics.

$$\frac{\partial u}{\partial t} = -\frac{1}{\rho}\nabla P \tag{2.1}$$

$$\rho C_{ve}\frac{\partial T_e}{\partial t} = \nabla k_e \nabla T_e - P_e(\nabla\cdot u) - \omega_{ei}(T_e - T_i) + S_e \tag{2.2}$$

$$\rho C_{vi}\frac{\partial T_i}{\partial t} = \nabla k_i \nabla T_i - P_i(\nabla\cdot u) + \omega_{ei}(T_e - T_i) + S_i \tag{2.3}$$

$u$ is the fluid velocity, $\rho$ is the mass density, $P = P_e + P_i$ is the pressure,

$C_v$ is the specific heat, T is the temperature, subscript i denotes ions and e denotes electrons. The conductivity coefficients $K_e$ and $K_i$ and electron-ion equilibration coefficient $\omega_{ei}$ are taken from Spitzer.[8] The source terms $S_e$ and $S_i$ are, in the present context, the energy deposited by the ion beam to the plasma. Ions and electrons can have different temperatures but both the fluids travel with the same speed so that no charge separation takes place and the generation of electric fields is avoided. PHD-IV can treat radiation as a third temperature or can use a multigroup transport of radiation.[7] The radiation transport coefficients are taken from the Los Alamos opacity library.[9]

The two populations (electrons and ions) are governed by their own pressures. For ions it is deemed sufficient to use an ideal gas equation of state. Electrons, however, require a more complex treatment. The code PHD-IV reads the equation of state data from the SESAME library.[10] In MEDUSA-KA an analytical equation of state is used. This has the form

$$P_e(\rho,T) = P_c(\rho) + P_B(\rho,T) + P_f(\rho,T) \ .$$

$P_c$ denotes cold or zero temperature curve, $P_B(\rho,T)$ and $P_f(\rho,T)$ are the components due to bound and free electrons in the plasma. In the code different options to calculate $P_e$ are available.[10] For the present calculations the so-called corrected Thomas-Fermi equation of state is used.

The correction to the Thomas-Fermi equation of state is obtained by an expansion of the Hartree-Fock equation in series of progressively higher order quantum terms. Retaining the first order quantum term yields the corrected Thomas-Fermi equation of state.[12] The correction term has the same form as

obtained by including the exchange forces. Thus, first order quantum effects and exchange forces can be accounted for by using the same term multiplying it by an appropriate numerical factor. The zero temperature part of this term can be separated from the temperature dependent part. For the sake of simplicity MEDUSA-KA uses only the zero temperature part of the correction term.[11]

In Fig. 2.2, the equation of state data for aluminum as calculated in MEDUSA-KA is compared with the SESAME library. Since the tabulated SESAME library data is used in PHD-IV both codes use essentially comparable EOS data.

## 2.2 Beam Target Coupling Model

The source terms in Eqs. (2.2) and (2.3) are determined by the amount of energy deposited in the plasma by the ion beam interaction. They depend on the beam energy and on the temperature and density of the target. There is a great deal of information available on the ion stopping in cold material.[12] Less is known about the stopping of charged particles in hot dense media. Only recently have experiments been performed to measure the stopping power of protons in hot plasma.[14,15] Enhancement of the stopping power in hot plasma has been observed.

A fair amount of theoretical work has been done to calculate stopping of charged particles in hot plasma.[16-22] All calculations of stopping power treat bound and free electrons separately. Others have suggested that this description may not be a valid assumption in dense plasmas.[23]

In a general form the stopping power can be written as:

$$\frac{dE}{dx} = \left[\frac{dE}{dx}\right]_{bound} + \left[\frac{dE}{dx}\right]_{free} + \left[\frac{dE}{dx}\right]_{ions} .$$

The ion stopping is important only at low energies or in low atomic weight ma-

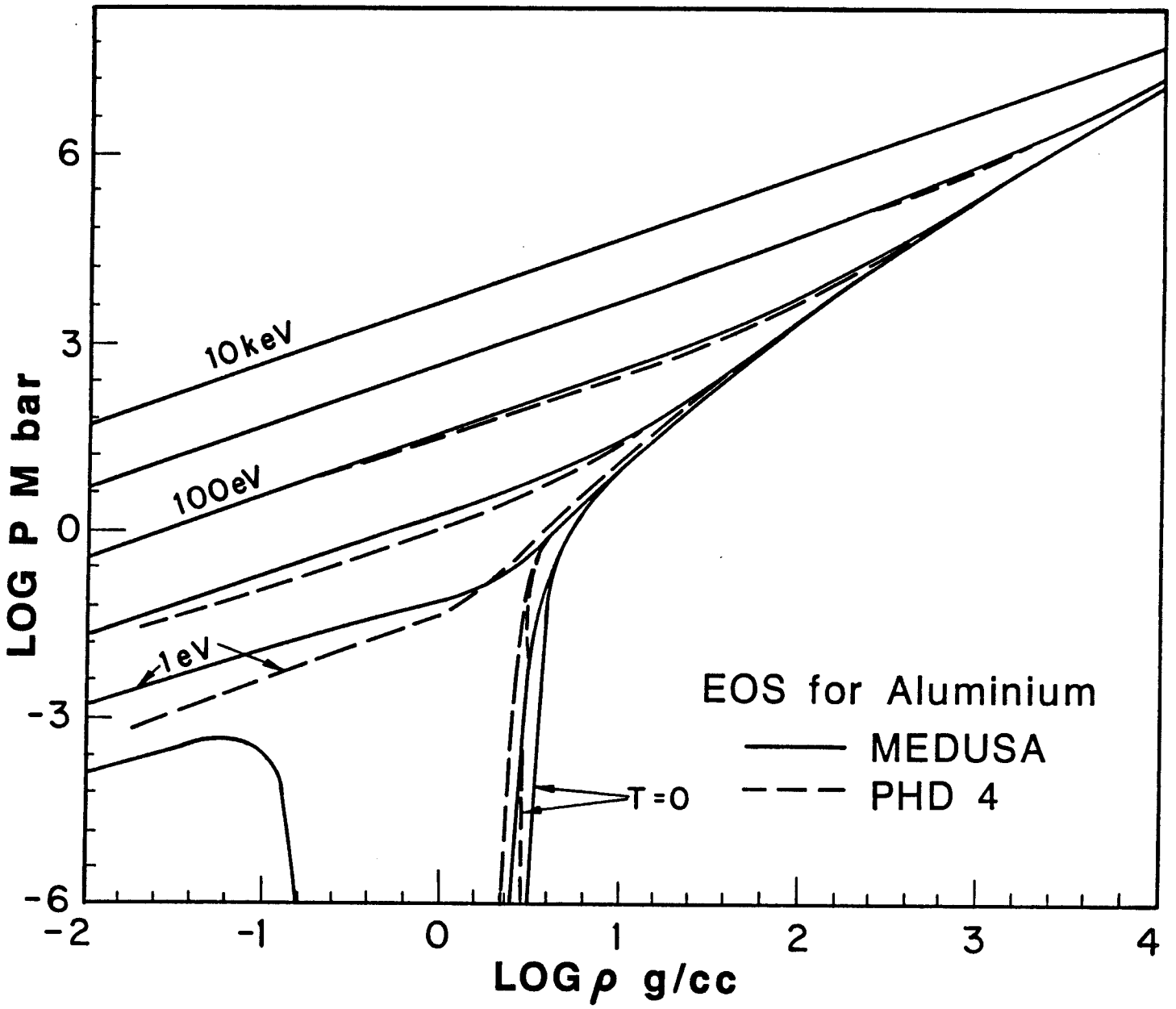


Fig. 2.2. Comparison of aluminum equations-of-state as calculated in MEDUSA-KA and tabulated in the SESAME tables.

terials. The calculation for the bound electron stopping power is done using Bethe's theory.[24] Bethe's equation can be written as

$$\frac{dE}{dx} = \frac{4\pi Z_B^2 Z e^4 N}{m_e v^2} \left[ \ln \frac{2m_e\theta^2}{I} - \beta^2 - \sum_i \frac{C_i}{Z} - \frac{\delta}{2} \right] . \qquad (2.4)$$

$Z_B$ is the charge number, v the velocity of the beam particle, $\beta = v/C$; Z and N are the charge number and the number density of the field particles. $C_i$ and $\delta$ are the correction terms due to shell effects and polarization. The basic parameter in Eq. (2.4) is the average ionization potential I. Different approaches of calculating the ion stopping differ in the way I is calculated. At KfK, the code GORGON[25] is used. This code is based on the work of Nardi and Zinamon.[16] A semi-classical procedure based on Bohr's model is used to calculate I. However, the calculation is time consuming and not suitable for incorporation in a hydrodynamics code. The alternate procedure is to obtain values of I from appropriate calculations and use an analytical fit to these I values in the dE/dx calculation. We use the analytical fit of Mehlhorn et al.[20] in the data of McGuire et al.[21] Similarly the calculation of stopping due to free electrons in GORGON using the dielectric theory involves time consuming numerical integration.[25] We again use the analytical expression of Mehlhorn.[19] Figure 2.3 shows the result of this latter approach (marked EDEPOS) to the GORGON results. It is seen that the agreement between the two approaches is reasonably good except at low energies. At these low energies, however, uncertainty even in the cold data is large.[13]

## 2.3 Comparison With Published Results

In this section the results of our calculations are compared with a recent publication by Rogerson et al. (NRL).[2] The problem analyzed is a 16

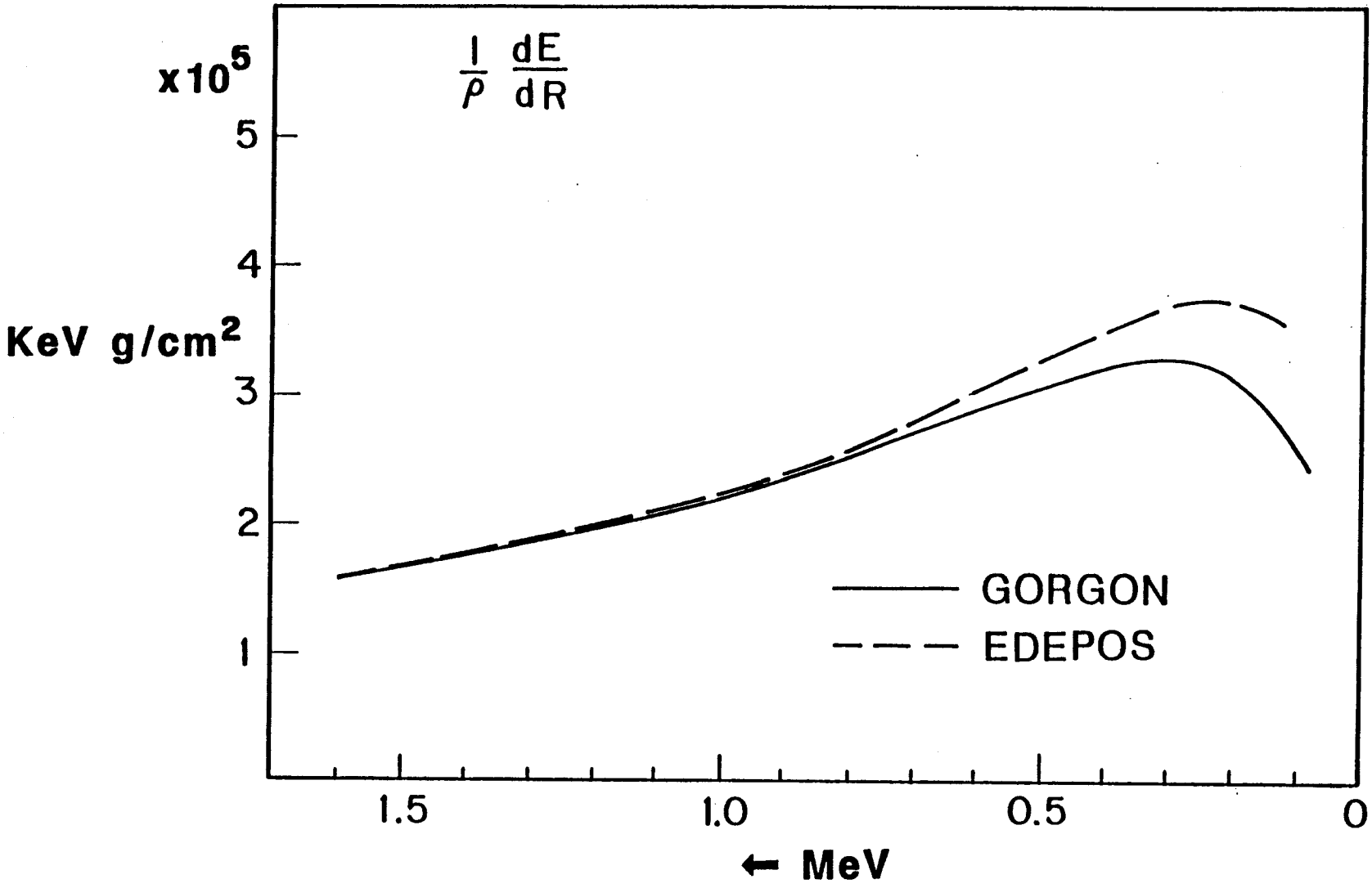


Fig. 2.3. Comparison of proton stopping in aluminum at 100 eV using different approaches.

TW, 1 MeV proton beam incident on a 15 μm thick aluminum slab for 10 ns. Their method of solution is somewhat different than our approach. They use a sliding zone Eulerian hydrodynamics code in contrast to our Lagrangian approach. They also use a collisional radiative equilibrium treatment of the ionization balance.[27] However, in their calculation an average charge value is used. They use a modified ideal gas equation of state, whereas in our codes a more realistic equation of state is used. The energy coupling is also somewhat different between the two approaches. Figure 2.4 shows the energy deposited by 1 MeV photons in each of the 20 equal mass zones of a 15 μm Al target. An understanding of this figure is aided by Figs. 2.5 and 2.6 showing the temperature and density profile at different time steps and by Fig. 2.7 depicting the range shortening and enhancement phenomena as target temperature rises. At the start of the pulse the range of the 1 MeV protons is about the thickness of the target. As the temperature rises, the range shortens to its maximum extent at about 6 ns and starts lengthening again (see also Fig. 2.7). At the start, due to the Bragg peak, the rear part of the target is heated more strongly than the front surface. After about 1 ns of heating with the 16 TW beam, the temperature rises to about 30 eV and range shortening is evident. The temperature continues up to 6 ns. At this time the temperature of the target increases to 200 eV and the Bragg peak has almost disappeared. At 9.5 ns, towards the end of the pulse, the range has increased again to about its original value but due to the higher temperature, the Bragg peak is not as pronounced as at the start. This behavior can also be seen in Fig. 2.7. Figure 2.8 shows the front and rear surface temperatures of the target as calculated with MEDUSA-KA without radiation transport. (Results of PHD-IV without using the radiation transport option are essentially the same.) The

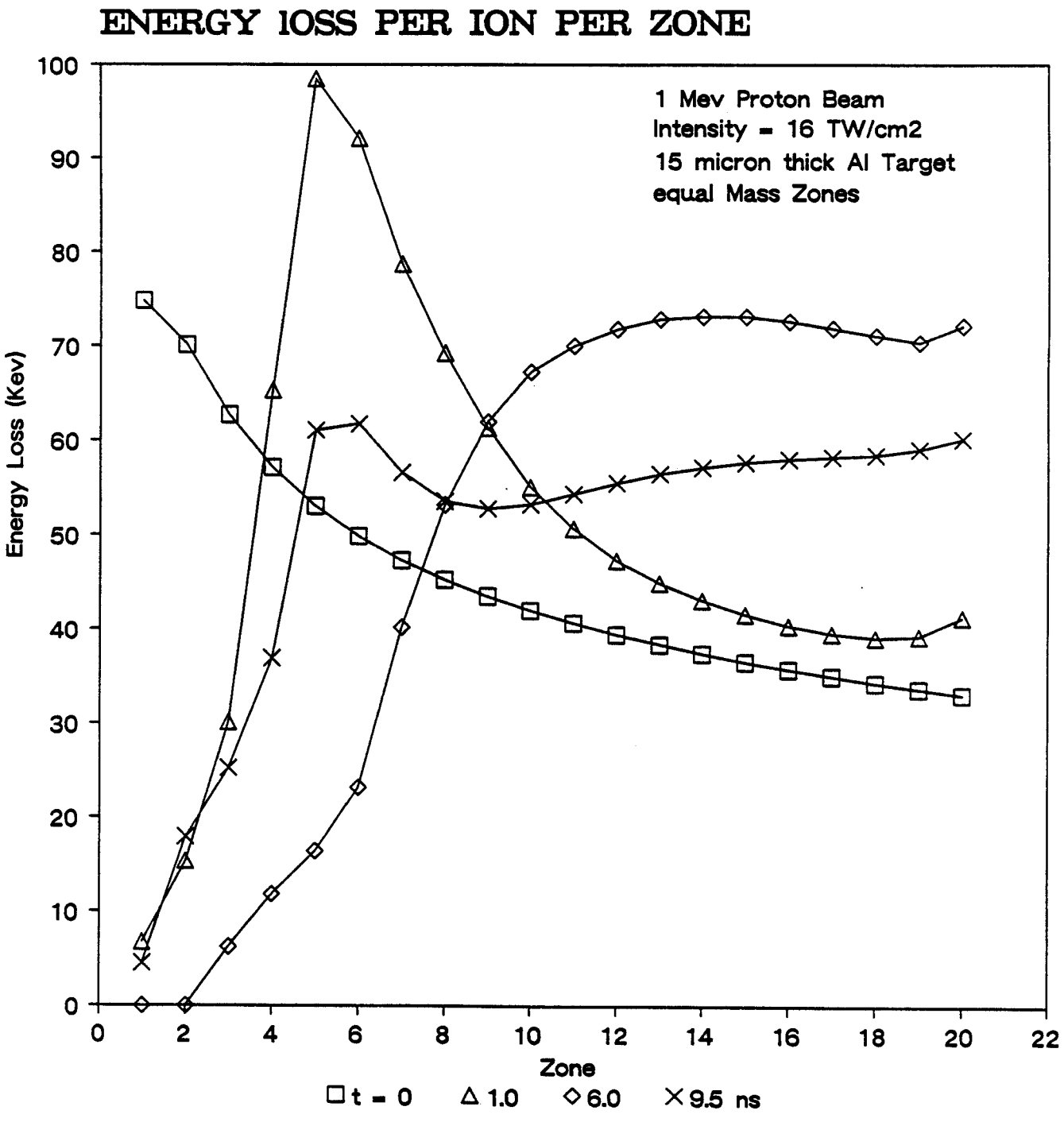


Fig. 2.4. Energy loss per ion per zone in an aluminum target.

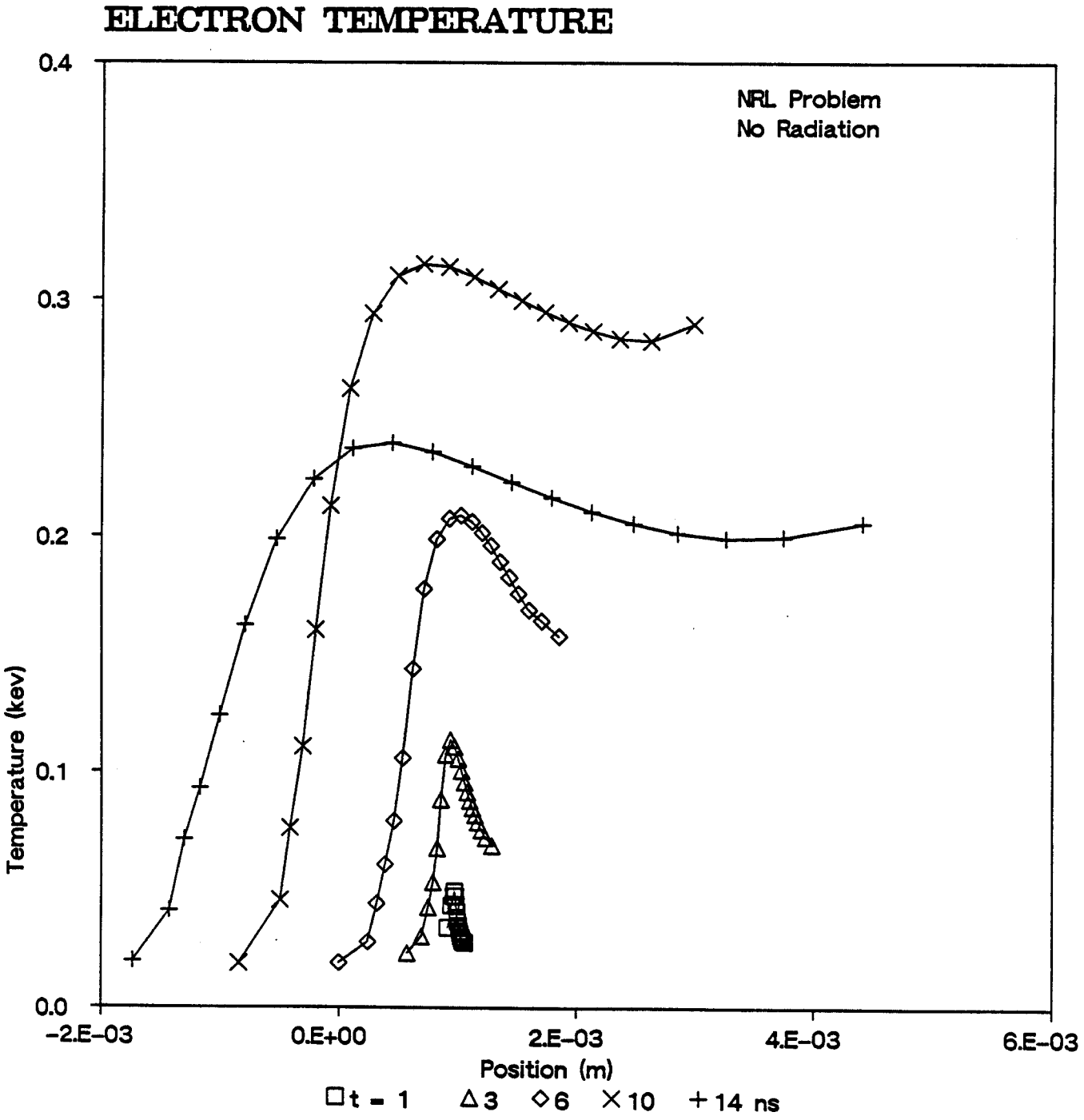


Fig. 2.5. Electron temperature profiles in an aluminum target at various times.

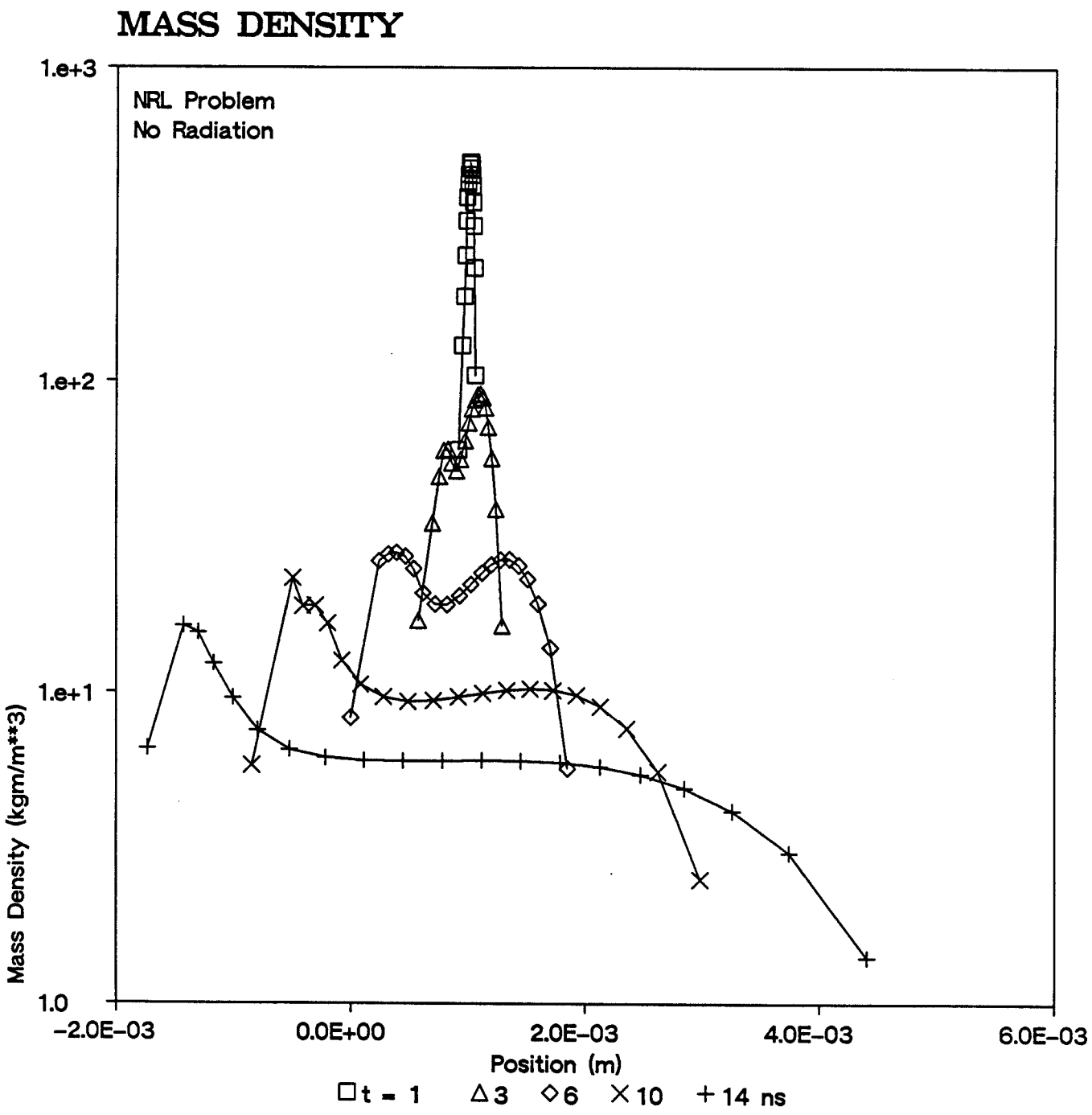


Fig. 2.6. Mass density profiles in an aluminum target at various times.

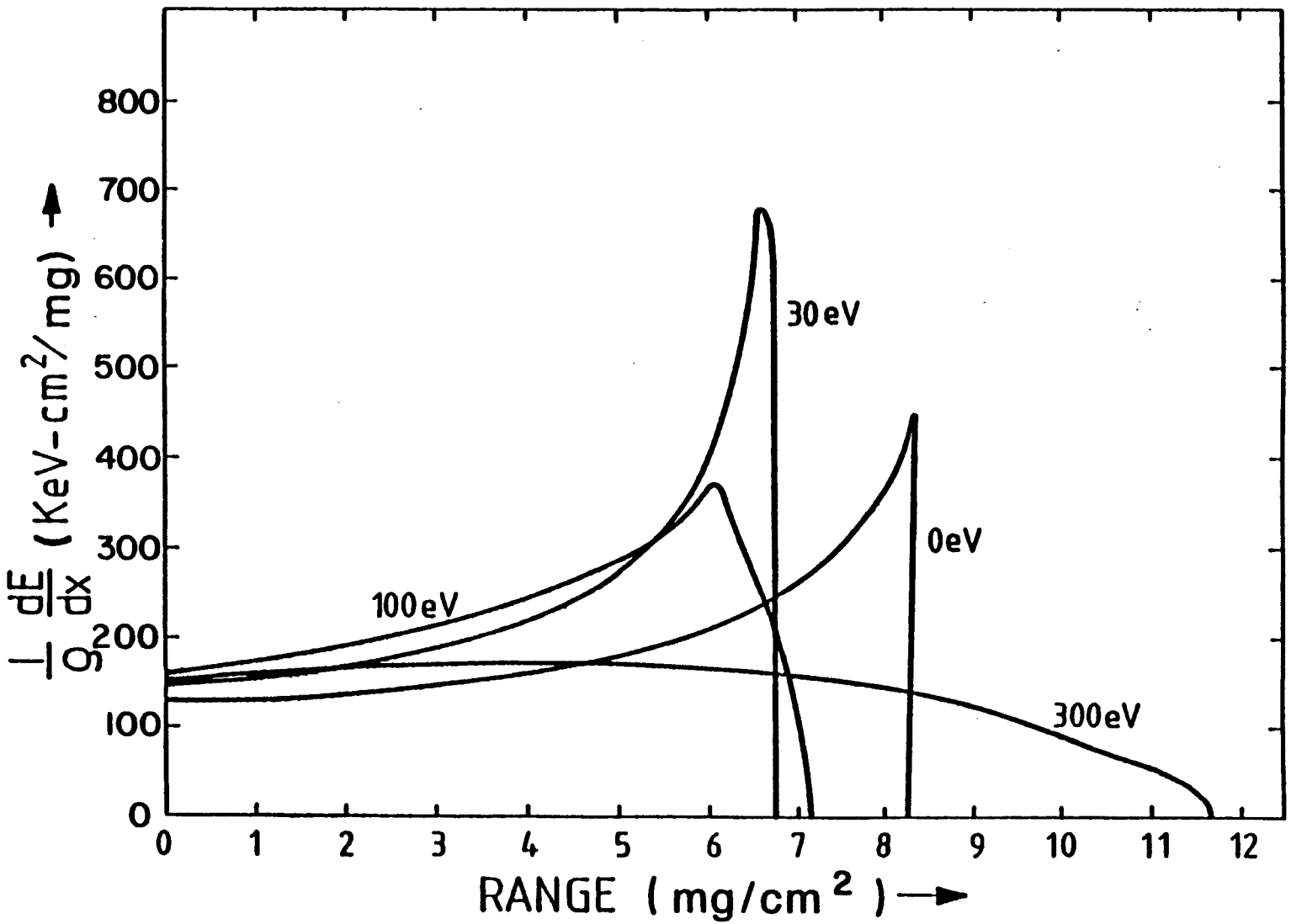


Energy loss of 1.6 MeV protons in solid density aluminum

Fig. 2.7. Energy loss of 1.6 MeV protons versus range in solid aluminum at various temperatures.

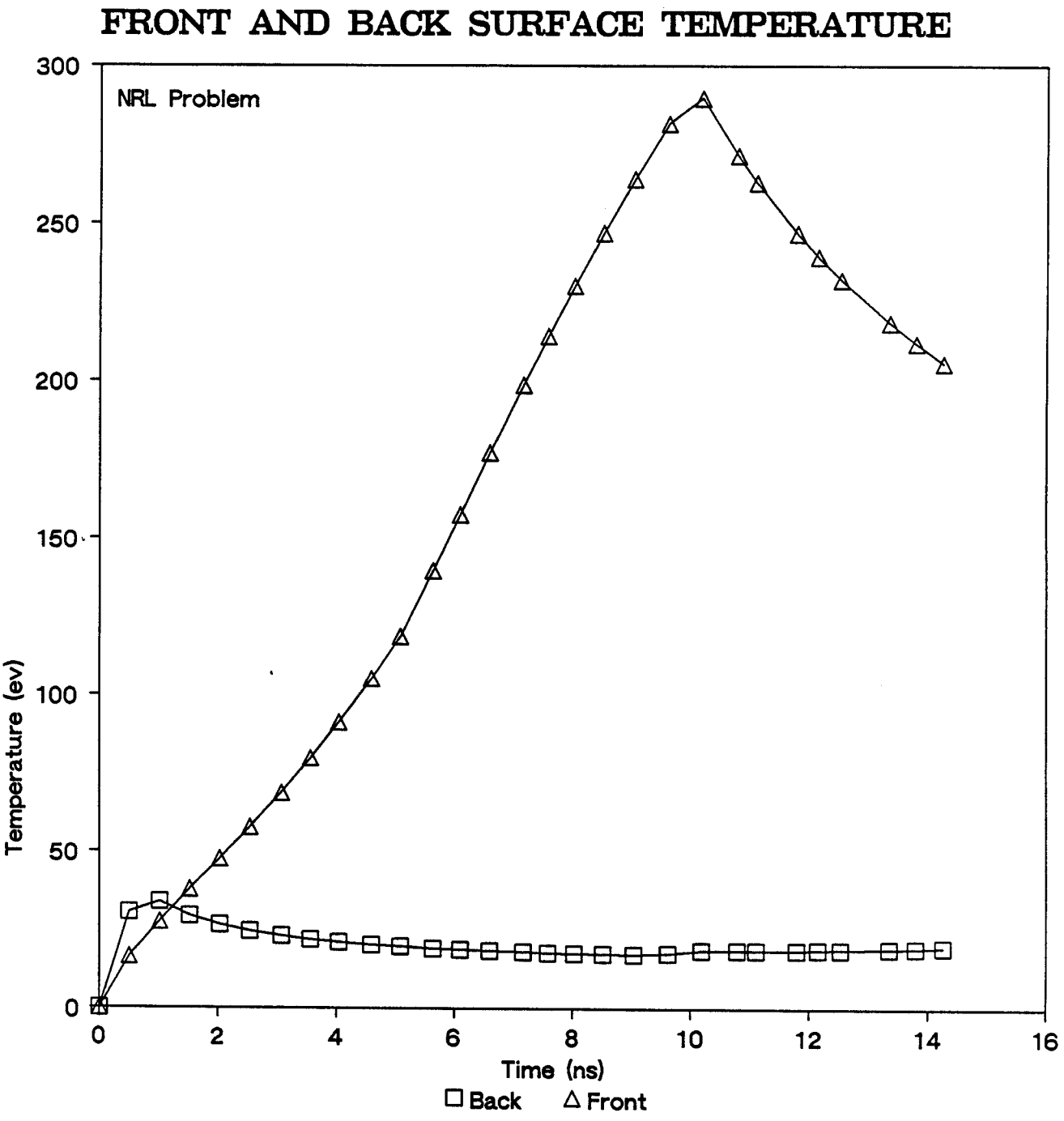


Fig. 2.8. Electron temperatures at the front and rear surfaces of an aluminum target as functions of time where radiative heat transfer has not been included.

temperatures reported by NRL are up to 50% higher than those observed in our calculations. This may be attributed to their use of a simple equation of state and different energy deposition profiles. Rogerson et al.[2] also predicts a slower cooling after the pulse has been shut down. The rise in rear surface temperature (for the no radiation transport case) cannot be seen in our calculation.

In Fig. 2.9 the temperature of the front surface is compared with those of the NRL publication with and without inclusion of radiation transport. In both cases, the temperatures in our calculations are lower than the NRL calculations, but both calculations show similar behavior of the temperature. Considering the difference in calculational methods the agreement is considered reasonably good.

Finally, in Fig. 2.10 front surface temperatures at different times are given. The multigroup radiation transport cannot give details of line radiation but the overall shape of emitted spectra compares well with those of Rogerson et al.

## 2.4 Pre-Experiment Calculations for Ion Stopping Measurements on KALIF

The 16 TW beam power used in our benchmark calculations is more than an order of magnitude higher than the light ion beam power that can be reached with the present day KALIF machine. The idealized square pulse is also of an academic interest. The shape of the ion beam pulse would look somewhat like Fig. 2.11. Both voltage and current change with time. The ion beam does not always hit the target normally as assumed in the previous section. But due to the geometry of the anode and ballistic focusing, the angle of incidence varies according to the diode characteristics. The codes MEDUSA-KA and PHD-IV were modified to accommodate these effects.

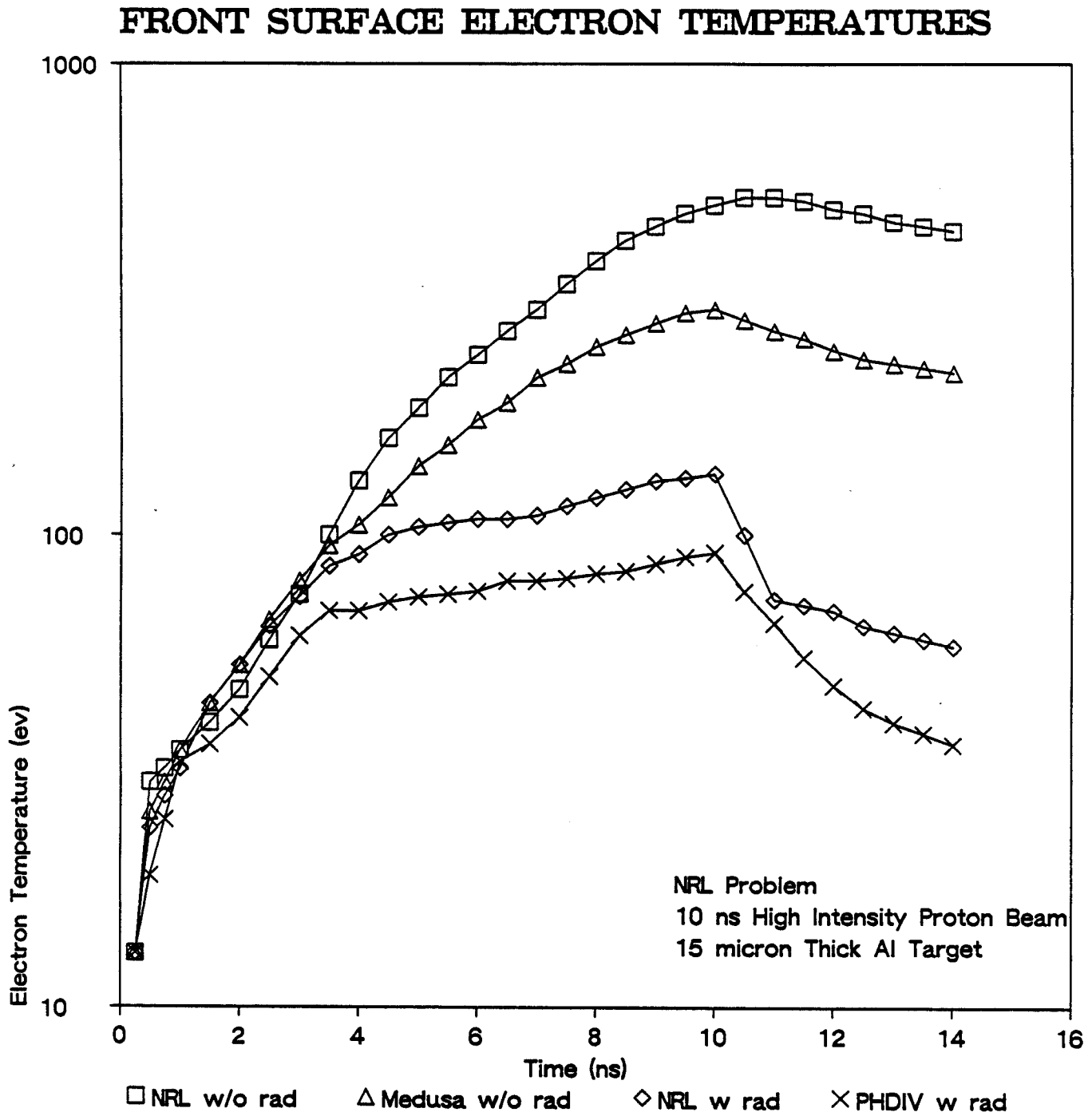


Fig. 2.9. Electron temperatures at the front surface of an aluminum target as functions of time for cases where radiative heat transfer has and has not been included.

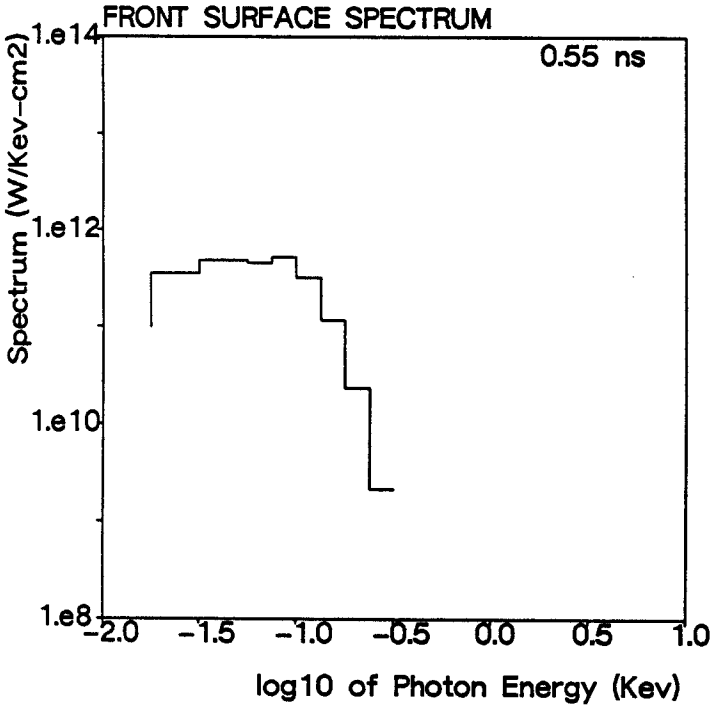


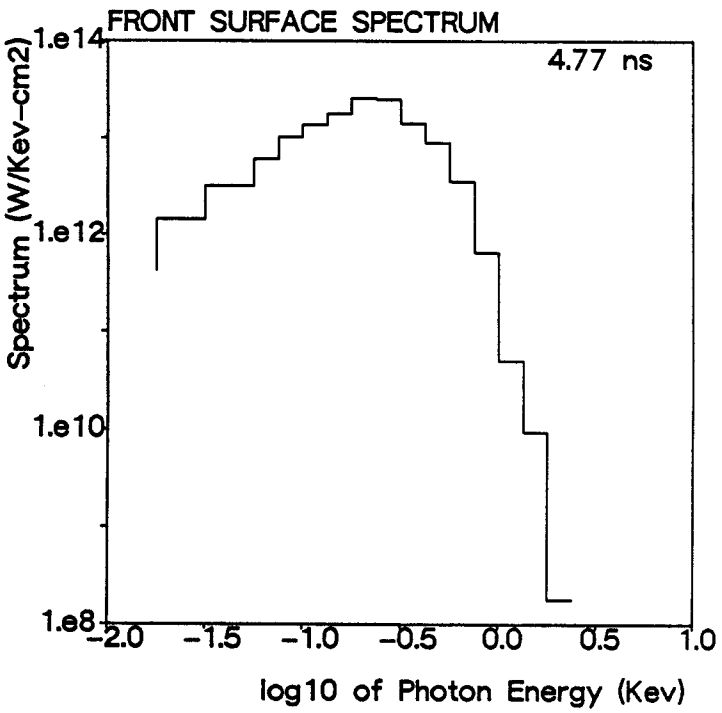


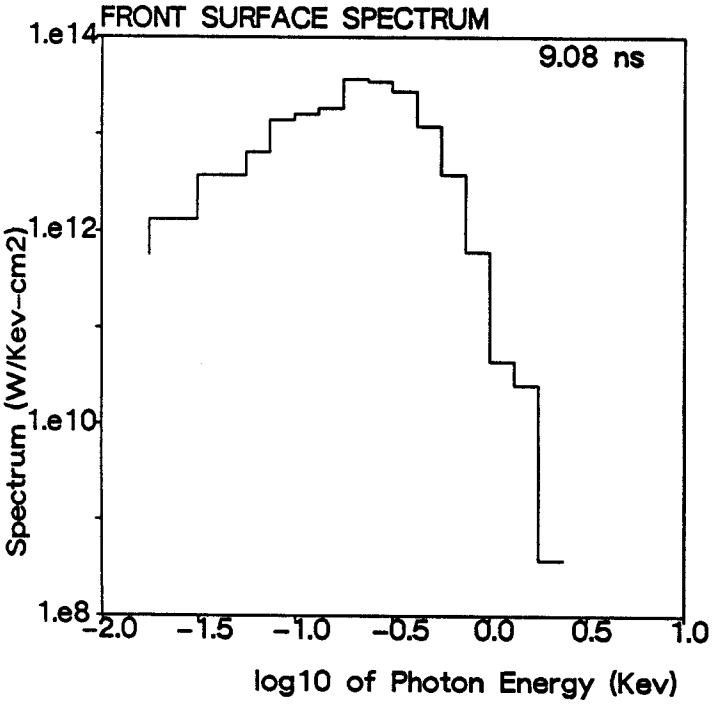


Fig. 2.10. Spectra of radiation leaving the front surface of an aluminum target at three different times.

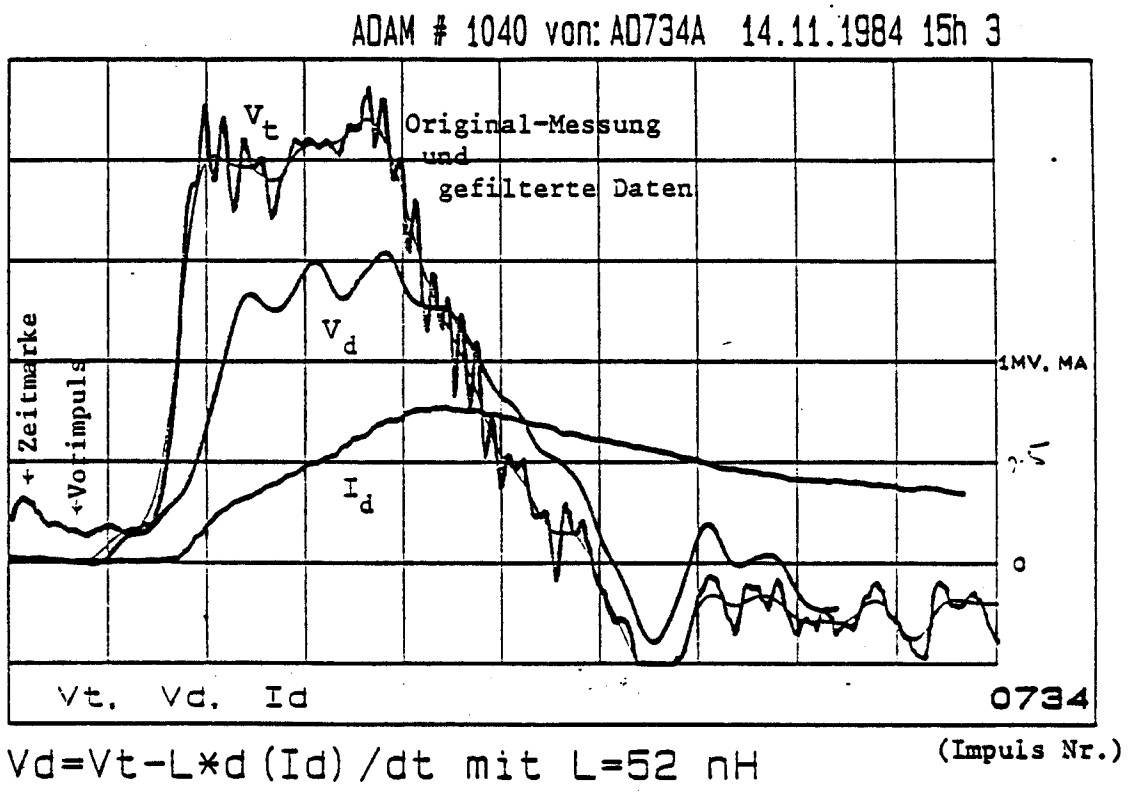


Fig. 2.11. Voltage and current profiles of a pinch reflex diode on KALIF.

Calculations were done assuming the beam profile as in Fig. 2.11 and an average incident angle of 74°. It was assumed that these profiles are transferred to the ion beam without appreciable distortion. It is recognized that the ion current will be much less than the total diode current. The total power assumed on the target is 0.4 $TW/cm^2$ in our calculations as compared to 0.3 $TW/cm^2$ measured earlier this year.[1] For the present calculation a 7.5 μm (2 $mg/cm^2$) thick aluminum slab target is chosen. The thickness is about a quarter of the range of 1.5 MeV protons in cold material. As will be shown later this target allows the measurement of proton stopping in aluminum from about 3 eV to 25 eV.

Figure 2.12 shows the evolution of temperature and density of the target midplane with time. Also shown is the incident beam power. The basis of this figure is a MEDUSA-KA calculation without radiation transfer. At these temperatures this omission makes little difference except at the end of the pulse, at times where the ion stopping measurement is not possible anyway. If the ion beam would start at 1.5 MeV instantaneously the target would be heated uniformly and the dE/dx measurement could start right from the beginning. However, at the initial stages, beam voltage is so low that the Bragg peak in the ion stopping nonuniformly heats the target. At about 10 ns the target temperature profile becomes fairly uniform and as seen in Fig. 2.13 remains so throughout the course of the experiment. (Please note that the time scale in the hydro calculation is different than in Fig. 2.11. Hydro calculations start at the point when power coming out of the diode is different from zero.) The density profile (Fig. 2.14) is parabolic because outer zones expand more quickly than the center of the target. Figure 2.15 shows the incoming beam energy and the energy with which particles leave the rear surface of the

Fig. 2.12. Electron temperature and density at the midplane of an aluminum target heated by protons from KALIF.

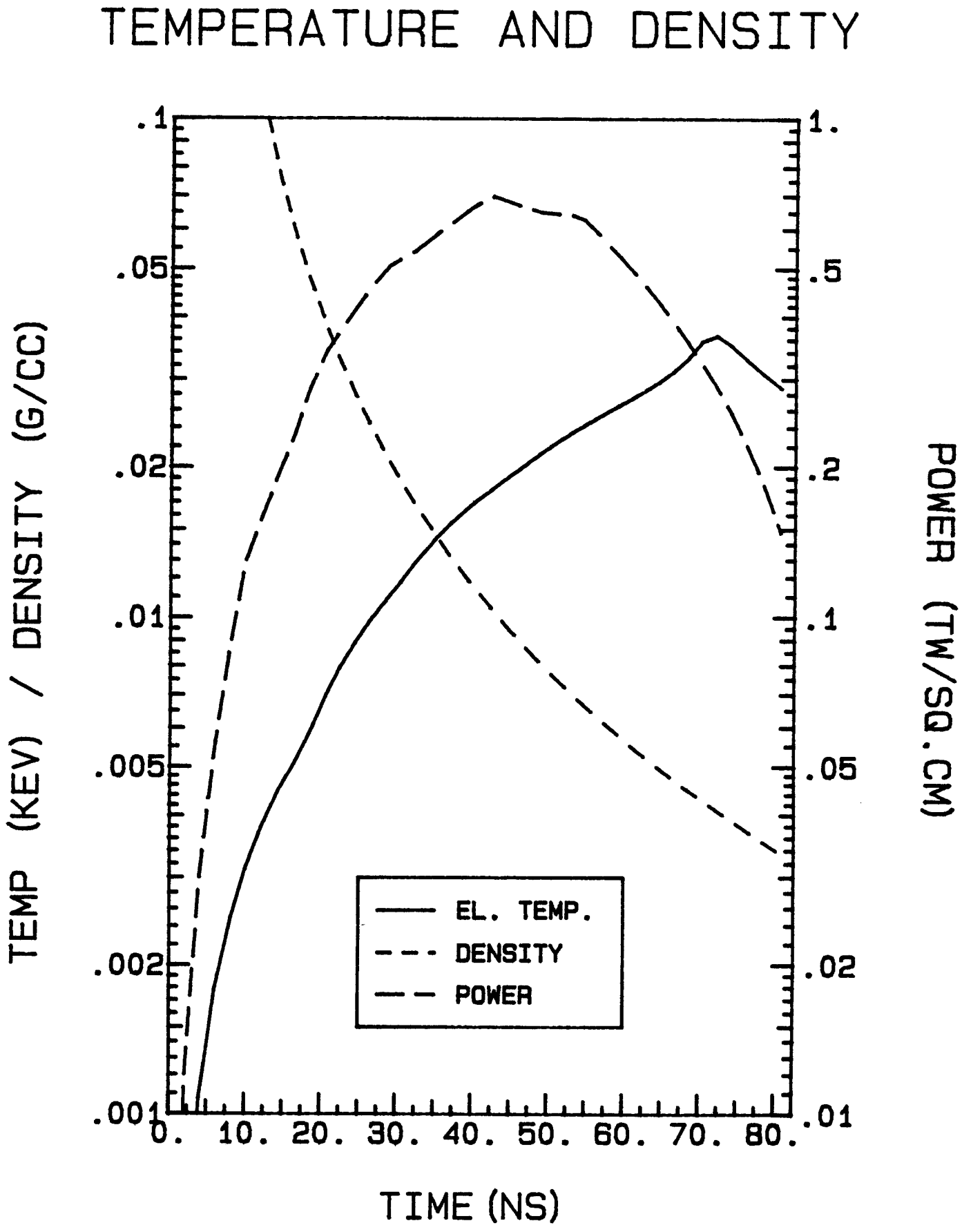

Fig. 2.13. Electron temperature profiles at various times of an aluminum target heated by protons from KALIF.

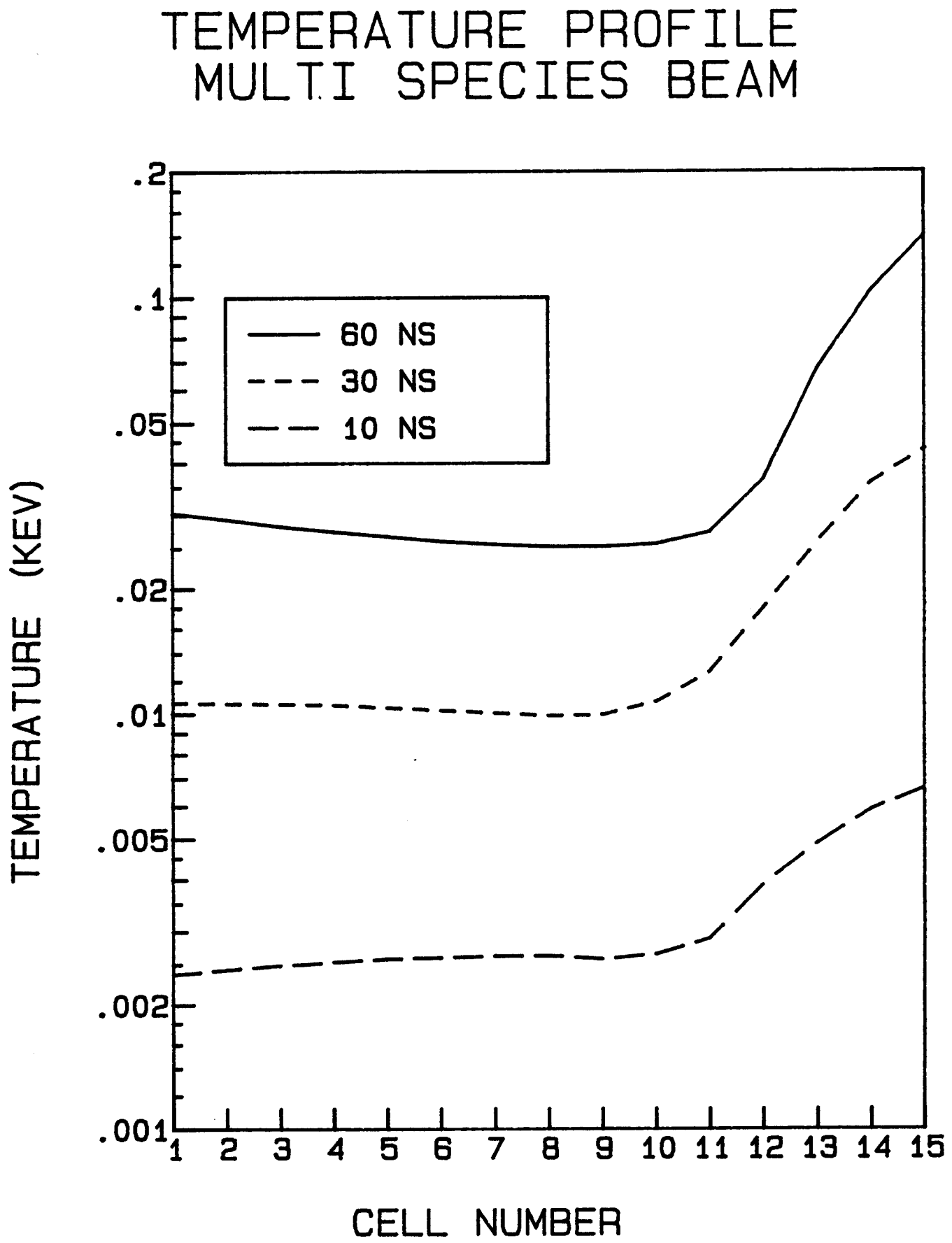

Fig. 2.14. Mass density profiles at various times of an aluminum target heated by protons from KALIF.

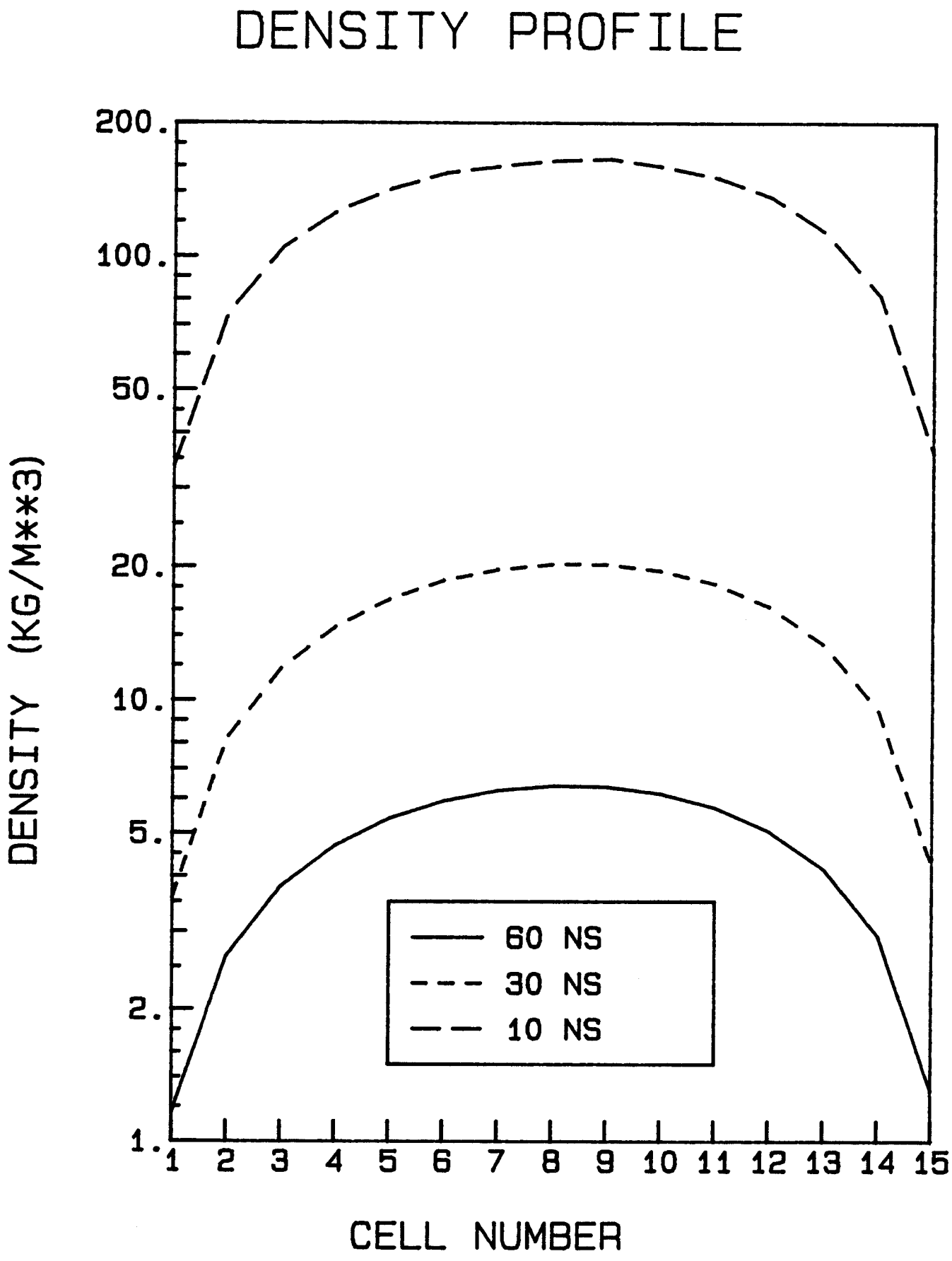

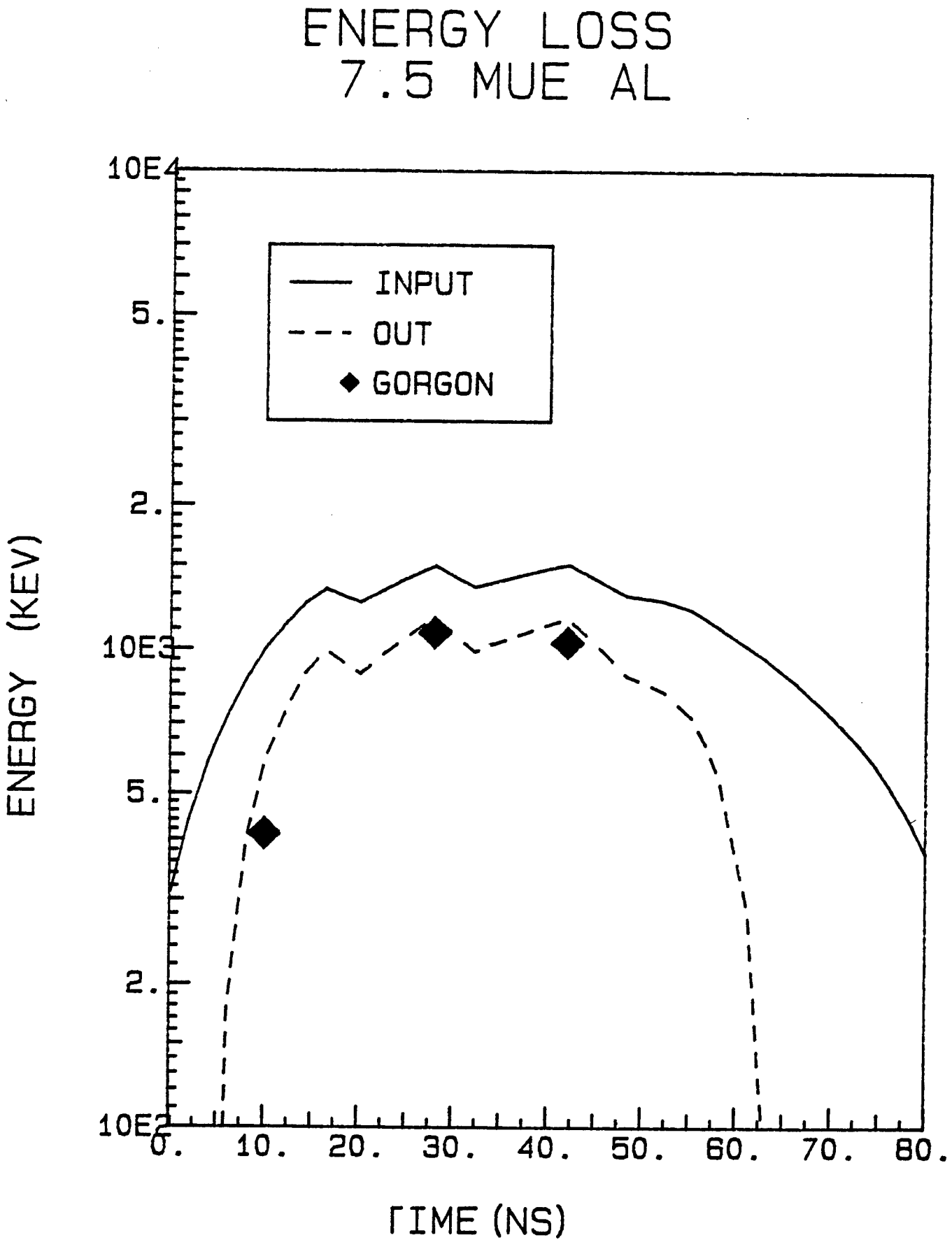


Fig. 2.15. Energy per ion for a proton beam from KALIF as it enters and leaves a 15 μm thick aluminum target.

target. Also shown are the results of calculations with the GORGON code for three different time steps, using the average temperature and density. It is seen that the agreement with the basic dE/dx GORGON code and a more simple method incorporated in the hydro code is very good. Because of the low energy of the beam it does not penetrate out of the target for the first 5 ns. At this time the temperature of the target has reached 3 eV and the input beam energy is 1 MeV. The measurement can be continued until about 55 ns at which time the temperature of the target is 25 eV. Radiation losses are not important at these temperatures. There is also an enhancement of stopping power due to temperature and density changes. For example at 10 ns, out of 1 MeV input energy, only 420 keV is deposited in the target (T = 3 eV and $\rho = \rho_s/20$) whereas at 60 ns the input energy is again 1 MeV. The energy lost in the target is 730 keV, almost double the previous value. At this time the temperature is $\approx$ 30 eV and $\rho = \rho_s/500$. In a one-dimensional slab target the $\rho R$ value of the target remains constant as the target expands. Thus in this experiment stopping enhancement should be clearly observed.

The results presented so far assumed that the particle beam is purely protons, but in fact the beam is always contaminated with other particles. At KALIF, the ion beam was observed to contain only 87% protons, with the remainder being carbon; namely 3% $C^{+}$, 8% $C^{+2}$ and 2% $C^{+3}$. Since dE/dx is proportional to $Z^2$ the range of carbon ions is much shorter than protons. In fact, they are stopped in the first 1/3 of the target, thereby raising the temperature of the front surface dramatically (Fig. 2.16). In the calculation without radiation transport, temperatures higher than 100 eV are predicted. At these temperatures, ignoring the radiation is not a good approximation. Calculations were repeated with radiation transport included using the PHD-IV

Fig. 2.16. Electron temperature profiles at various times of an aluminum target heated by protons and carbon ions from KALIF.

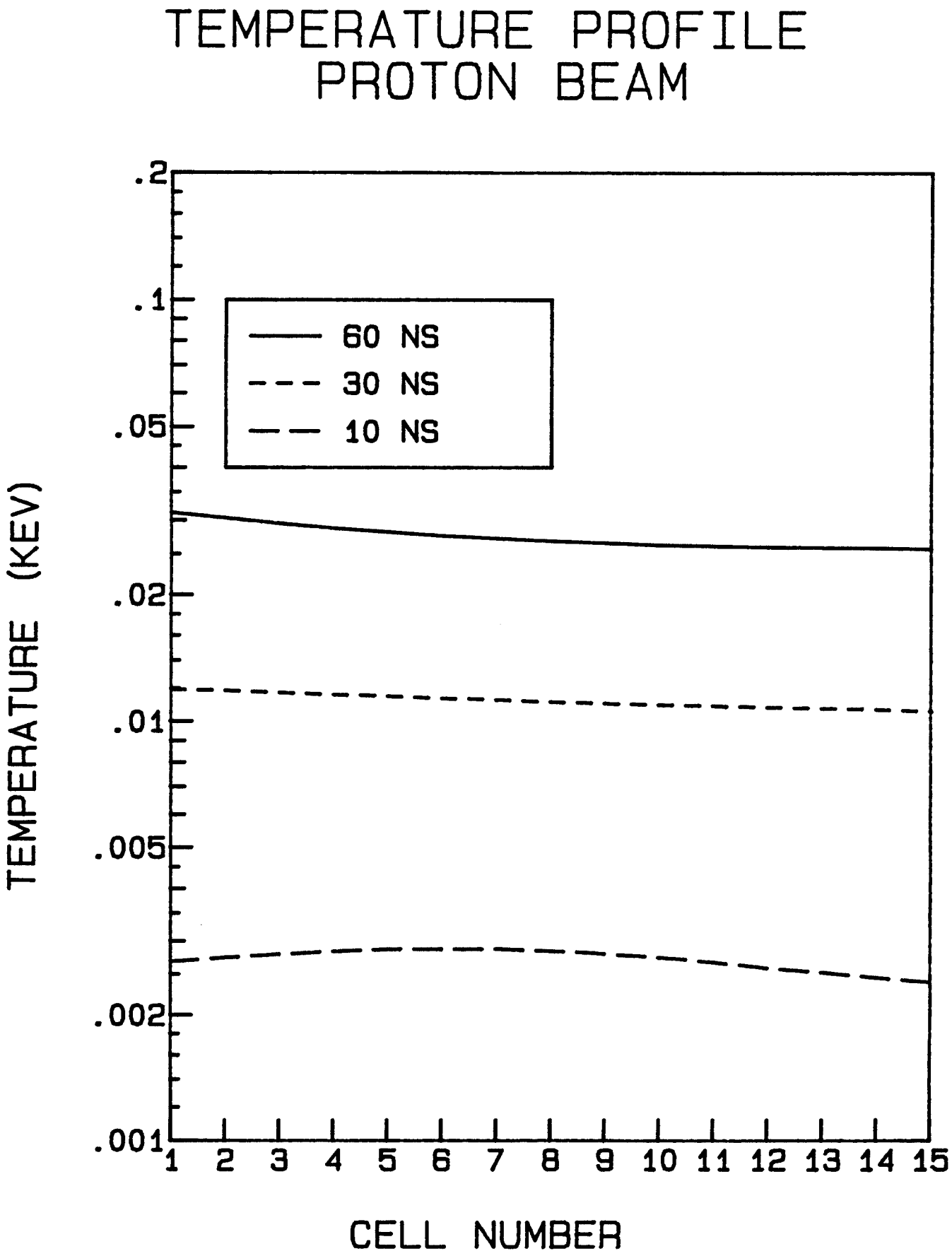

code. The extremely high temperatures, for example at 33 and 60 ns, have been lowered due to radiation cooling. At 60 ns even the temperature profile is almost as flat as in the case of protons only. However at earlier times the flatness of the temperature profile has been destroyed due to the carbon contamination of the beam.

## 2.5 Discussion of Results

Results presented in Section 2.3 show a reasonable agreement between our code predictions and those of Rogerson et al.[2] At the beam power level of 16 TW both phenomena of range shortening and range lengthening can be observed. At this power level, radiation transport is very important. Our multigroup treatment of radiation transport compares with their continuum spectrum. However, we cannot obtain any detailed information about the line radiation. The main difference between our predictions and those of Rogerson et al. is in the electron temperature. We believe that this is due to different equation of state.

At the Karlsruhe Light Ion Facility KALIF, dE/dx measurements can be made as a function of temperature in a temperature range of 3 eV to 25 eV for protons of energies 1 MeV and higher. The densities associated with these measurements are 1/30 to 1/500 of the solid state density. The present beam characteristics of KALIF would allow the dE/dx measurement at uniform target temperatures. However, to achieve this, carbon ions must be removed from the beam. This can be accomplished by putting a thin foil in front of the aluminum target. This foil can also be used as a Rutherford scattering diagnostic to measure the energy of the particle beam entering the target foil (Fig. 2.1). Radiation effects are not important at the present power density of

about 1/2 $TW/cm^2$. The results of the energy stopping formalism included in the hydro codes, MEDUSA-KA and PHD-IV match very well the results of GORGON.

Another experiment of this type was performed at the Proto-I accelerator of Sandia National Laboratory and has been published recently.[15] The basic trend of our calculations matches well with results published by Olsen et al.[15] However, the temperature and density profiles are not given in Ref. 15. The proton beam at KALIF has a purity of about 90% whereas at Proto-I about 58% of the beam is reported to be nonprotonic.

## 2.6 Summary and Conclusions

We have shown that computer codes MEDUSA-KA and PHD-IV with their recent modifications, are suitable to analyze energy deposition experiments. The results of calculations with these codes agree well with the results of Rogerson et al. for a 1 MeV, 16 TW proton beam incident on 15 μm aluminum. KALIF with its present characteristics is suitable to measure dE/dx in aluminum in the temperature range of 3 eV to 25 eV. It is planned to improve the power density at KALIF (a) by inductive pulse compression and plasma erosion switches, and (b) by improving the diode performance. Pulse compression associated with voltage doubling would extend the dE/dx measurements towards lower temperature, down to about 1/2 eV. An increase in power densities would extend the range towards higher temperature. At these temperatures, however, radiation cooling of the target becomes important. Thus an 8 fold increase in power density would extend the temperature range of the measurement only by a factor of 3 (i.e., to about 70 eV).

References for Chapter 2


1. H. Bluhm, K. Boehnel, L. Buth, P. Hoppé, H.V. Karow, A. Klumpp, D. Rusch, T. Scherer, U. Schuelken and J. Singer, IEEE Int'l. Conf. on Plasma Science, Pittsburgh, June 1985.

2. J.E. Rogerson, R.W. Clark and J. Davis, Phys. Rev. A31, 3323 (1985).

3. J.P. Christiansen, D.E.T.F. Ashby and K.V. Roberts; Comp. Phys. Comm. 7, 271 (1974).

4. N.A. Tahir and K.A. Long; KfK 3454, Karlsruhe (1983).

5. B. Goel and W. Höbel, Plasma Physics and Controlled Nuclear Fusion Research, London, 12-19 September 1984, Nuclear Fusion Supplement 1985, Vol. 3, p. 345.

6. G.A. Moses, Nucl. Sci. Engr. 64, 49 (1977).

7. G.R. Magelssen and G.A. Moses, Nucl. Fus. 19, 301 (1979).

8. L. Spitzer, Jr., Physics of Fully Ionized Gases, 2nd Edition, John Wiley & Sons, New York, p. 125.

9. W.F. Huebner, A.L. Merts, N.H. Magee, Jr., and M.F. Argo, LA-6760-M, Los Alamos (1977).

10. B.I. Bennet, J.D. Johnson, G.I. Kerley and G.T. Rood, LA-7130, Los Alamos (1978).

11. A.R. Bell, RL-80-91 Rutherford (1981).

12. D.A. Kirzhnits, Sov. Phys. JETP 8, 1081 (1959).

13. J.F. Ziegler, Stopping Cross Section for Energetic Ions in All Elements, Vol. 5, Pergamon Press, New York, 1980.

14. F.C. Young, D. Mosher, S.J. Stephanakis, S.A. Goldstein and T.A. Mehlhorn, Phys. Rev. Lett. 49, 549 (1982).

15. J.N. Olsen, T.A. Mehlhorn, J. Maenchen and D.J. Johnson, J. Appl. Phys., (1985).

16. E. Nardi and Z. Zinamon, Phys. Rev. Lett. 49, 1251 (1982).

17. E. Nardi, E. Pelleg and Z. Zinamon, Phys. Fluids 21, 574 (1978); and Appl. Phys. Lett. 39, 46 (1981).

18. C. Deutsch, G. Maynard and H. Minoo, in GSI-82-8, p. 543, Gesellschaft für Schwerionenforschung, Darmstadt (1982).

19. T.A. Mehlhorn, J. Appl. Phys. 52, 6522 (1981).

20. T.A. Mehlhorn, J.M. Peek, E.J. McGuire, J.N. Olson, F.C. Young, J. de Physique, Colloque 44, C8-39 (1983).

21. E.J. McGuire, J.M. Peek and L.C. Pitchford, Phys. Rev. A26, 1318 (1982).

22. T.D. Beynon, Phil. Trans. Roy. Soc. London A300, 613 (1981).

23. W. Geiger, H. Hornberg and K.H. Schramm, Springer, Tracts of Modern Physics 46, 1 (1968).

24. H.A. Bethe, Ann. d. Physik (Leipzig) 5, 325 (1930).

25. K.A. Long, N. Moritz and N.A. Tahir, KfK-3608, Karlsruhe (1983).

26. D. Duston, R.W. Clark, J. Davis, J.P. Apruzese, Phys. Rev. A21, 1441 (1983).

## 3. IMPROVEMENTS TO THE Z-PINCH COMPUTER CODE

The Z-PINCH computer code has now been in use for over a year and a half. During the past year, several modifications have been made to the code that make it both more convenient to use and more physically consistent. These modifications are described and a sample problem demonstrating some of the modifications is displayed.

Several of the modifications are mainly cosmetic. These include the specification of driving circuit parameters (resistance, inductance, capacitance and initial voltage, and an additional driving voltage) and the ion beam current density. Previously, the driving circuit parameters were obtained by reading in a file that contained the values of $R_o$, $L_o$, etc. vs. time. These values are now given by specifying the nine parameters in a function of the form

$$R_o(t) = R_o + R_1 \exp\left[-\left(\frac{t - t_1}{\tau_1}\right)^{n_1}\right] + R_2 \exp\left[-\left(\frac{t - t_2}{\tau_2}\right)^{n_2}\right] .$$

The inductance $L_o$ and applied voltage are given by functions of identical form, both with nine analogous parameters of their own. This functional form provides the user with a great deal of flexibility; by proper choice of the parameters, the user may specify constant values ($R_1 = R_2 = 0$), nearly linear ramps ($R_2 = 0$, $R_1 \neq 0$, $\tau_1 >> t$) and nearly instantaneous changes ($\tau_1$, $\tau_2$ small; $n_1$, $n_2$ large).

The specification of initial conditions in the driving circuit has also been made more convenient. In addition to the three sets of nine parameters that define $R_o(t)$, $L_o(t)$, and $V_{applied}(t)$, the user specifies the value of a capacitance and charge on the capacitor, as well as an initial value for the

discharge current (I(0) = 0 in most applications). This setup provides the user with a great deal of flexibility in defining the driving circuit. A new output edit has been added that gives a detailed accounting of the voltages in the circuit which allows the user to follow the flow of energy from the driving circuit to the discharge.

The specification of the ion beam current has likewise been made more convenient. Previously, $J_{beam}(r)$ was given by a combination of piecewise linear functions. This has been modified so that $J_{beam}(r)$ is now given by a nine parameter function similar to that used for defining $R_o(t)$, $L_o(t)$, and $V_{applied}(t)$, except that the independent variable is radius rather than time. Thus, the user specifies the radial profile of the beam current density by inputting the values of the nine parameters in the function

$$J_{beam}(r) = I_{beam}\left[\alpha + \beta \exp\left[-\left(\frac{r - r_1}{R_1}\right)^{n_1}\right] + \gamma \exp\left[-\left(\frac{r - r_2}{R_2}\right)^{n_2}\right]\right]$$

where $I_{beam}$ is the total electrical current of the beam.

When an ion beam is included in the simulation, the module BEAMCD evaluates this function on the Lagrangian mesh and integrates it in order to normalize the total beam current to $I_{beam}$. This insures that the total beam current will not change as a result of motion of the grid, which was a problem before this revision was made.

The only change that has been made to the physics in the code has been to improve the modeling of the discharge as a load in the circuit. The problem is that the discharge voltage drop $V_{dis}$ depends on the discharge current, which in turn depends on $V_{dis}$. The discharge current and $V_{dis}$ must be obtained in some self-consistent manner under the constraint that the voltages

around the circuit sum to zero (Kirchhoff's law). Part of the solution to this problem was to express $V_{dis}$ in a form where an explicitly inductive term could be identified. A scheme was then developed in which the calculation of the discharge inductance and discharge current were calculated iteratively. This scheme satisfies Kirchhoff's law much better than the code had before this revision was made. The practical implication of this revision is that since the discharge has a fairly high inductance ($\simeq$ 1 μH/m) it takes a great deal of energy to drive a rapidly changing discharge current. The accompanying Fig. 3.1 illustrates this by comparing the discharge current in a circuit where the discharge load is not included to one in which the load is included. In both circuits, the current is driven by a 2 μF capacitor charged to 0.5 MV (0.2 MJ stored energy) with $R_o$ = 10 Ω and $L_o$ = 0.5 μH. The difference in current traces is due mainly to the inductive load of the discharge ($\simeq$ 2.5 μH). The change in discharge inductance as the magnetic field diffuses into the discharge also loads down the current, but this effect is not so great.

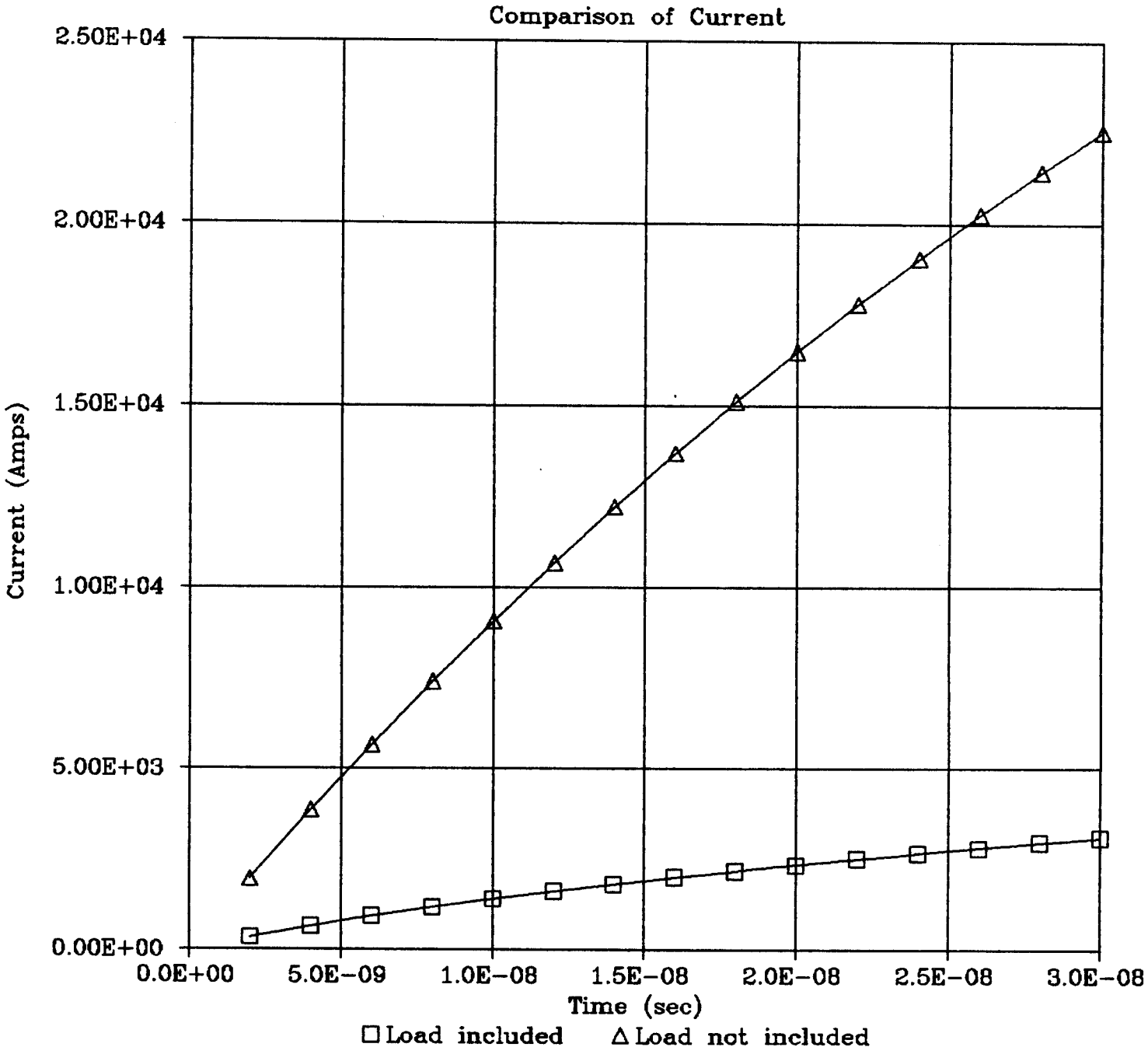


Fig. 3.1. Comparison of the discharge current with and without the load inductance.

## 4. LIGHT ION FUSION REACTOR DESIGN WORK

The feasibility of Light Ion Fusion as a concept for electrical power production is an important part of FPA's work for KfK. The LIBRA reactor concept has been under constant evolution as work continues on various reactor relevant issues. The evolution of the reactor's general parameters is shown in Table 4.1. The major changes in the parameters this year are to a beam ion species of 20 MeV $D^+$ and the change to a smaller cavity, with a corresponding shortening of the plasma channels.

Work has continued on several issues dealing with the design of light ion beam driven fusion reactors. The interface between the driver and the reaction chamber cavity has been addressed by matching the geometrical requirements of beam propagation and pulsed power machinery with those of the cavity. The effects of geometry on the cavity appear substantially through the neutron transport, which has been calculated for the cavity for various geometries. A literature search has been completed that studies the topic of shock flow around cylinders, in order to better understand gas dynamics in the region of the INPORT tubes. The flow of lithium-lead coolant in the INPORT tubes has been reevaluated due to the changes in the cavity geometry. The thermal and mechanical loading on the INPORT tubes due to the target explosion have been calculated for the new geometry. The mechanical behavior of the INPORT tubes under the influence of the target generated pressure has been considered, including the effects of the coolant flow. Finally, the operating conditions of the plasma channels are considered for the new geometry and the latest design of the driver.[1]

Table 4.1. Chronology of LIBRA Parameters, 1982-1985

| Parameter | 1982 | 1983 | 1984 | 1985 |
|---|---|---|---|---|
| Type of reactor | Demo-Elec. | Demo-Elec. | Demo-Elec. | Demo-Elec. |
| DT power, MWth | 500 | 480 | 480 | 480 |
| Net electric power, MWe | 215 | 215 | 215 | 204 |
| Pulsed power type | General | Helia | Helia | Helia |
| Repetition rate, Hz | 1.5 | 1.5 | 1.5 | 1.5 |
| Ion | Li | Li | D | D |
| Ion Energy, MeV | 21 | 30 | 15 | 20 |
| Energy on target, MJ | 4 | 5 | 4 | 4 |
| Number of beam lines | 40 | 40 | 24 | 24 |
| Beam prop. length, m | --- | --- | 11 | 6 |
| Power on target, TW | 320 | 320 | 240 | 240 |
| Target type | Single Shell Cryogenic | Single Shell Cryogenic | Single Shell Cryogenic | Single Shell Cryogenic |
| Target gain | 80 | 80 | 80 | 80 |
| Cavity gas | Ar + 0.002 Li | Ar + 0.002 Li | Ar + 0.002 Li | Ar + 0.002 Li |
| Gas pressure, torr | 10 | 10 | 10 | 10 |
| First wall protection | INPORT units | INPORT units | INPORT units | INPORT units |
| Radius to INPORT, m | 5 | 5 | 5 | 3 |
| Tritium breeding ratio | 1.09 | 1.09 | 1.09 | 1.16 |
| Blanket multiplication | 1.4 | 1.4 | 1.4 | 1.31 |
| Radius to back of shield, m | 8 | 8 | 8 | 4 |

## 4.1 Driver/Cavity Interface

### 4.1.1 Layout

An overall layout of the light ion driver and the reaction chamber has been done for the latest driver design.[1] The purpose of this is to determine the geometrical interaction between the placement of the pulse power modules, the placement of the diodes, the lengths of the plasma channels, and the size of the reaction chamber. An additional effort has been made to investigate pulse shaping by geometrical placement and timing of the diodes.

The layout is shown, in an overhead view, in Fig. 4.1. There are 28 meters from the back of the inductive HELIA section of the pulsed power to the target, which means that the facility as a whole must be at least 60 meters in radius. The Sandia Light Ion Fusion Target Development Facility (TDF)[2] has, for comparison, about 23 meters from the target to the back of the inductive voltage adder. There are about 11 meters of transmission line from the HELIA modules to the diodes. The diodes are about 7 meters from the target and the plasma channels must be about 6 meters long. Two or three meters of the plasma channels may be confined in a tube that can improve the stability of the channels and increases the credibility of 6 meter long channels. A side view of the device is shown in Fig 4.2. The driver modules are seen to be coplanar, whereas in previous work,[3] shown in Fig. 4.3, there were sets of modules entering the reaction chamber from above and below the central plane. There are important maintenance and construction advantages to the new coplanar geometry.

In order to ignite and burn high gain targets, it is necessary to shape the pulse of ion power on the target. Specifically, a low power prepulse is required. Since the electromagnetic energy in the pulsed power machinery is

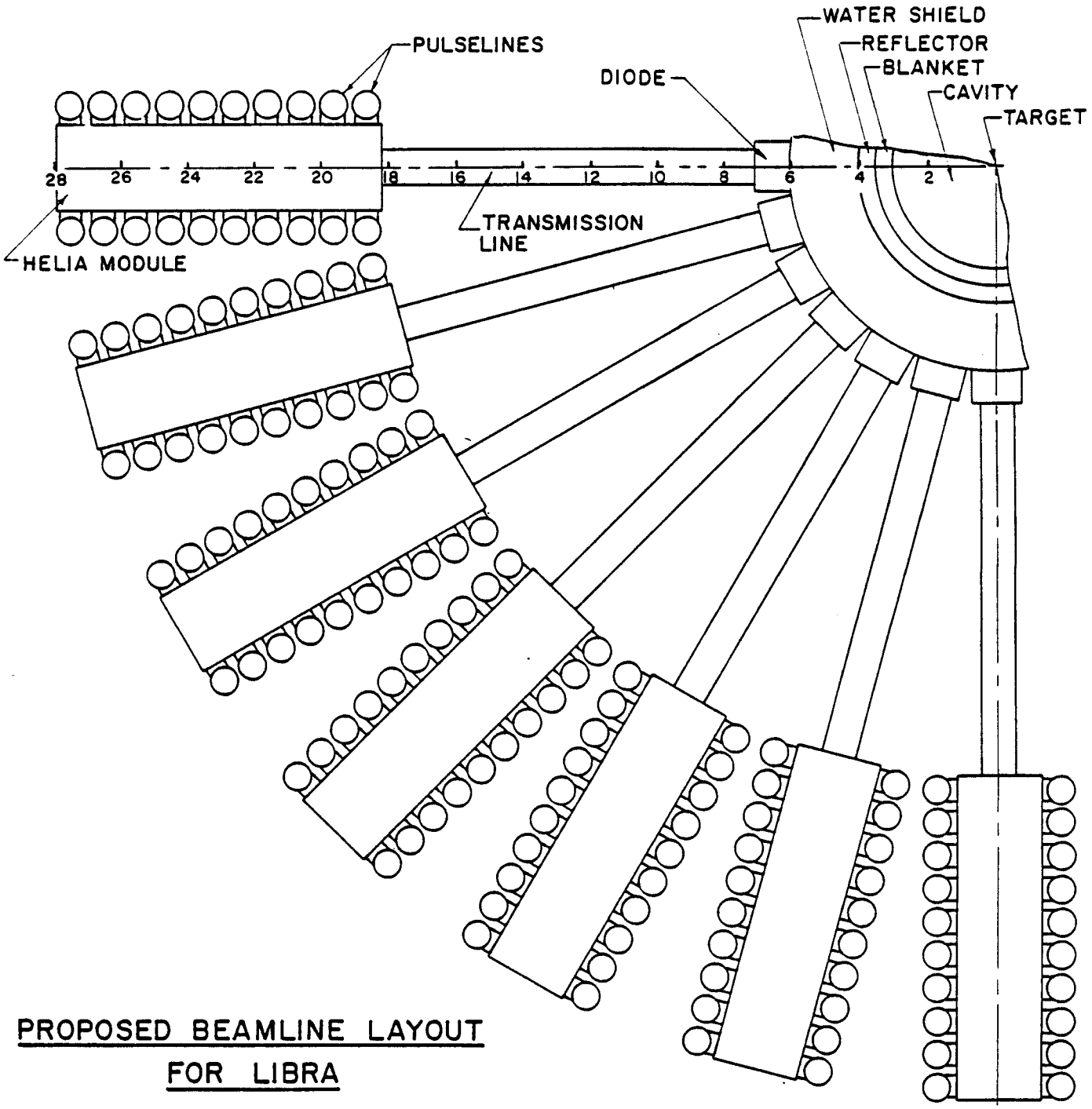


Fig. 4.1. Overhead view of the beam line layout for LIBRA with the latest driver design.

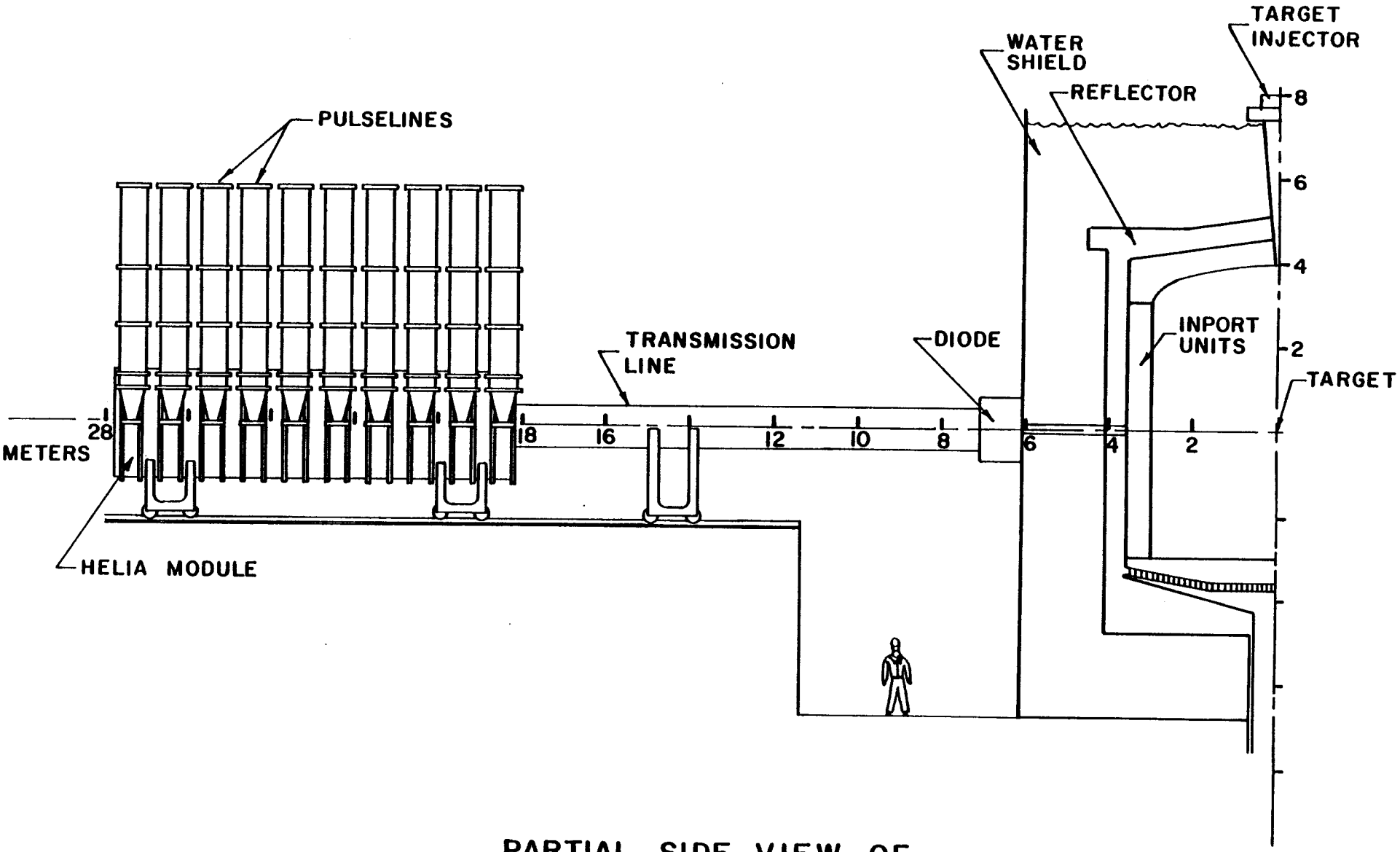


## PARTIAL SIDE VIEW OF
## LIBRA DEMONSTRATION POWER REACTOR

Fig. 4.2. Partial side view of LIBRA with the latest driver design.

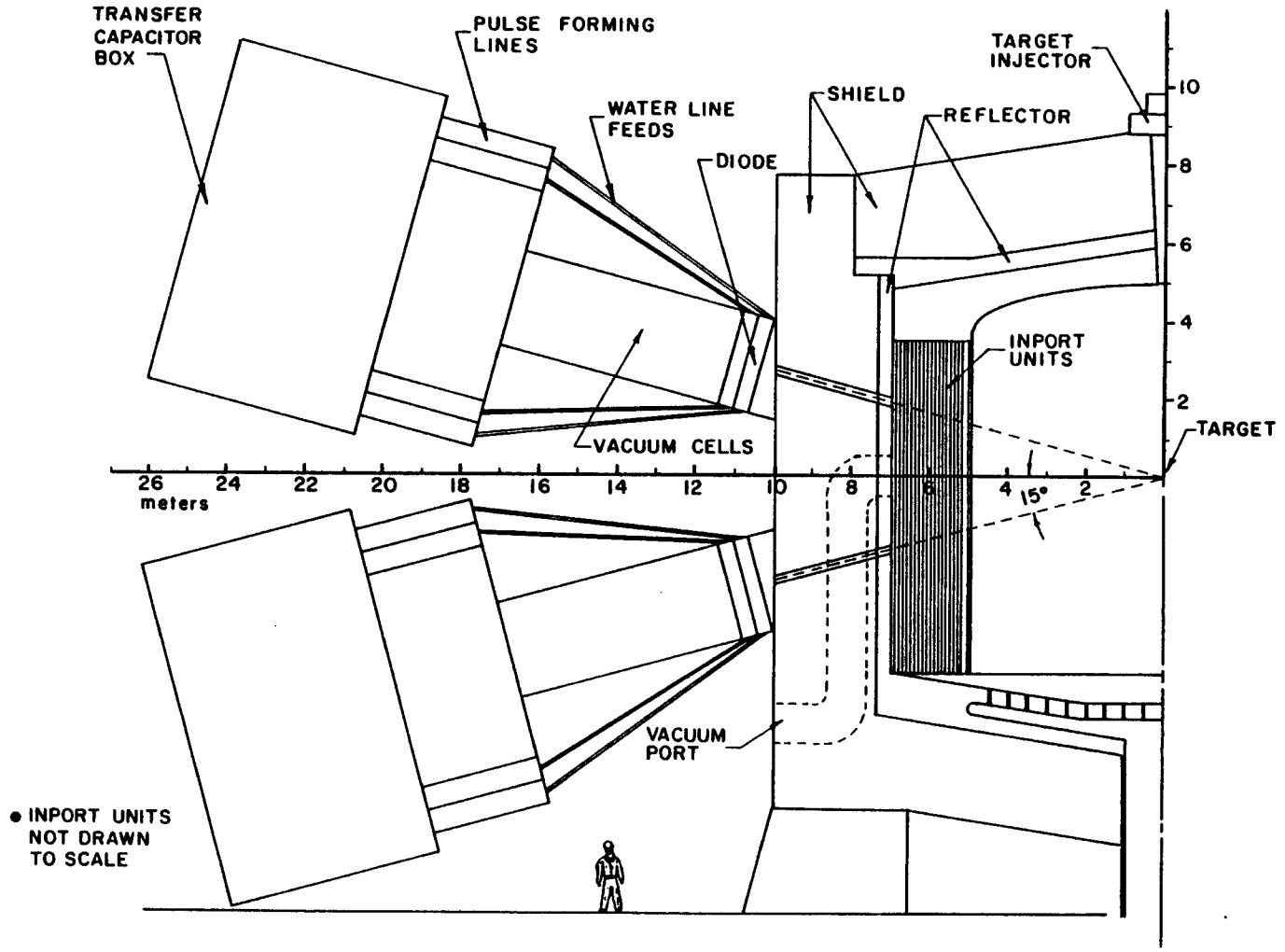


PARTIAL SIDE VIEW OF

LIBRA DEMONSTRATION POWER REACTOR

Fig. 4.3. Partial side view of LIBRA with the old driver design.

propagated at the speed of light, there is a relationship between the time that each diode fires and the length of transmission line between the diode and its HELIA module. Therefore, one can arrange a system where the ions from some diodes arrive at the target before ions from other diodes. An example of such a system for LIBRA is shown in Fig. 4.4, where all of the diodes are the same distance from the target, but some of the HELIA modules have been moved up closer to their diodes. The pulsed power modules are all triggered at the same time by a common laser system, so the pulse lines with the shortest transmission lines will accelerate the ions that reach the targets first. The pulse shape for this layout is shown in Fig 4.5. The beams that make the prepulse are not bunched as the main part of the pulse is, so the prepulse has a duration of 50 ns, while the main pulse lasts 17 ns. The same pulse shape could be achieved with the geometrical layout shown in Fig. 4.1 by firing some of the pulsed power modules earlier. This could be easily done by varying the path lengths for the light traveling from the master laser oscillator to the various HELIA modules.

### 4.1.2 Neutronics Analysis

The blanket in LIBRA is required to breed tritium and convert the kinetic energy of the fusion reaction into heat. The energy multiplication (M) should be as high as possible due to its impact on the cost of electricity. Varying the design parameters results in different effects on both tritium breeding ratio (TBR) and M.[4] Increasing TBR usually results in decreasing M. Hence, the goal of the design is to obtain a TBR that exceeds unity by a small margin that accounts for any deficiencies and uncertainties in the calculational models and cross section data used and to allow for tritium losses and radioactive decay and supplying fuel for startup of other fusion reactors. A value

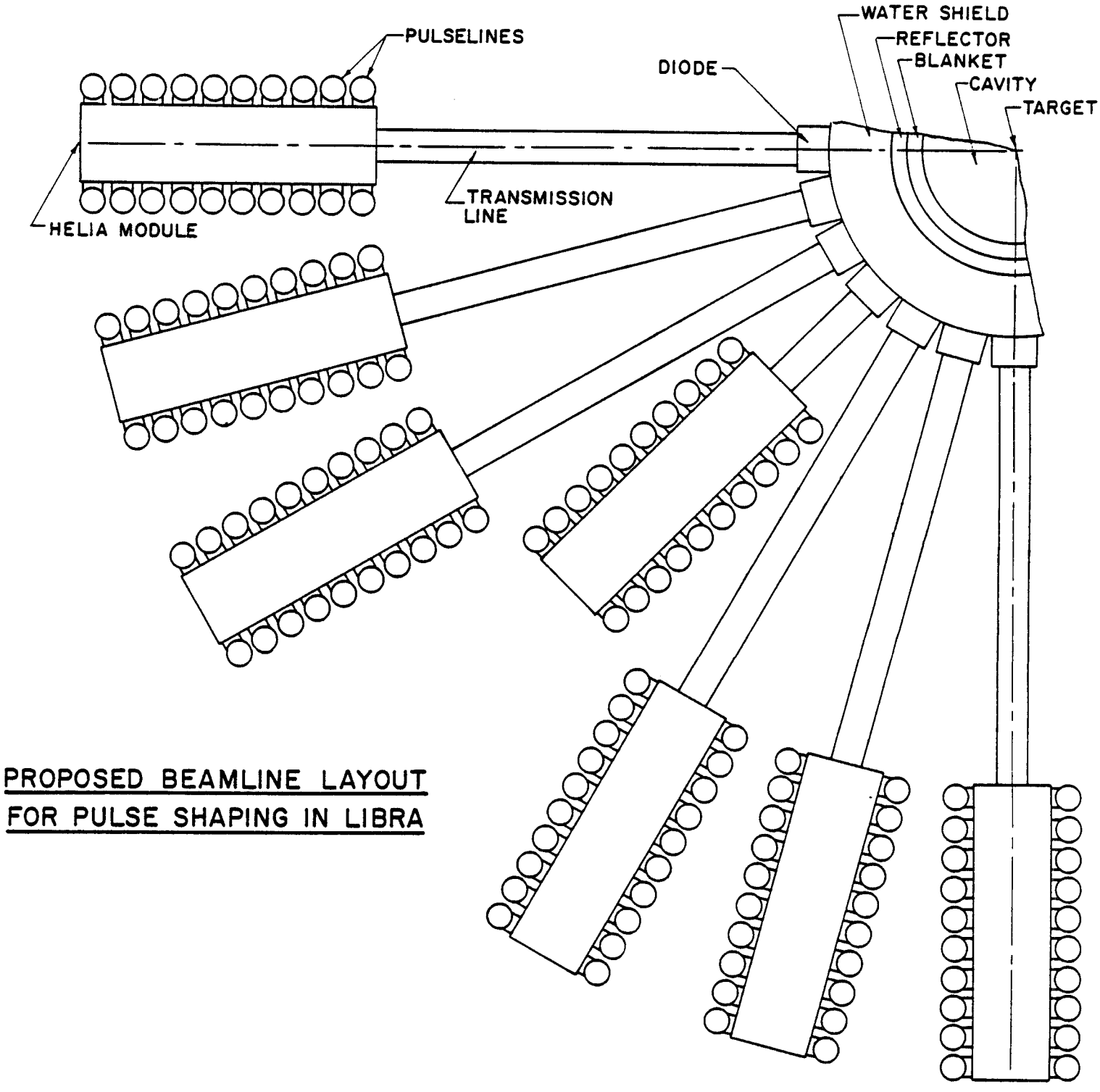


Fig. 4.4. Overhead view of the beam line layout for LIBRA in the shaped-pulse mode.

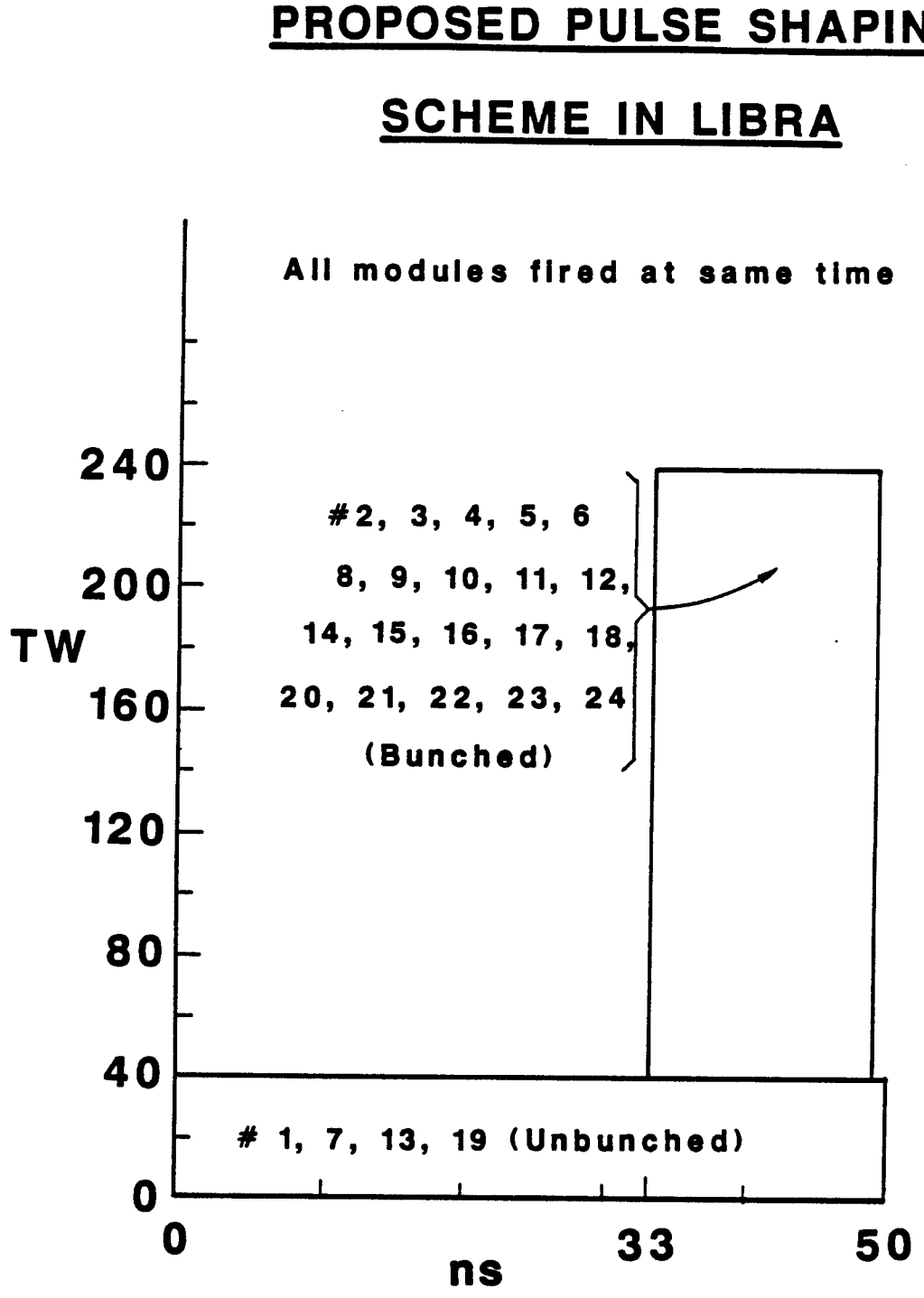


Fig. 4.5. Shaped ion pulse on the target in LIBRA.

of 1.1 is usually required from the three-dimensional calculations. In this work a one-dimensional value of ~ 1.15 is required for the TBR. For ICF reactors, we define two energy multiplication factors: nuclear energy multiplication ($M_n$) and overall energy multiplication ($M_o$). $M_n$ is the nuclear energy ($n + \gamma$) deposited in the blanket and reflector divided by the fusion neutron energy incident on the blanket. The overall energy multiplication is defined as the total energy deposited in the system, including the energy deposited by x-rays and target ion debris at the first surface of the blanket, divided by the DT fusion reaction yield. Another goal of the design is to reduce the radiation damage in the first metallic wall to values that eliminate the need for replacement during the reactor lifetime, estimated to be 10 full power years (FPY). A lifetime dpa limit of 200 dpa is considered for the ferritic steel alloy HT-9 used as the metallic structure in LIBRA. Hence, a dpa rate limit of 20 dpa/FPY is used.

A series of one-dimensional neutronics and photonics calculations was made to determine the best blanket design parameters that satisfy the design goals mentioned above. The calculations were performed in spherical geometry using the one-dimensional discrete ordinates code ONEDANT[5] and the $P_3$ - $S_8$ transport approximation. A coupled 30 neutron-12 gamma group cross section library based on the ENDF/B-V evaluation was used.[6] A schematic of the geometrical model used in the calculations is given in Fig. 4.6. The blanket consists of INPORT tubes[7] with a packing fraction of 0.33. The tubes are made of SiC and are filled with $Li_{17}Pb_{83}$. The SiC occupies 2% of the tube volume. The inner blanket surface is at a 3 m distance from the target. The blanket is backed by a HT-9 reflector with 10 v/o $Li_{17}Pb_{83}$ coolant. A 2 m thick water shield was used in the calculations. The neutron source was con-

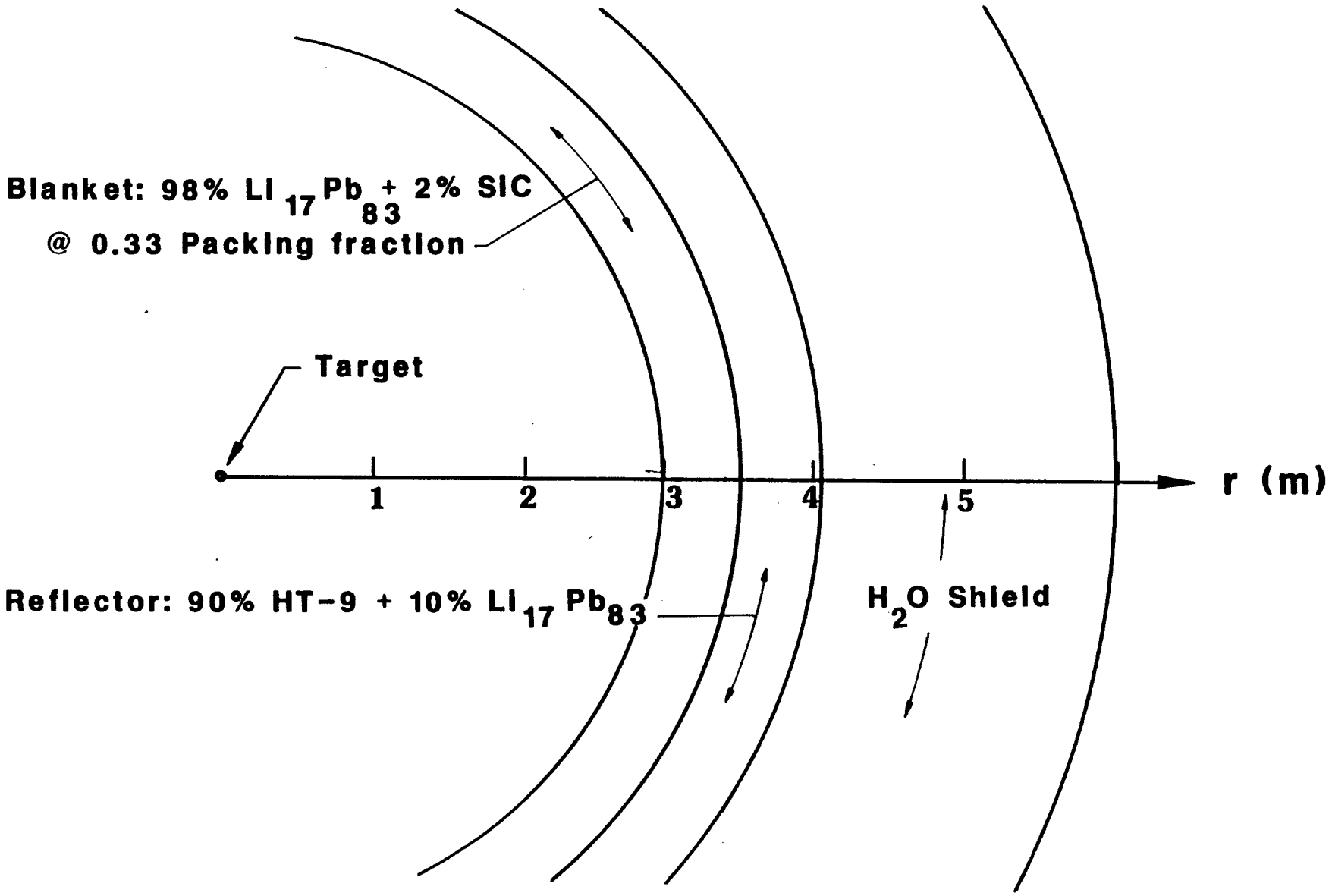


Fig. 4.6. Schematic of neutronics calculational model.

sidered to be an isotropic point source at the center of the cavity. The HIBALL target spectrum[7] was used to represent the energy dependence of the source neutrons. 72% of the target yield is carried by neutrons with an average energy of 12 MeV. A neutron multiplication factor of 1.046 in the target was taken into account. The gamma source from the target was neglected as the gammas carry only 0.15% of the target yield. The results were normalized to a DT yield of 320 MJ and a repetition rate of 1.5 Hz that yields 480 MW of fusion power.

The design parameters varied in the calculations are the blanket thickness, the reflector thickness, and the lithium enrichment. Table 4.2 gives the nuclear parameters calculated for the ten cases considered. In case 1, a 2 m thick blanket zone with natural Li in $Li_{17}Pb_{83}$, which is similar to the HIBALL design, was used. Due to the soft spectrum almost all tritium breeding occurs in $^6Li$, and enriching Li is beneficial when $Li_{17}Pb_{83}$ is used. The effect of enrichment was investigated in case 2 when 90% $^6Li$ was used. This resulted in increasing the TBR by 40% while $M_0$ decreased by 6% and the peak dpa rate in HT-9 dropped by a factor of two. Since the TBR in case 2 is excessive, the blanket thickness was reduced in cases 4, 6 and 8. Figure 4.7 shows the effect of blanket thickness on TBR and $M_0$ for 90% $^6Li$. It is clear that one can achieve the required TBR by reducing the blanket thickness to 0.55 m. This also results in increasing $M_0$ by 3%. The effect of blanket thickness on peak dpa rate in HT-9 is shown in Fig. 4.8. The dpa rate increases by a factor of 15 as the blanket thickness was reduced from 2 m to 0.55 m. However, the dpa rate of 18 dpa/FPY obtained in case 8 is acceptable for a reactor lifetime of ~ 10 FPY. It is clear from the results of Table 4.2 that reducing the blanket thickness yields unacceptable TBR if natural Li is used.

Table 4.2. Nuclear Parameters for LIBRA

| Case | $\Delta_B$ (m) | $\Delta_r$ (m) | % $^6$Li | TBR | $M_n$ | $M_o^*$ | Peak Heat dpa/FPY |
|---|---|---|---|---|---|---|---|
| 1 | 2 | 0.5 | 7.42 | 1.152 | 1.366 | 1.250 | 2.44 |
| 2 | 2 | 0.5 | 90 | 1.625 | 1.259 | 1.174 | 1.21 |
| 3 | 1.5 | 0.5 | 7.42 | 0.957 | 1.407 | 1.280 | 5.37 |
| 4 | 1.5 | 0.5 | 90 | 1.549 | 1.278 | 1.189 | 3.12 |
| 5 | 1.0 | 0.5 | 7.42 | 0.715 | 1.451 | 1.312 | 11.63 |
| 6 | 1.0 | 0.5 | 90 | 1.406 | 1.293 | 1.200 | 7.95 |
| 7 | 1.0 | 0.5 | 35 | 1.168 | 1.346 | 1.237 | 9.89 |
| 8 | 0.55 | 0.5 | 90 | 1.162 | 1.309 | 1.211 | 18.0 |
| 9 | 1.0 | 0.8 | 35 | 1.175 | 1.377 | 1.258 | 9.71 |
| 10 | 0.55 | 0.85 | 90 | 1.177 | 1.374 | 1.238 | 17.61 |

$$M_o = \frac{(0.18 + 0.72\ M_n)\ 0.99\ E_{DT}}{E_{DT}}$$

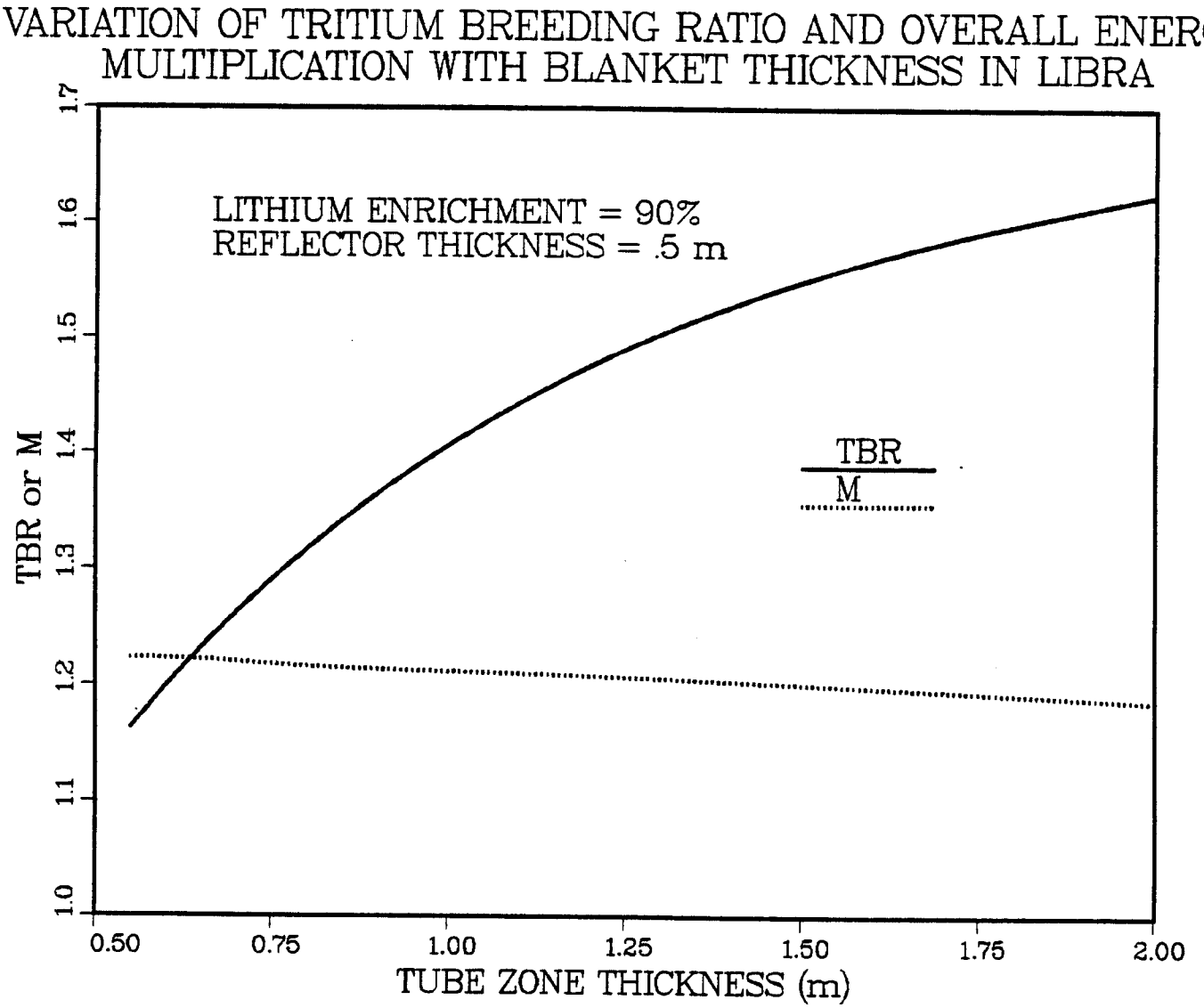


Fig. 4.7. Variation of tritium breeding ratio and overall energy multiplication with blanket thickness in LIBRA.

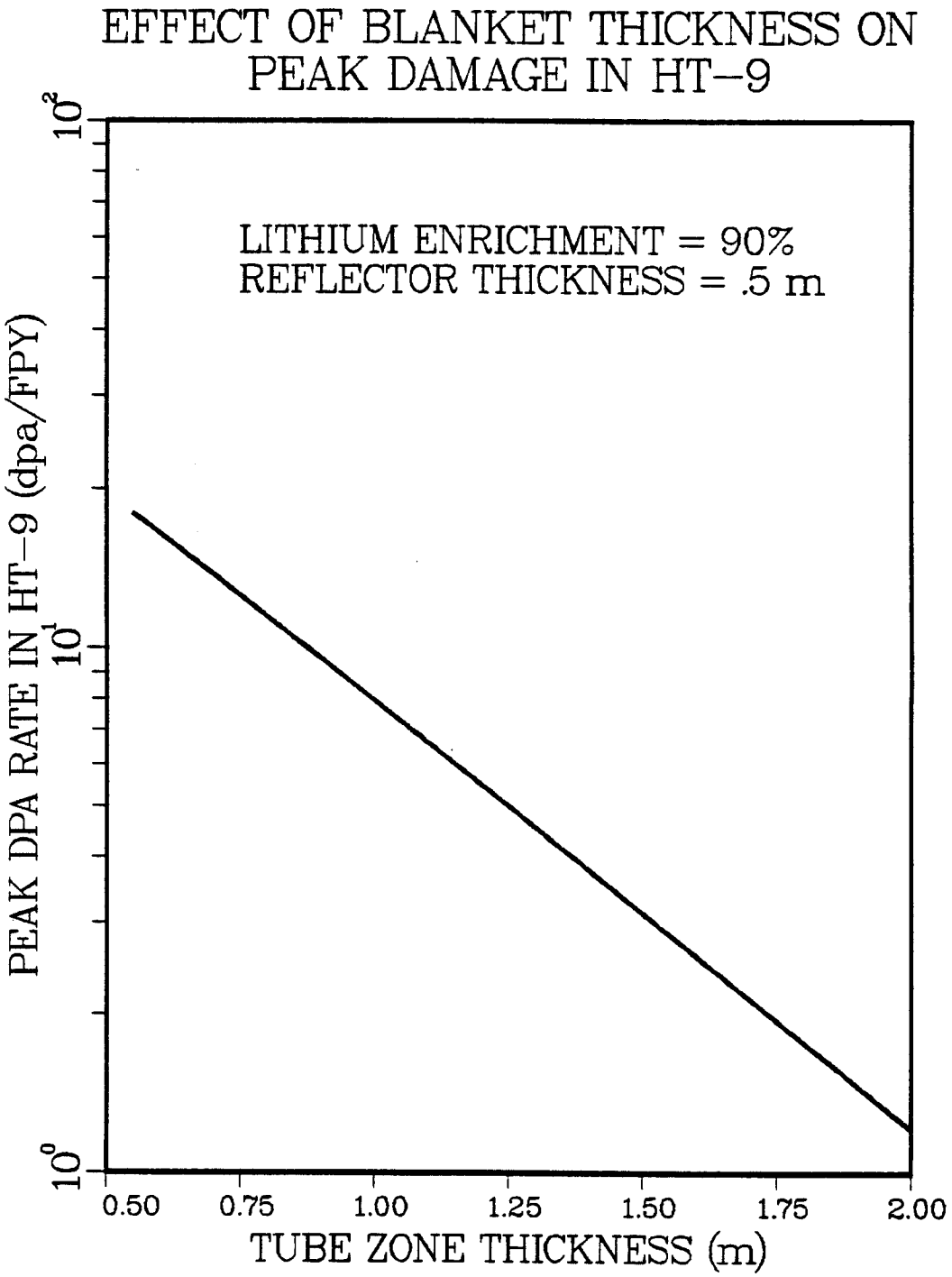


Fig. 4.8. Effect of blanket thickness on peak damage in HT-9.

Fixing the blanket thickness at 1 m we varied the enrichment and found that 35% $^{6}Li$ yields the required TBR. In this case (case 7) $M_0$ is 2% larger than that in case 8 while the dpa rate is about half that in case 8. However, case 7 has a 0.45 m thicker blanket. Further improvement in energy multiplication for cases 7 and 8 was obtained by increasing the metallic reflector thickness. However, this improvement is only ~ 2%.

Since the reactor size determined by the blanket and reflector thickness has significant impact on the cost of the reactor and insignificant enhancement of $M_0$ was obtained with thicker blankets and reflectors, we chose case 8 for the LIBRA design. This yields a savings of 1.45 m in total blanket and reflector thickness compared to the starting design (case 1) and only a 3% drop in $M_0$. Only 0.2% of tritium breeding results from the $^{7}Li(n,n\alpha)t$ reaction. The nuclear heating is produced equally by neutron and gamma heating.

## 4.2 Drag Force Considerations on the LIBRA INPORT Tubes

The calculation of the time dependent drag force on the LIBRA tubes is a very difficult problem. One could perform a detailed finite-difference calculation to determine it. However, this approach would be computationally intensive. Katz[8] appears to have attempted this. His grid is much too coarse to provide meaningful results. A second approach is to formulate the problem as one of determining the time dependent drag coefficients (an analogy to typical steady-state calculations). The total force on the body can be defined as:

$$K = C_D \, q \, A \, .$$

Here, $C_D$ is the drag coefficient, q is the dynamic pressure ($1/2 \, \rho u^2$), and A

is the cross sectional area of the object. Unfortunately, unsteady drag coefficients are rarely available in the open literature, but fortunately, two sources have been located.

Heilig[9] presents data for supersonic flow past a half-circular cylinder; he assumed symmetric flow fields. Figure 4.9 shows the experimental time-dependent drag coefficients. One will note that as the Mach number increases, the drag coefficient is smaller; this could be due to the decreased Mach cone at higher incident Mach numbers. Heilig also compares his experimental results with three simple relations: (1) the time required to reach the peak maximum loading is approximately D/(3U), where U is the shock velocity, D is the diameter; (2) the duration of the diffraction loading pulse is 2D/U; (3) the peak loading pulse can be estimated to be 5/3 ($\Delta p$), where $\Delta p$ is the free-field overpressure. Heilig's data agree with these expressions.

The second source was an AWRE report.[10] This data was for subsonic conditions. Figure 4.10 is from this report. One will note two things: the drag coefficients are lower than the supersonic data of Heilig (note the increasing function as the flow becomes supersonic) and the dependence of the drag coefficient of the Reynolds number.

The drag force on each of the rows of LIBRA INPORT tubes could be obtained from a control volume approach to the problem. Thus, a 1-D finite-difference code could be modified to include the drag coefficients in certain meshes. This approach is similar to a current 2-D problem under investigation: shock induced flow in a porous media.

A literature search was done to investigate the effects of the shock precursor on the drag force. They[11-13] were inconclusive.

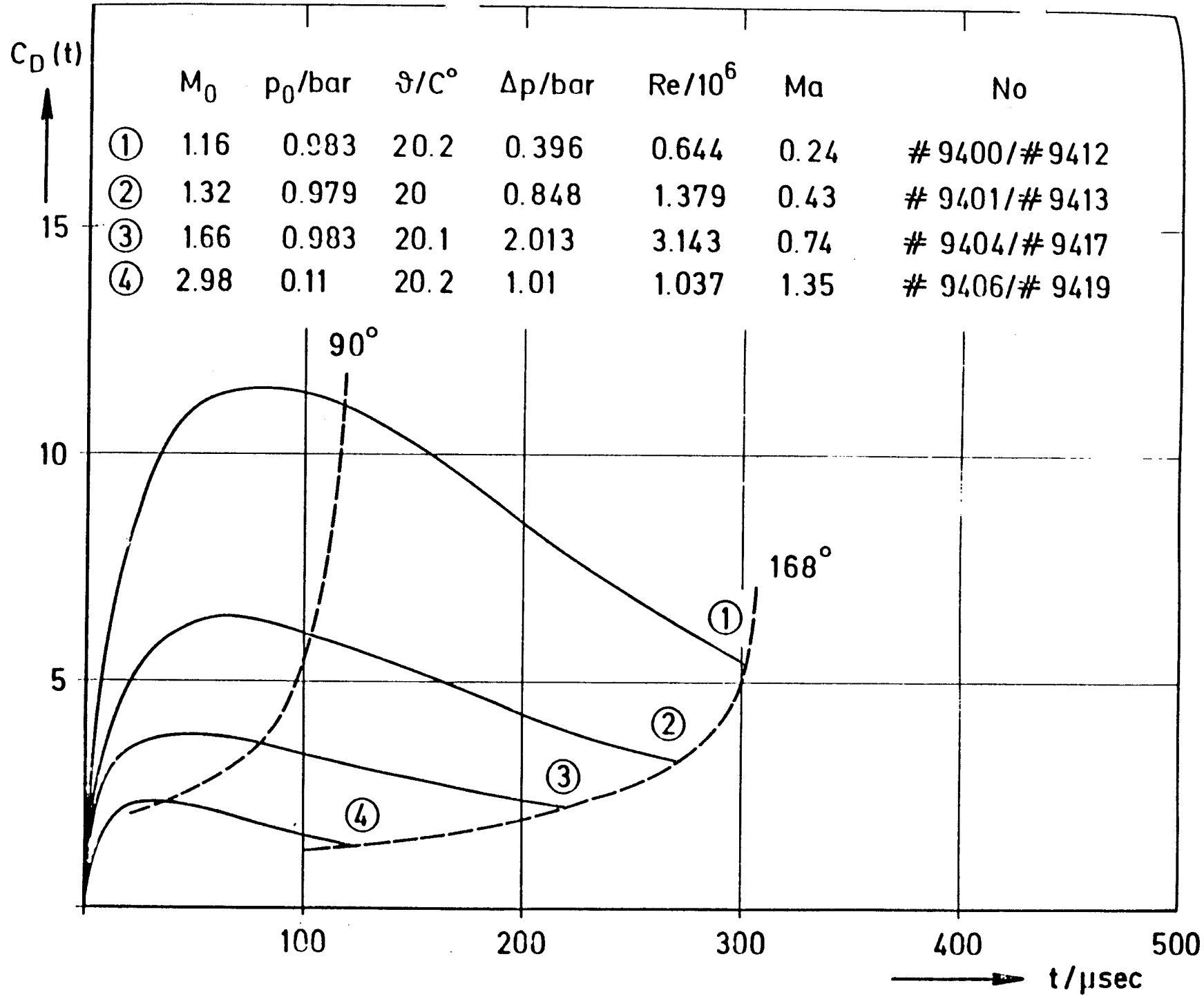


Fig. 4.9. Measurements of time-development drag coefficients $C_D(t)$ during the diffraction loading period of shock waves on a cylinder with diameter D = 0.1 m.

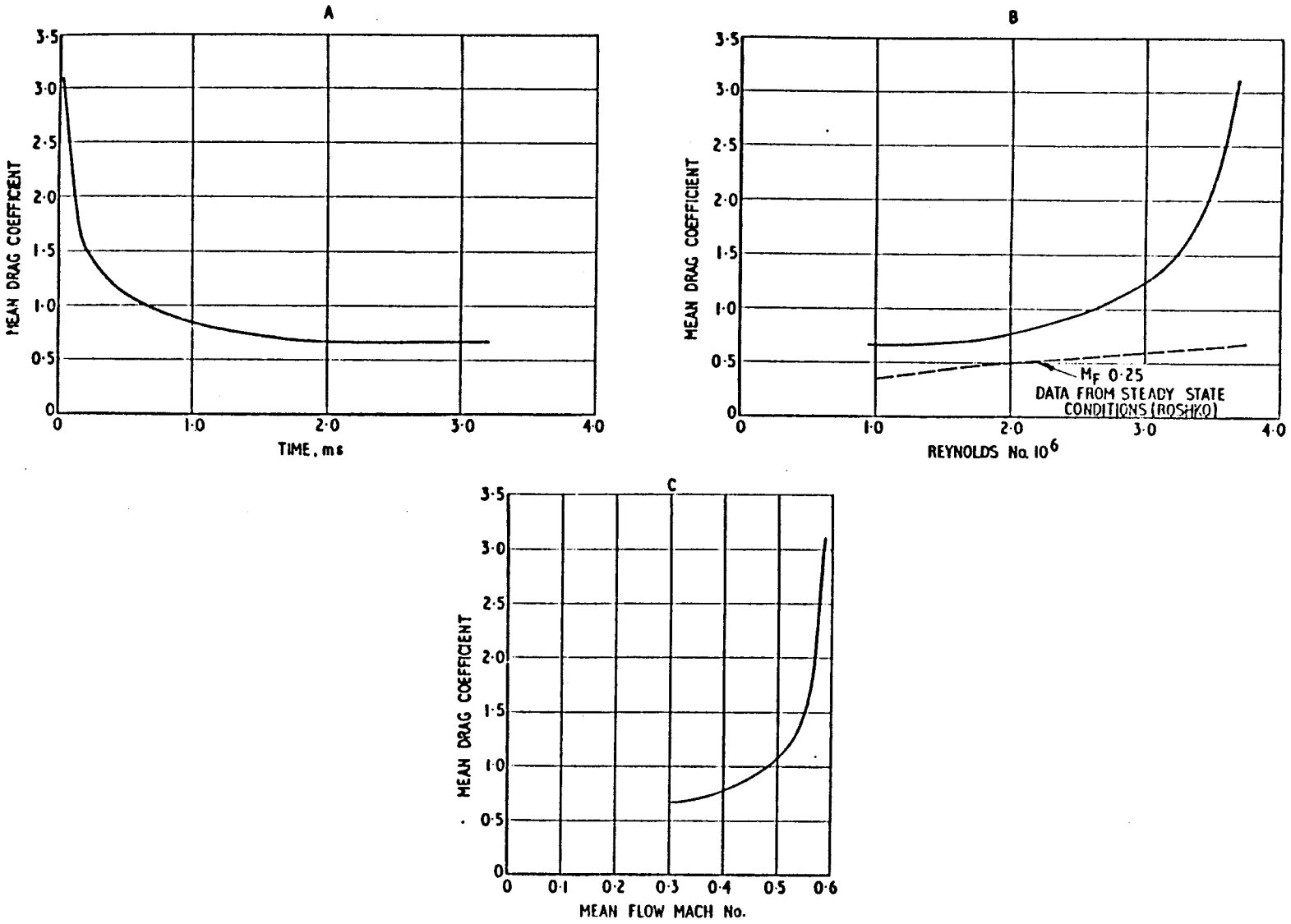


Fig. 4.10. Smoothed average drag coefficients plotted agains A - Time, B - Reynold's number, and C - Flow mach number.

## 4.3 LIBRA Cavity Thermal-Hydraulic Design

During this year we have performed scoping calculations in order to set the thermal-hydraulic boundary conditions for the LIBRA cavity. Since this task was not given a high priority during the year only an overall heat transfer analysis was performed. Similar to the HIBALL design the cavity is designed to have two types of INPORT tubes: the front rows being of small diameter and the back rows large diameter. The lithium-lead coolant mass flow is split between these two types of tubes to minimize the time-averaged hot spot temperature on the outer tube wall to be below 550°C (Fig. 4.11). Based on a time-averaged analysis we have found the maximum temperature to be 544°C (Table 4.3), while keeping the INPORT front row tube velocity relatively low (1.5 m/s). We have not done a detailed assessment of the condensation rate in this design although we expect it to be within the time scale of 660 ms.

## 4.4 Target Explosion Generated Fireballs

In the past, the MFFIRE computer code[14] has been used to calculate the thermal and mechanical loads on the INPORT tubes for the case where the tubes are five meters from the target.[15] The pressure on the INPORT tubes is shown as a function of time in Fig. 4.12. The maximum pressure is 0.18 MPa and the impulsive pressure used in the study of the behavior of the tubes is 87 Pa-s for the five meter case. The new geometry specifies that the tubes are three meters from the target explosion. If one uses strong shock theory,[16] the pressure scales as the inverse of the volume of gas behind the shock; so the peak pressure on the tubes for the three meter case should be 0.83 MPa. A simulation of the behavior of the target generated fireball has been done with MFFIRE for the three meter case, where all other parameters are the same as before. The peak pressure on the tubes was found to be 0.28 MPa,

Table 4.3. LIBRA Thermal-Hydraulic Parameters

| | |
|---|---|
| Total mass flow rate, $\dot{m}$ | 22,550 kg/s |
| INPORT front row tube velocity, $V_{sm}$ | 1.5 m/s |
| Inlet temperature, $T_{in}$ | 338°C |
| Outlet temperature, $T_{out}$ | 494°C |
| Inlet temperature back row INPORT tubes, $T_2$ | 384°C |
| Outlet temperature back row, $T_3$ | 526°C |
| Outlet temperature front row, $T_5$ | 422°C |
| Time-average hot spot temperature, $T_{max}$ | 544°C |

# CONCEPTUAL ARRANGEMENT OF INPORT COOLING

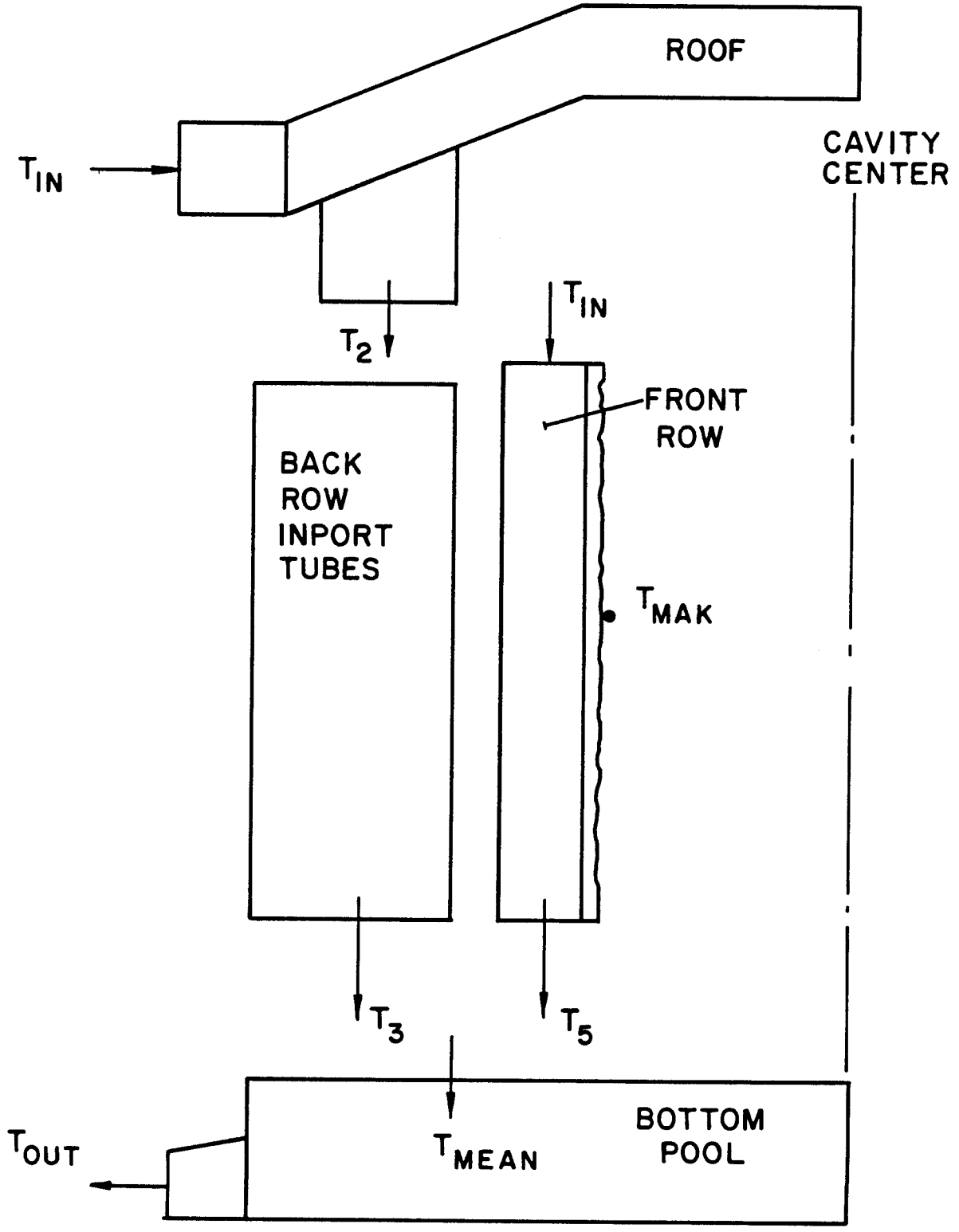


Fig. 4.11. Schematic heat flow in LIBRA INPORT tubes.

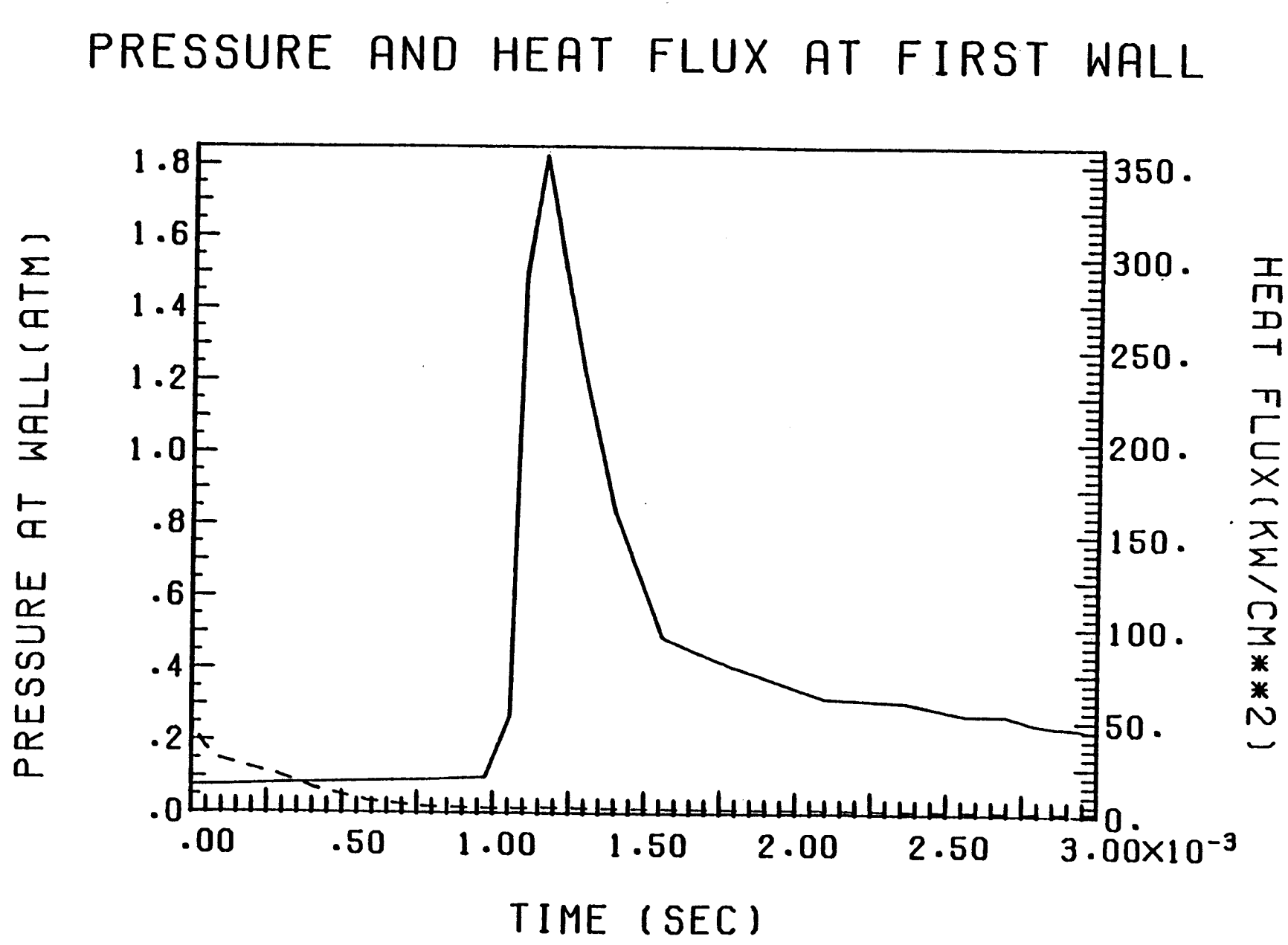


Fig. 4.12. Pressure on the INPORT tubes five meters from a 320 MJ target explosion versus time.

much less than the value predicted by strong shock theory. The impulsive pressure on the tubes, integrated out to a time of about 1.3 microseconds, was about 100 Pa-s. The details of this simulation give some idea of why the strong shock scaling is not valid.

The pressure on the first wall is shown as a function of time in Fig. 4.13. As mentioned before, the maximum pressure is 0.28 MPa, which occurs at a time of about 0.5 milliseconds. A second peak is seen at about 3 milliseconds, which is due to the shock that has reflected off of the tubes back onto the center of the cavity and then back out to the tubes. This peak only occurs if the target chamber is perfectly spherical, so it would not be seen in the LIBRA design. The time integral of the pressure, which we refer to as the impulsive pressure, measures the mechanical load on the INPORT tubes. This is shown as a function of time in Fig. 4.14. Once the pressure in Fig. 4.13 becomes constant, we can assume that the pressure is equalized on all sides of the tubes and the tubes experience no net force from the gas pressure. For this case, this occurs at about 1.3 milliseconds. The impulsive pressure at this time is about 100 Pa-s.

The emission of radiant energy from the fireball has something to do with why the peak pressure does not scale with radius as predicted by strong shock theory. The radiant heat flux on the INPORT tubes is shown as a function of time in Fig. 4.15. There is a very short but intense pulse followed by a rather long pulse of a lower intensity. There is a total of 75 MJ in this pulse, most of it being in the second longer burst. This may be compared with roughly 86 MJ in target x-rays and ions, 81 MJ of which are deposited in the gas, and with the 54 MJ emitted in the five meter case. Instead of scaling just as the inverse of the volume behind the shock, the pressure is propor-

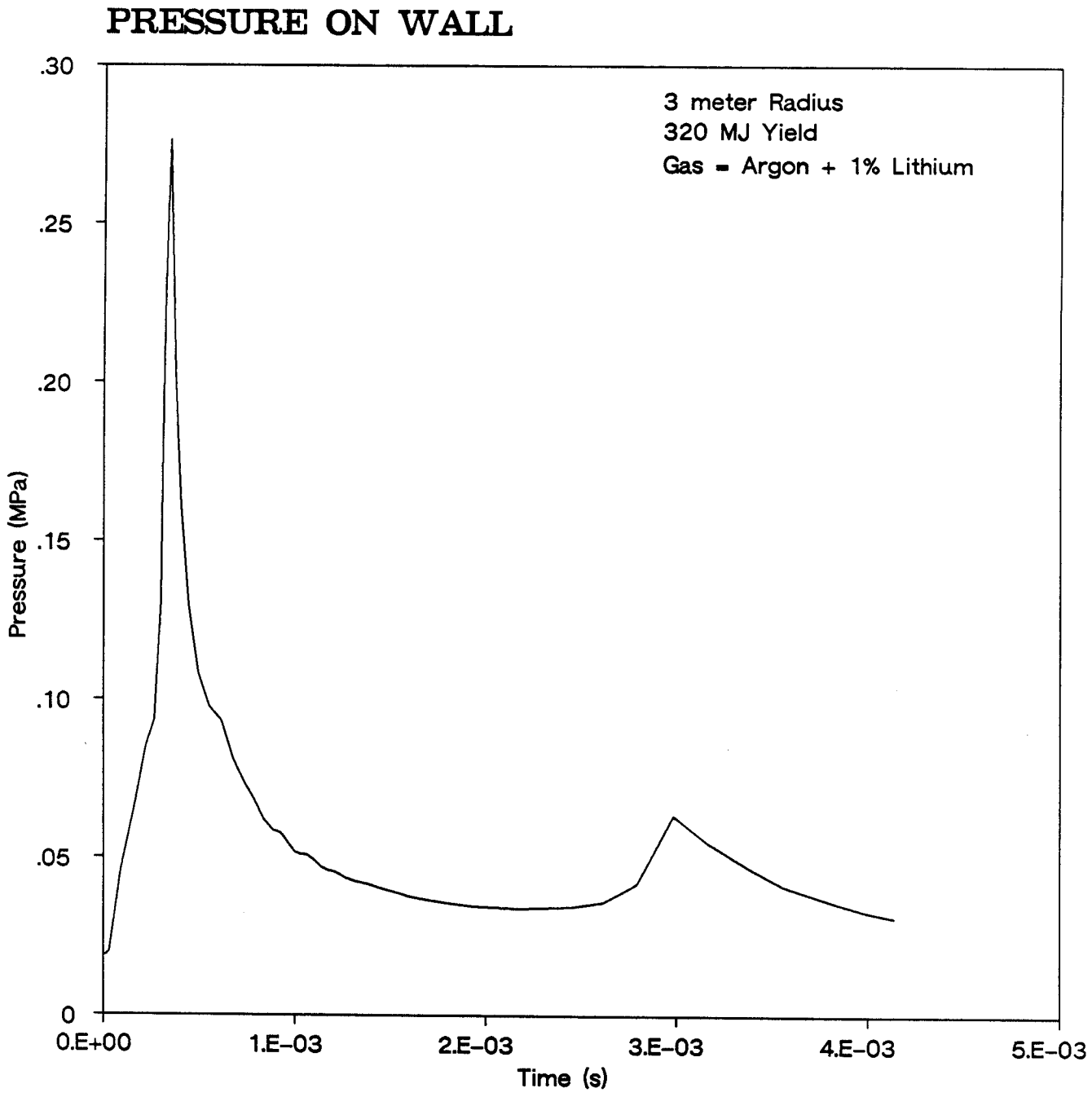


Fig. 4.13. Pressure on the INPORT tubes three meters from a 320 MJ target explosion versus time.

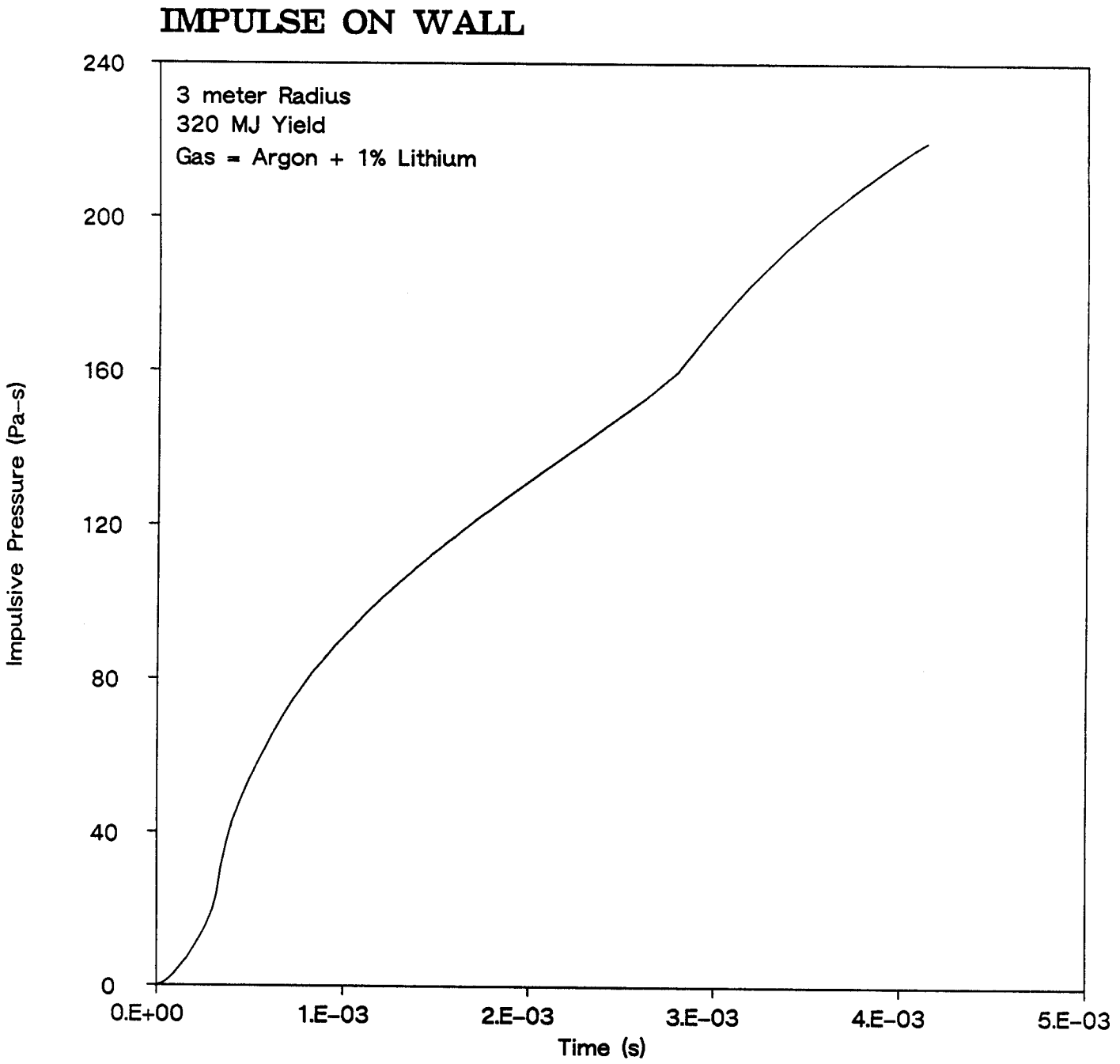


Fig. 4.14. Impulsive pressure on the INPORT tubes three meters from a 320 MJ target explosion versus time.

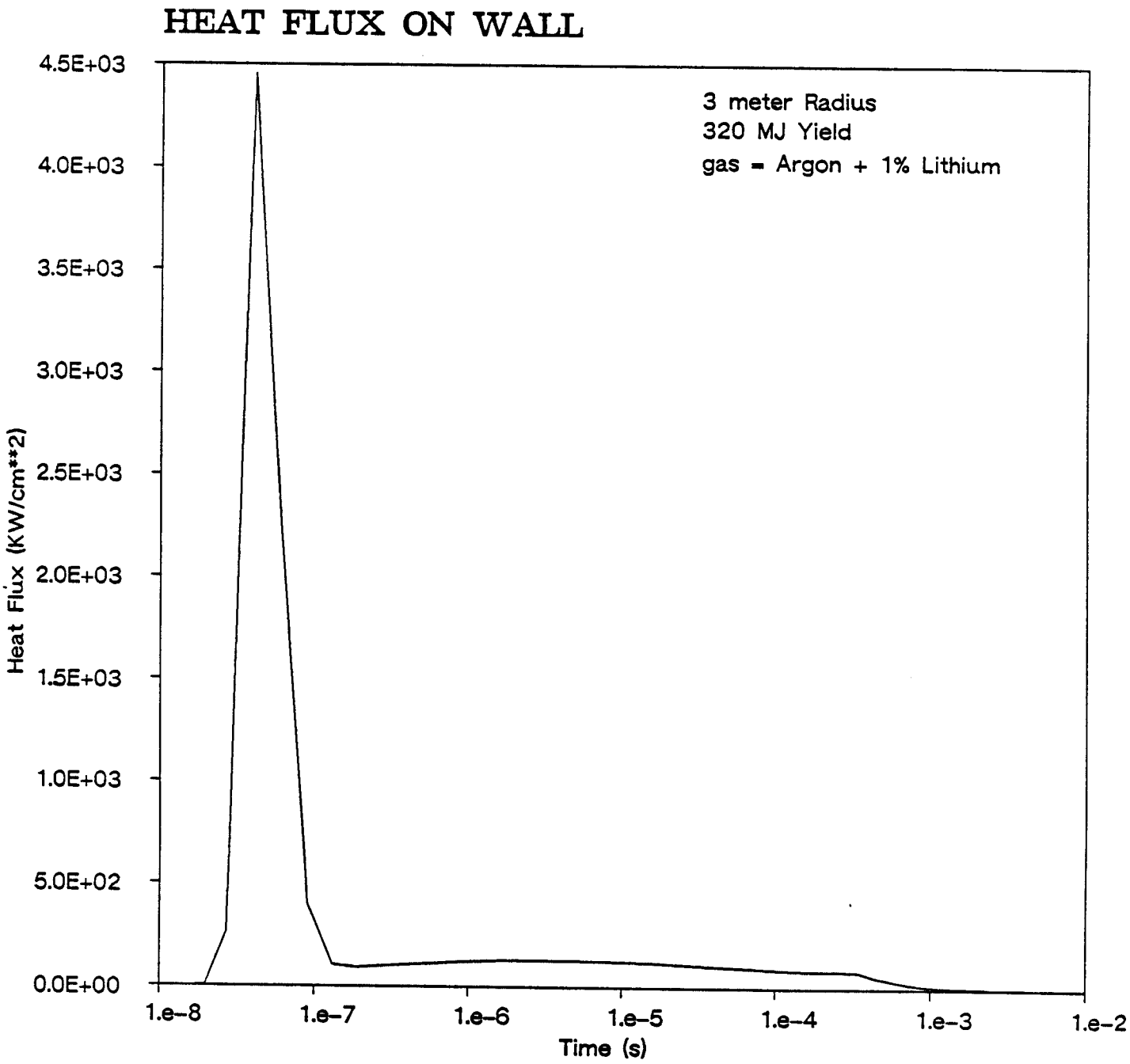


Fig. 4.15. Heat flux on the INPORT tubes three meters from a 320 MJ target explosion versus time.

tional to the ratio of energy behind the shock to the volume. This does not account for all of the reduction from the strong shock prediction.

We have shown in previously published work[17] that the heating of the gas in front of a shock can reduce the shock overpressure. There is significantly less x-ray heating of the gas in front of the tubes in the five meter case than in the three meter case. In the five meter case, the gas at the INPORT tubes has been heated to 0.135 eV, while it is heated to 0.333 eV in the three meter case. Therefore, the shock strength should be reduced for the 3 meter case by the x-ray preheat effect.

## 4.5 Structural Mechanics of INPORT Tubes

Cavity design and layout includes determination of INPORT spacing which in turn depends upon the maximum displacement of the tubes under operating conditions. The sequential impulsive pressure loadings produce INPORT motion characterized by a periodic radial excursion, out and in, about a mean deflected shape. The maximum amplitude of this response is a function primarily of the impulse magnitude, the proximity of the forcing frequency to natural frequencies of the INPORTs and to a lesser degree, the damping in the system. Natural frequencies depend upon the lithium-lead flow rate, unsupported length and axial stress.

Mechanical response calculations have been made using a code developed at the University of Wisconsin. Since the LIBRA cavity design has not been completely finalized, numerical values were developed in parametric form. Natural frequency results for 10 meter INPORTs are shown in Fig. 4.16 as a function of mean tensile force. Weight produces an axial gradient but it has been shown in earlier studies that an accurate assessment of the gradient may be made by using the mean tensile force in the dynamic analysis. In Figs.

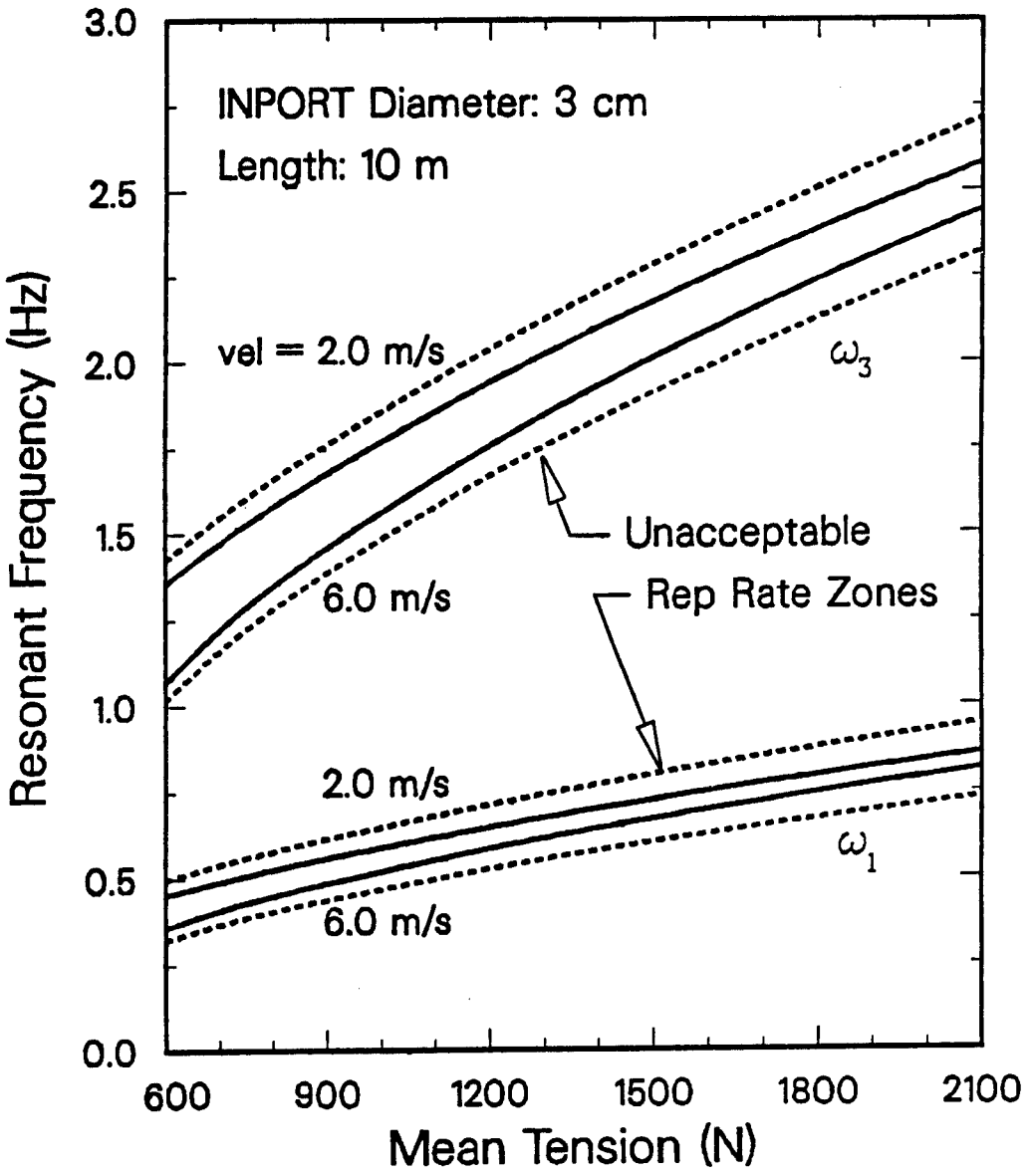


Fig. 4.16. Natural frequencies of 10 meter long INPORT tubes versus tensile loading.

4.16 and 4.17 the "windows" were established from variations of ±10% and ±5% on the first and third harmonics, respectively. The second harmonic is not relevant since unsymmetric modes will not respond to symmetric impulsive pressure distributions. From Fig. 4.16 it can be seen that for a driver frequency of 1.5 Hz, resonance is not an issue for the fundamental frequency and that the limit for the third harmonic will be above 1.5 Hz for mean tensile loads greater than 1014 N and all flow rates of interest. From the results of Fig. 4.17, resonance will not develop for 6 m INPORTs for the third harmonic but the window on the first harmonic requires that mean tensile loads do not exceed 1903 N.

Maximum dynamic displacements of the INPORTs are shown in Fig. 4.18 for a mean tensile load of 1500 N. At a given impulsive pressure, a decrease in length from 10 m to 6 m as well as flow reductions both result in smaller displacements. The corresponding results for a mean tension of 1800 N are shown in Fig. 4.19. Decreasing the length from 10 m to 6 m substantially reduces the dynamic displacement. Lowering the flow rate will reduce motion for the 10 m INPORT but produce the opposite effect with the shorter 6 m INPORT. In this case, a near-resonant condition exists with the 1.5 Hz driving frequency slightly above the fundamental harmonic. Decreasing the flow rate raises this natural frequency closer to 1.5 Hz at 1800 N, and thus results in larger dynamic displacements. (The opposite result would occur with the driving frequency just below the fundamental.)

The first wall pressure-time history for the 3 m radius cavity has been shown in Fig. 4.13. Since the mean pulse width of this loading is small compared with INPORT vibration periods, it may be considered as an impulsive distribution for all practical purposes. In addition, the constant pressure

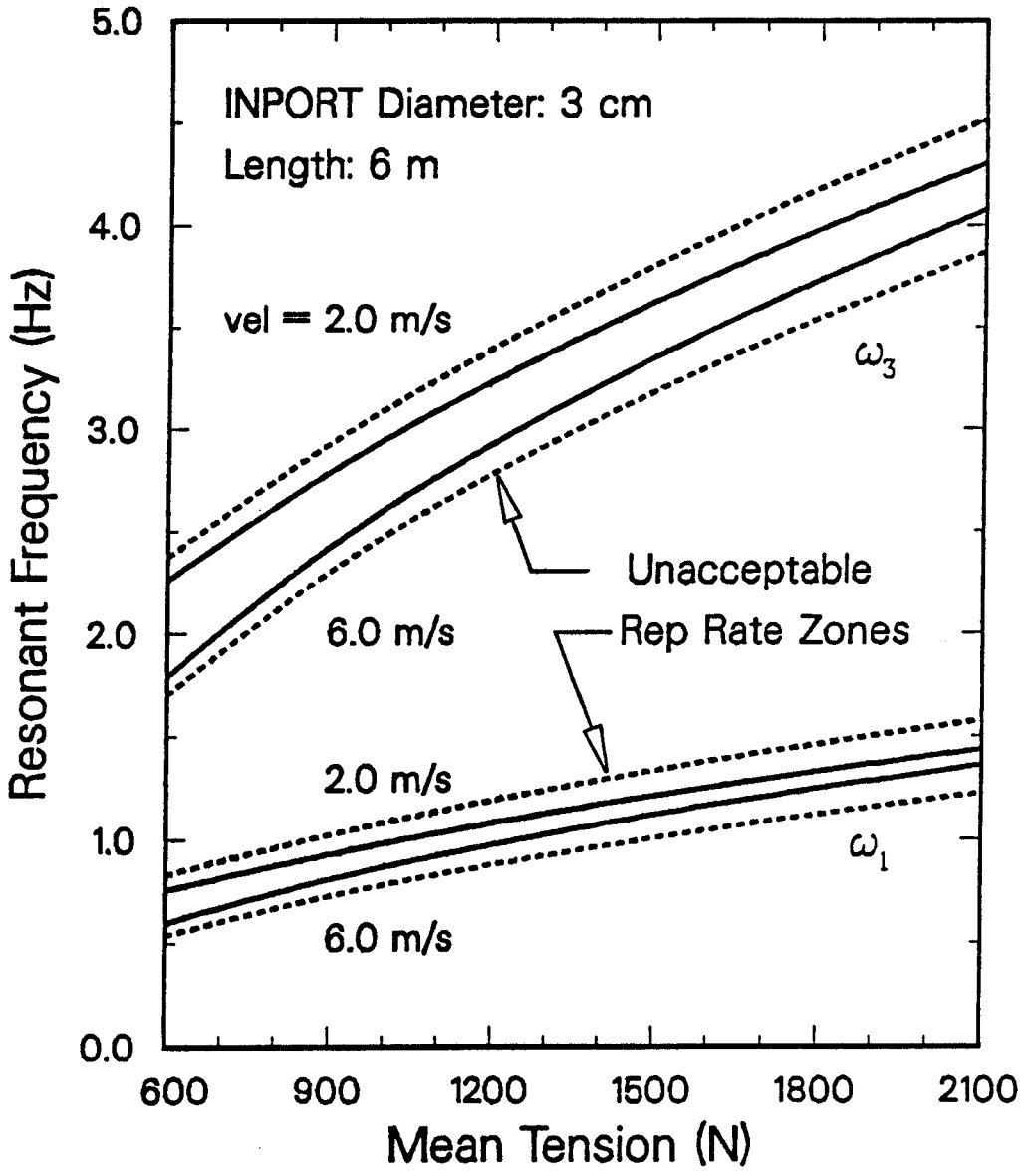


Fig. 4.17. Natural frequencies of 6 meter long INPORT tubes versus tensile loading.

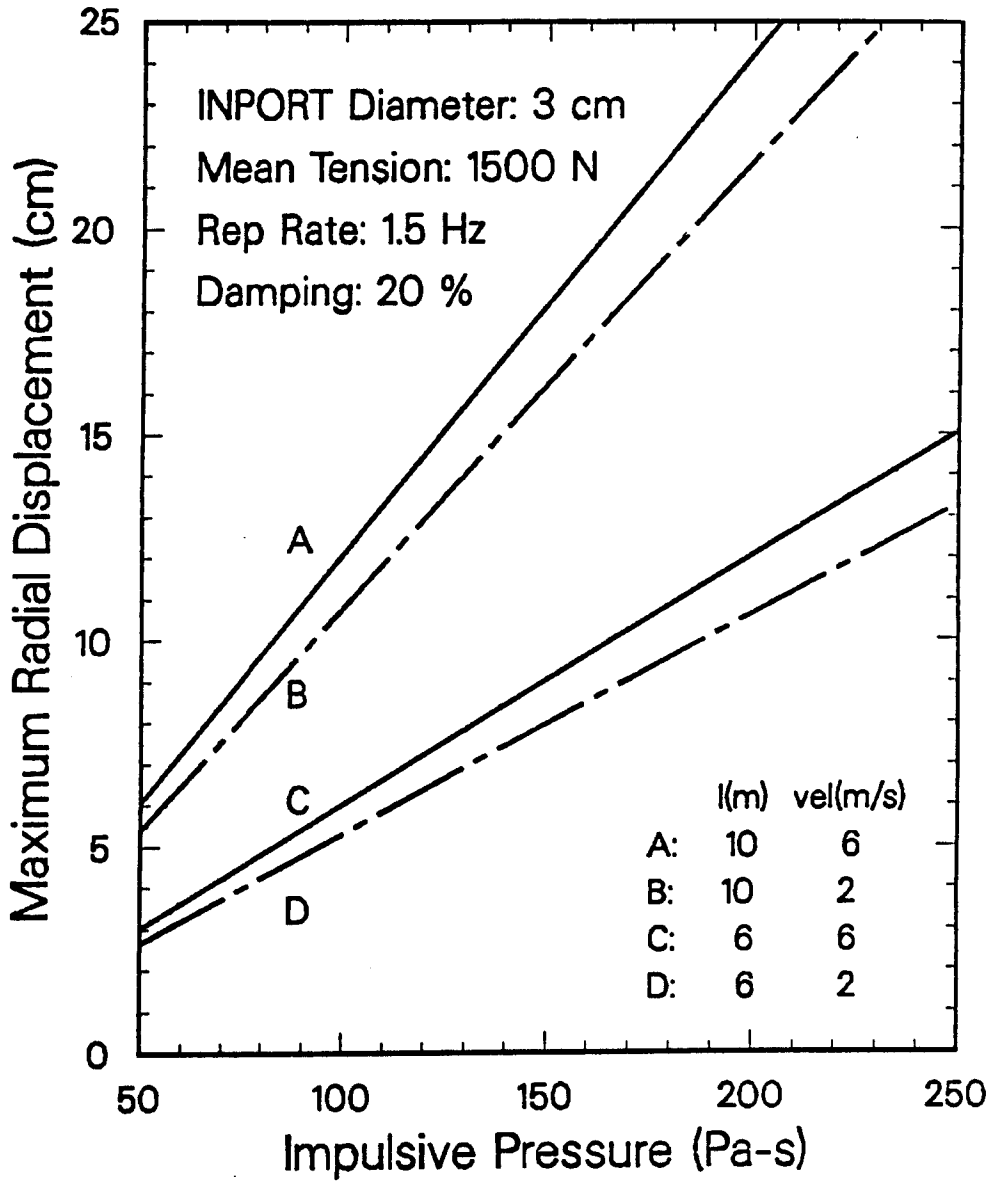


Fig. 4.18. Maximum dynamic displacement of INPORT tubes under a 1500 N mean tensile loading versus impulsive pressure.

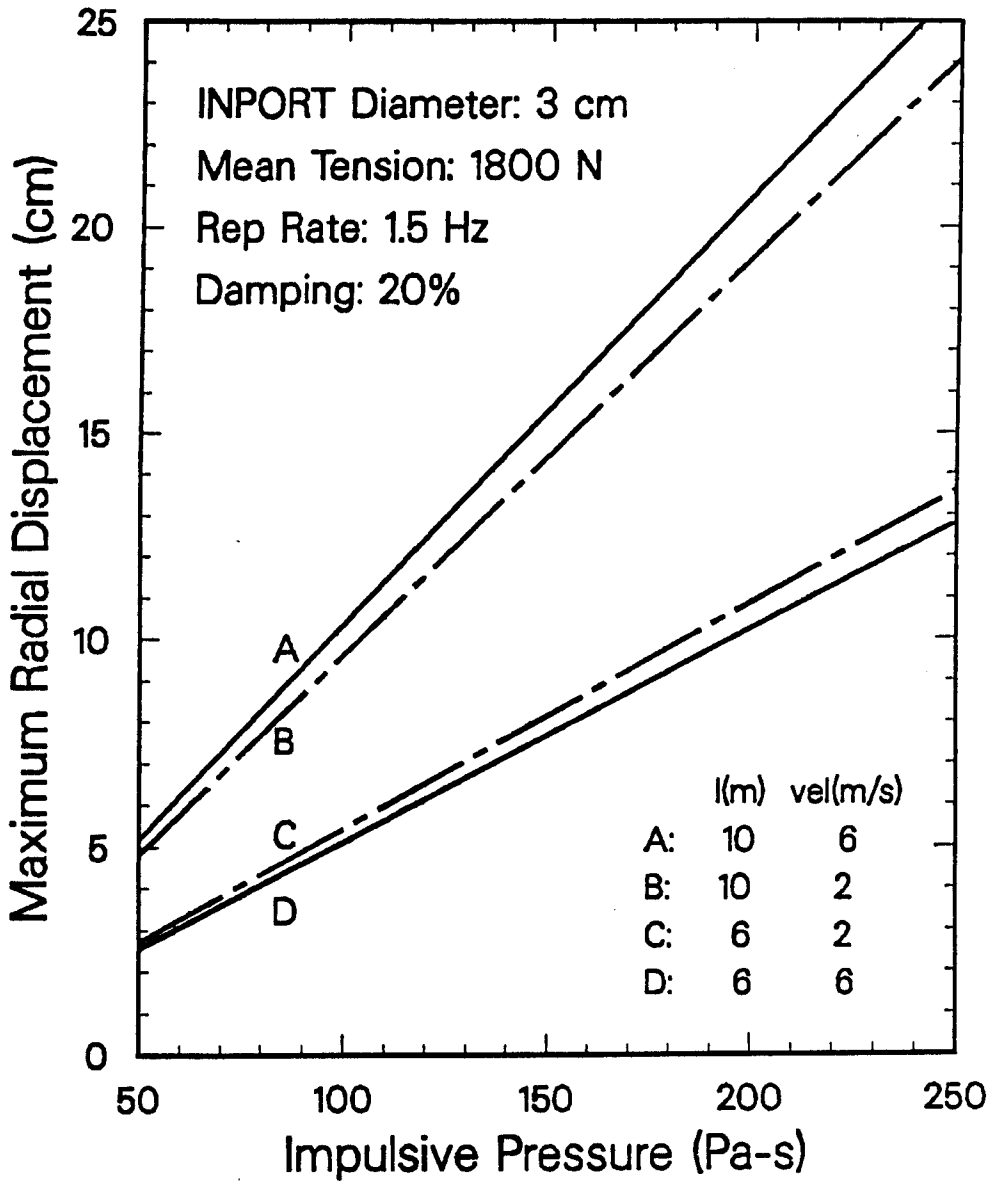


Fig. 4.19. Maximum dynamic displacement of INPORT tubes under a 1800 N mean tensile loading versus impulsive pressure.

following the impulse is effectively an ambient condition. From Fig. 4.14, the impulsive pressure is taken as 110 Pa-s. For a flow rate of 2 m/s, Figs. 4.18 and 4.19 show that the dynamic operating displacements of the INPORTs will be 5.8 cm and 6.0 cm at mean tensions of 1500 N and 1800 N, respectively.

It should again be emphasized that the response amplitudes depend upon a number of interacting dynamic parameters. The design curves provide a means of readily determining maximum displacements. The results indicate that INPORT placement allowing for 6 cm motion will not be a design problem for the smaller 3 m radius cavity.

## 4.6 Ion Beam Channel Parameters

The new driver parameters provided by PSI[1] require a reanalysis of the behavior of the plasma channels and the ion beams while they are in the channels. This has been done with the WINDOW computer code,[18] which has been described in previous reports. The beam ion that we have used for this study is 20 MeV $D^+$ and the channel length is 6 meters. A pulse width of 50 ns is assumed at the diode. A bunching factor of three over the length of the channel gives a pulse width of 17 ns at the target. The LIBRA design requires 240 TW on the target. Calculations have been done for channel radii of 0.5 cm and 1 cm.

The results of the WINDOW calculation for a 0.5 cm radius channel are shown in Fig. 4.20. Beam filamentation and ion energy loss are seen to provide the limits on the beam power. The optimum beam divergence is 0.1 radians and the maximum ion power is about 40 TW per channel. The window of propagation of the channel after the beam has been bunched is shown in Fig. 4.21, where it is seen that at 0.1 radians 70 TW can be transported. If we assume that the diode focal length is 1 meter, that the maximum source current densi-

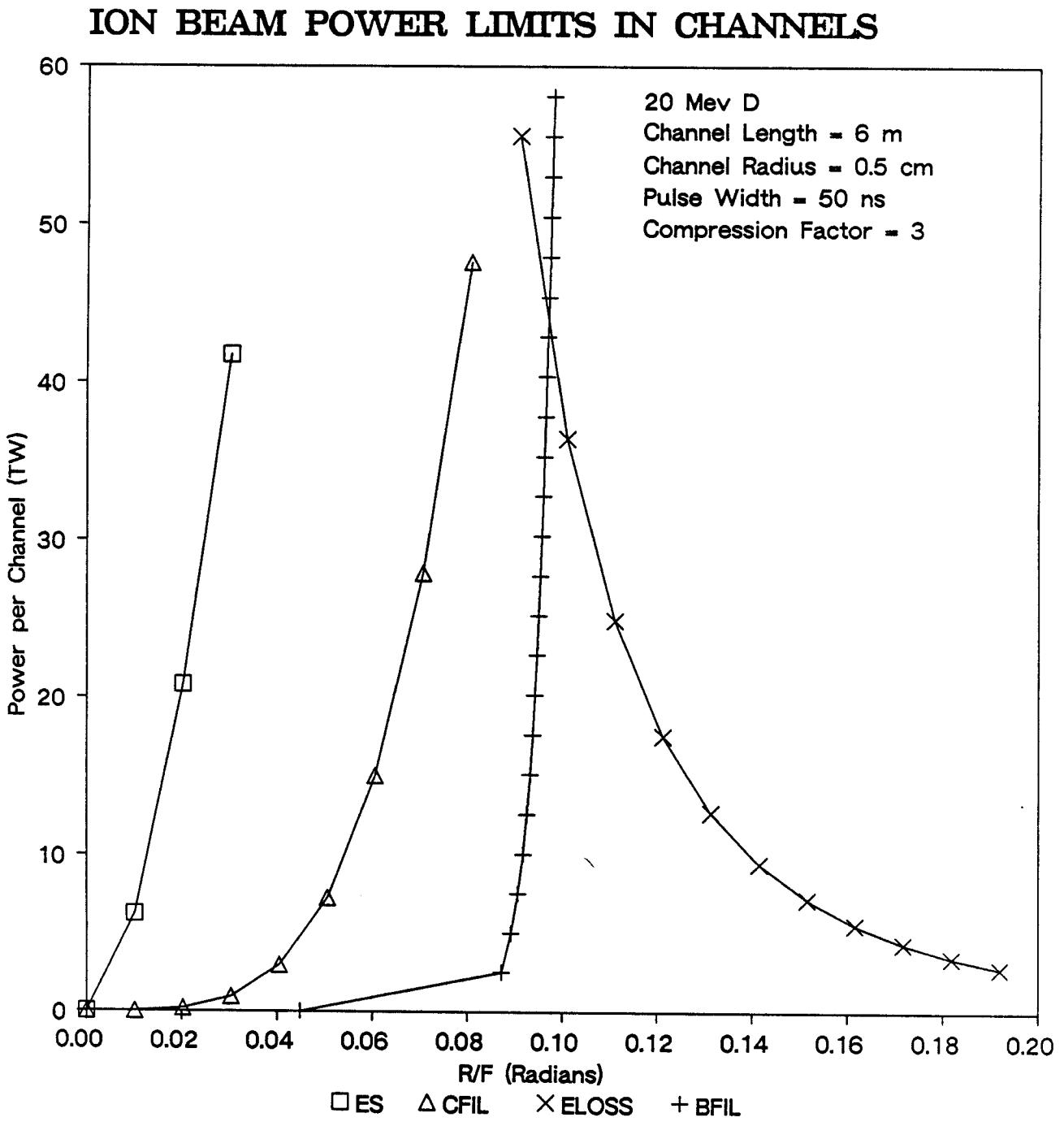


Fig. 4.20. Beam propagation at injection window for $D^+$ ions in a 6 meter long 0.5 cm radius channel.

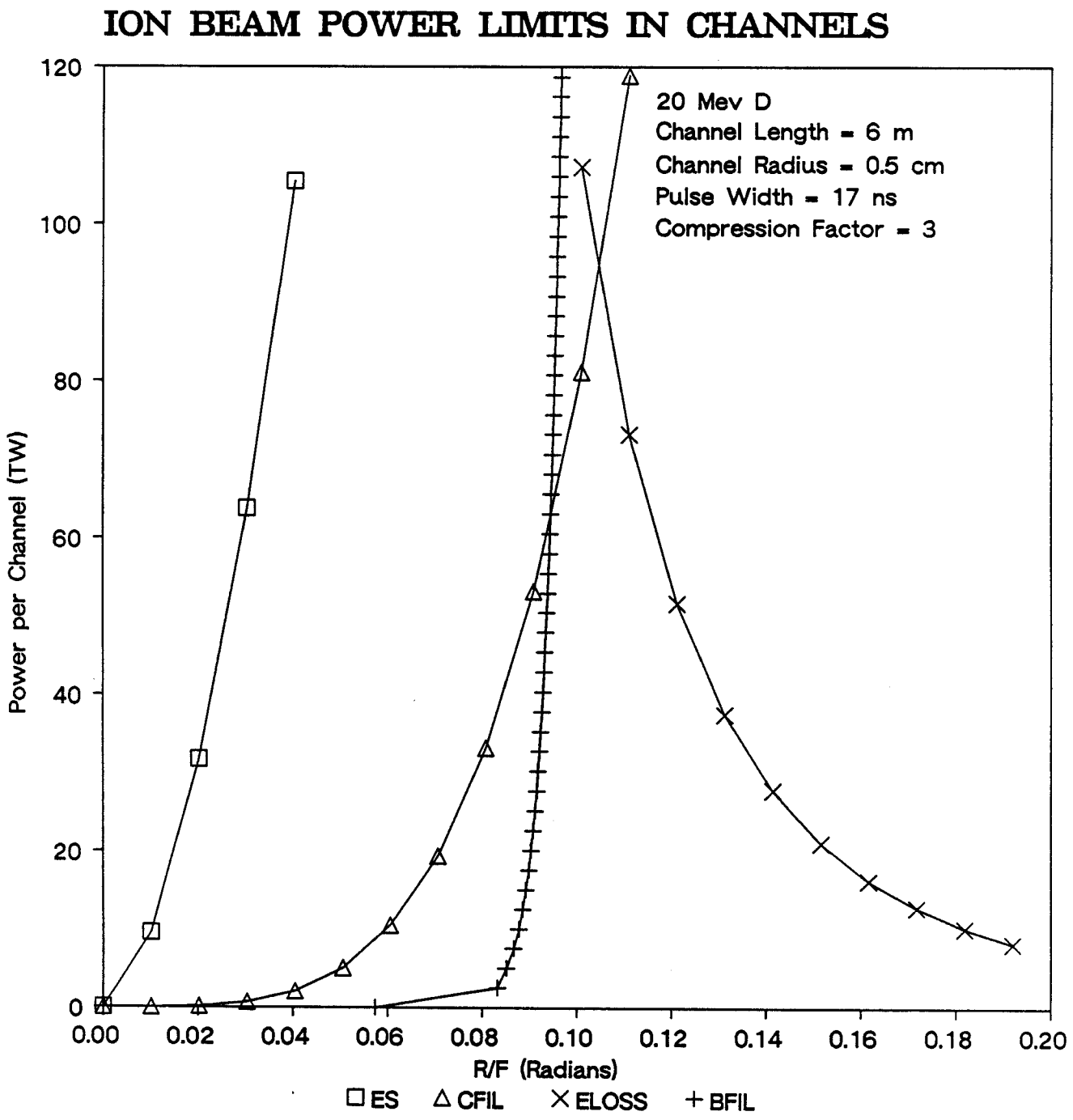


Fig. 4.21. Beam propagation window near the target for $D^+$ ions in a 6 meter long 0.5 cm radius channel.

ty is 5 kA/cm$^2$, and that 25% of the ion energy is lost during transmission, then each diode would need 44 cm$^2$ of anode surface. If the diode has an annular anode with a radius of 10 cm, the width of the annulus is 0.8 cm. The maximum total ion power on the target is 1680 TW, if 24 channels are present, where the transmission losses are not considered. If these losses are once again assumed to be 25%, the total power transmitted becomes 1260 TW, still much larger than the 240 TW required by the design.

The results for the 1 cm radius case are shown in Fig. 4.22. In this case, the beam power per channel is limited by beam filamentation, channel filamentation, and beam ion energy loss. The maximum power, 250 TW, occurs when the beam divergence is 0.13 radians. The situation after bunching is shown in Fig. 4.23, where it is seen that at 0.13 radians about 160 TW can be transported. The anode area required for this case is once again 44 cm$^2$ if one requires 13.3 TW per channel. The outer radius of the anode should be 13 cm for this case and the width of the annulus is 0.66 cm. In this case the maximum total transportable ion power is 3840 TW, far above the 240 TW called for in the LIBRA design. Even if the one assumes that 25% of the energy is lost, one could still transport 2880 TW.

Some simulations of channel behavior have been done with the Z-PINCH computer code.[19] The purpose of these is to determine the radius of the channels at the time of ion beam injection. Improvements to the Z-PINCH code have been made since the simulations presented in 1984[3] were completed, so they needed to be done again. The channels are formed by pre-ionizing a path with a laser in a 2.25 x $10^{-5}$ g/cm$^3$ argon gas with a 1% lithium impurity. The discharge current shown in Fig 4.24 is directed through this path by an unspecified means. The results of this simulation are show in Figs. 4.25 through

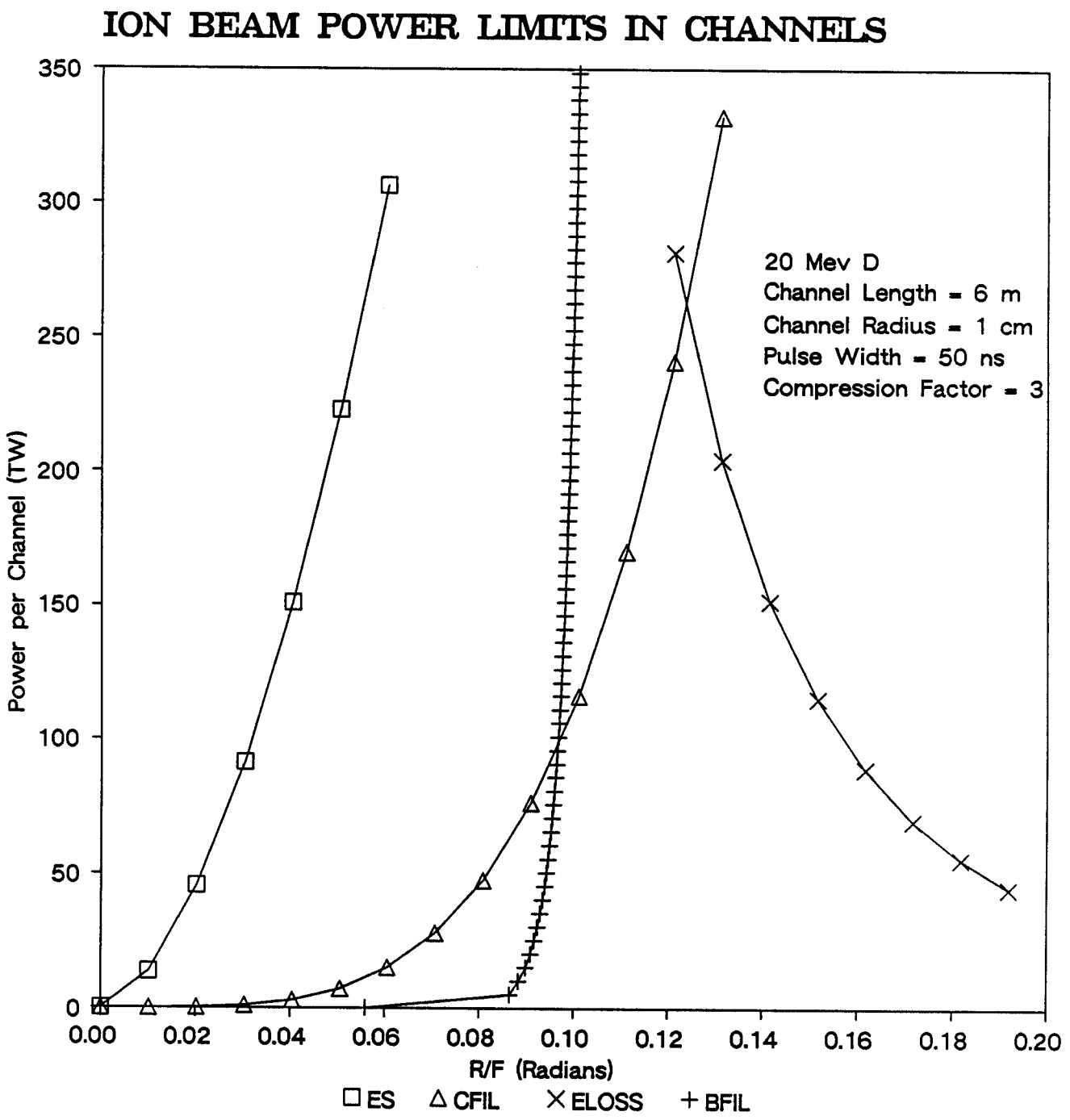


Fig. 4.22. Beam propagation window at injection for $D^+$ ions in a 6 meter long 1 cm radius channel.

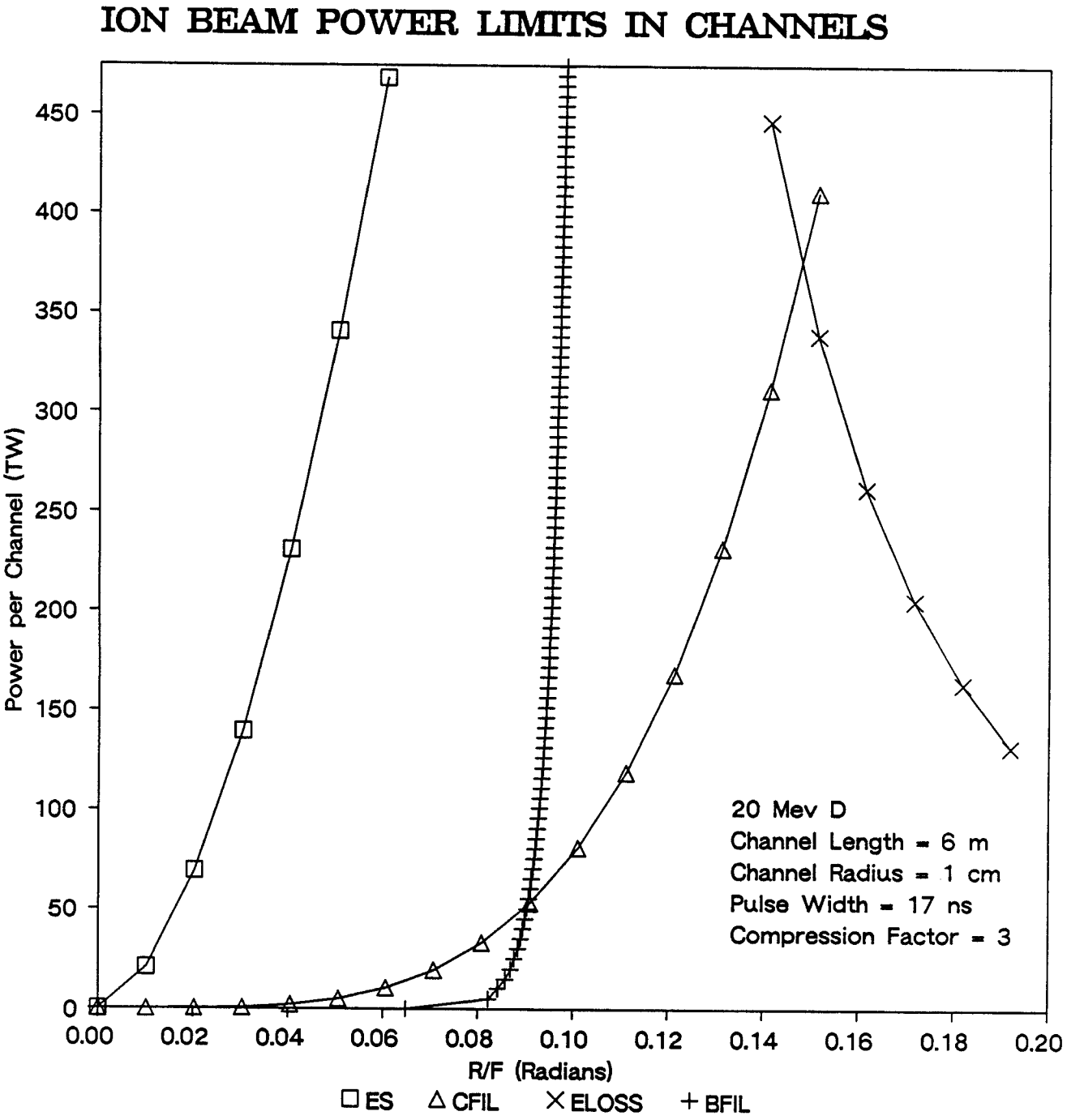


Fig. 4.23. Beam propagation window near the target for $D^+$ ions in a 6 meter long 1 cm radius channel.

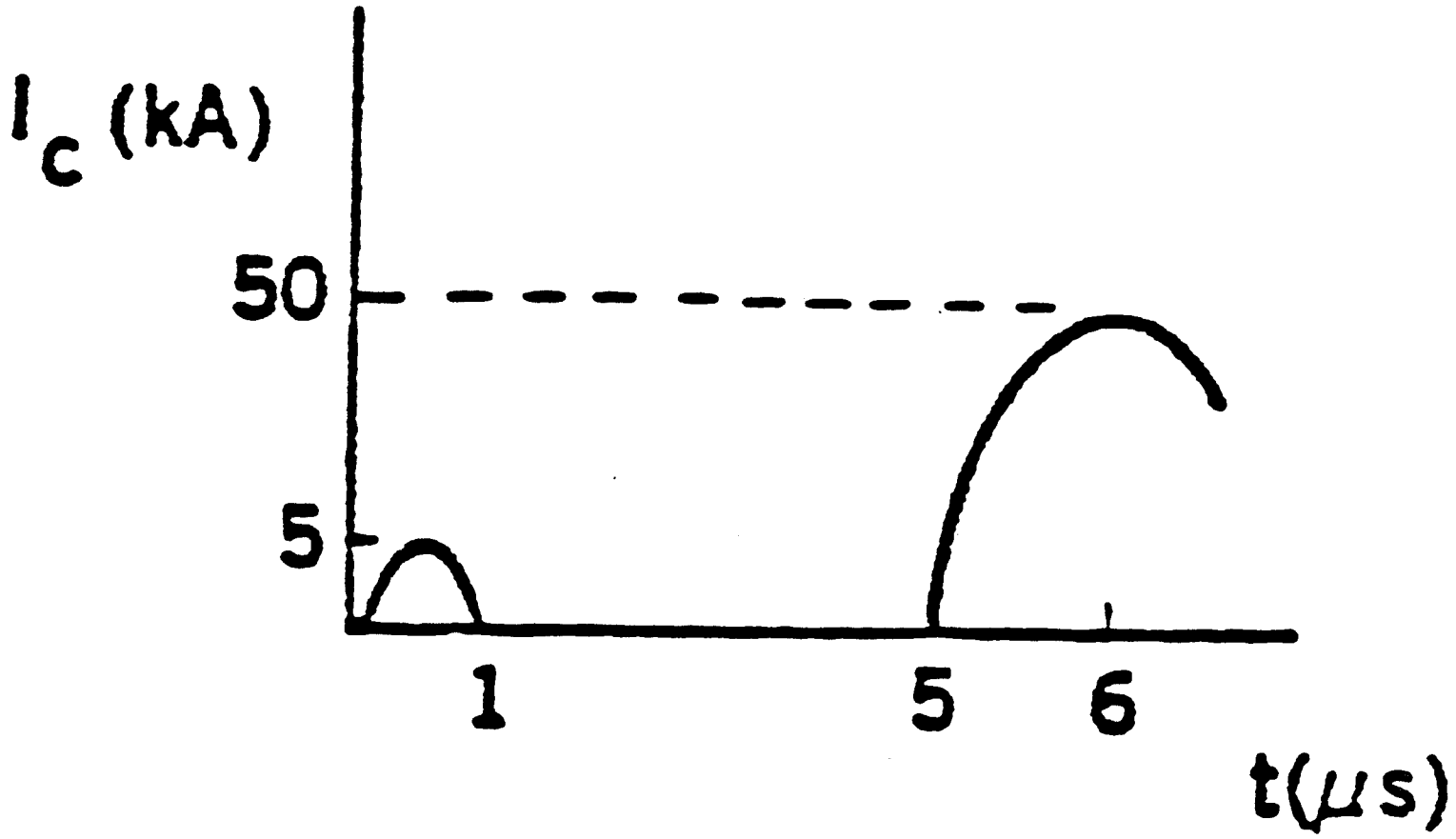


Fig. 4.24. Discharge current profile in LIBRA channels.

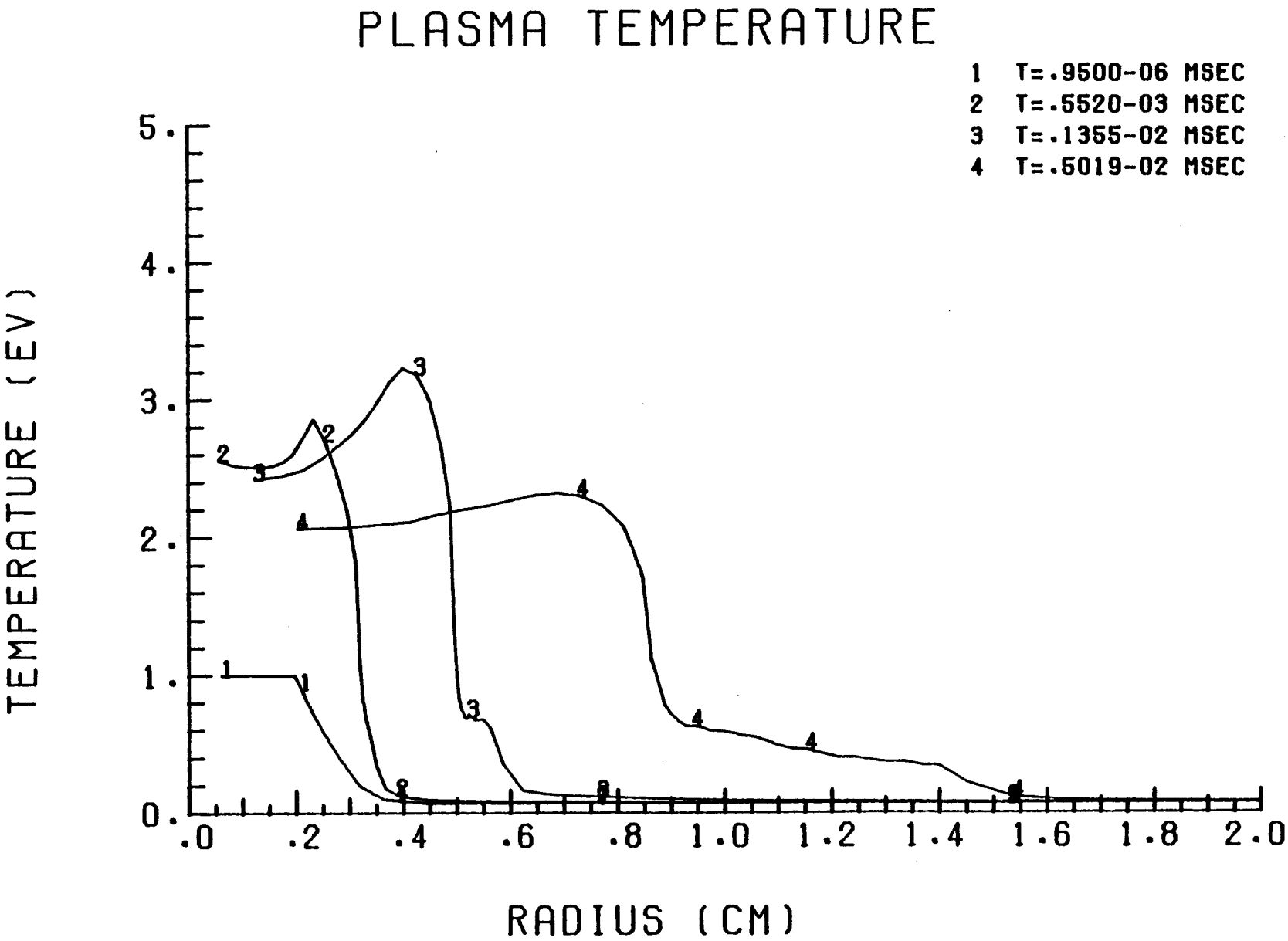


Fig. 4.25. Early plasma temperature profiles in LIBRA channels.

RUN ID = 3617

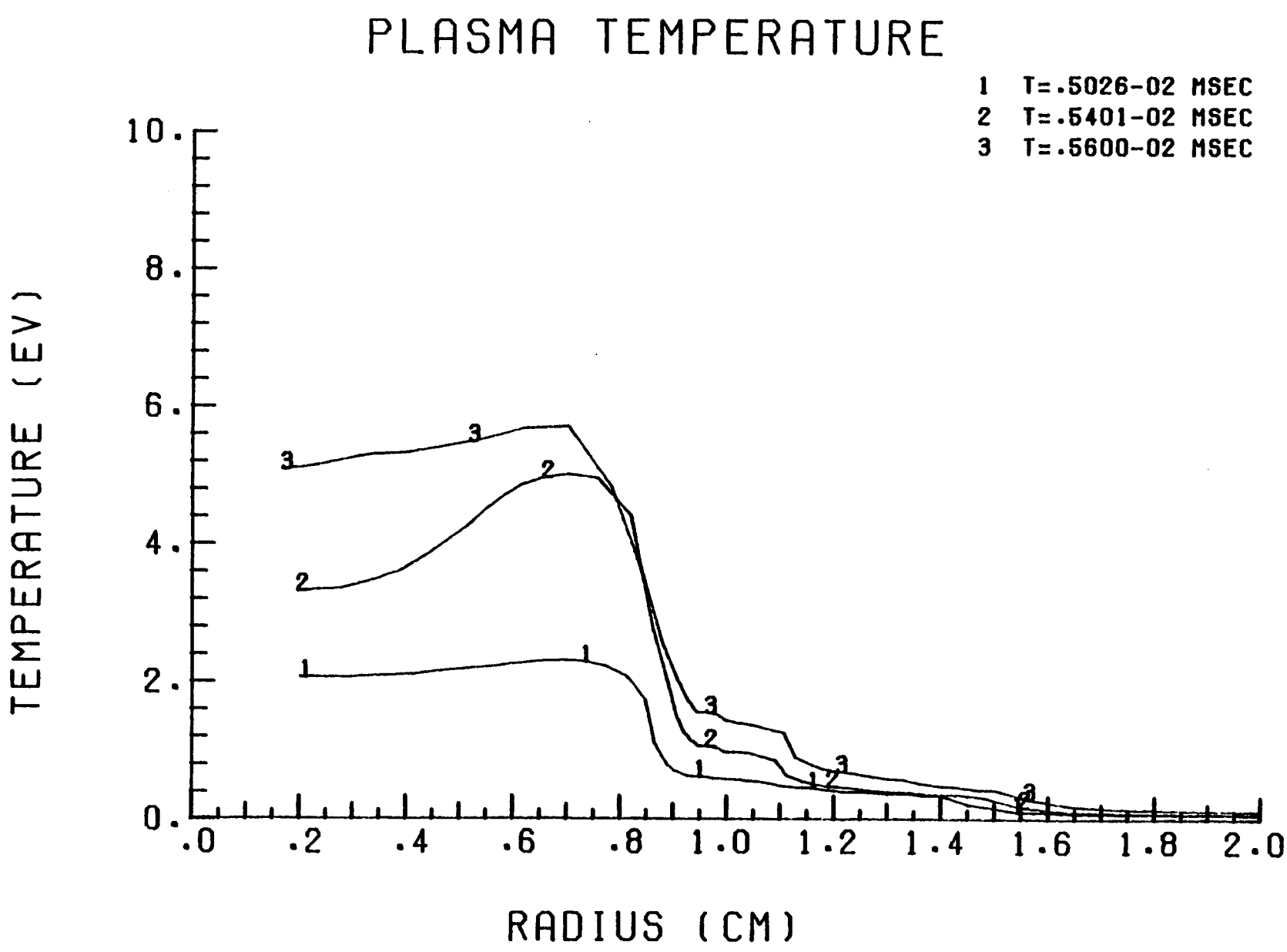


Fig. 4.26. Late plasma temperature profiles in LIBRA channels.

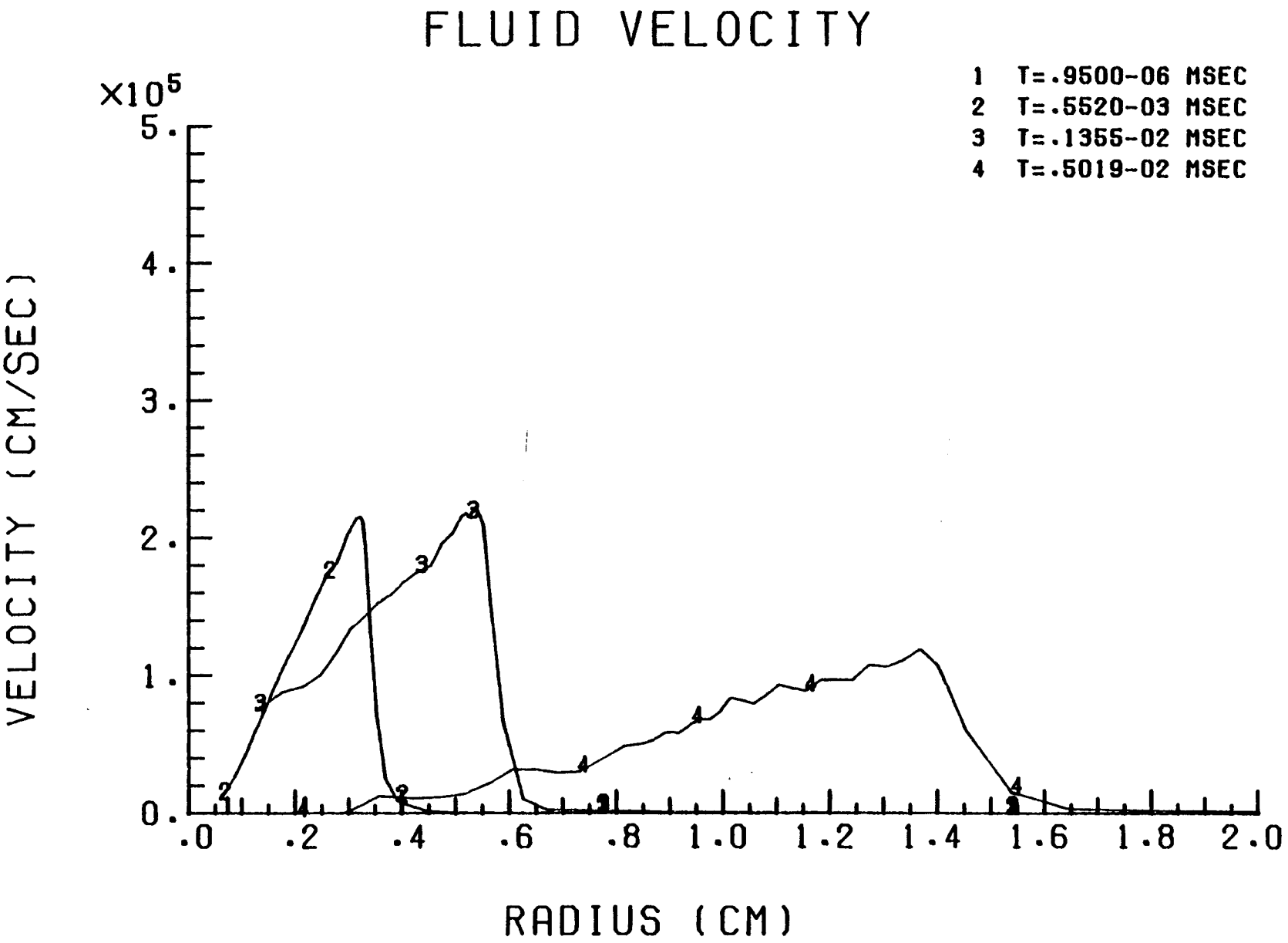


Fig. 4.27. Early fluid velocity profiles in LIBRA channels.

RUN ID = 3617

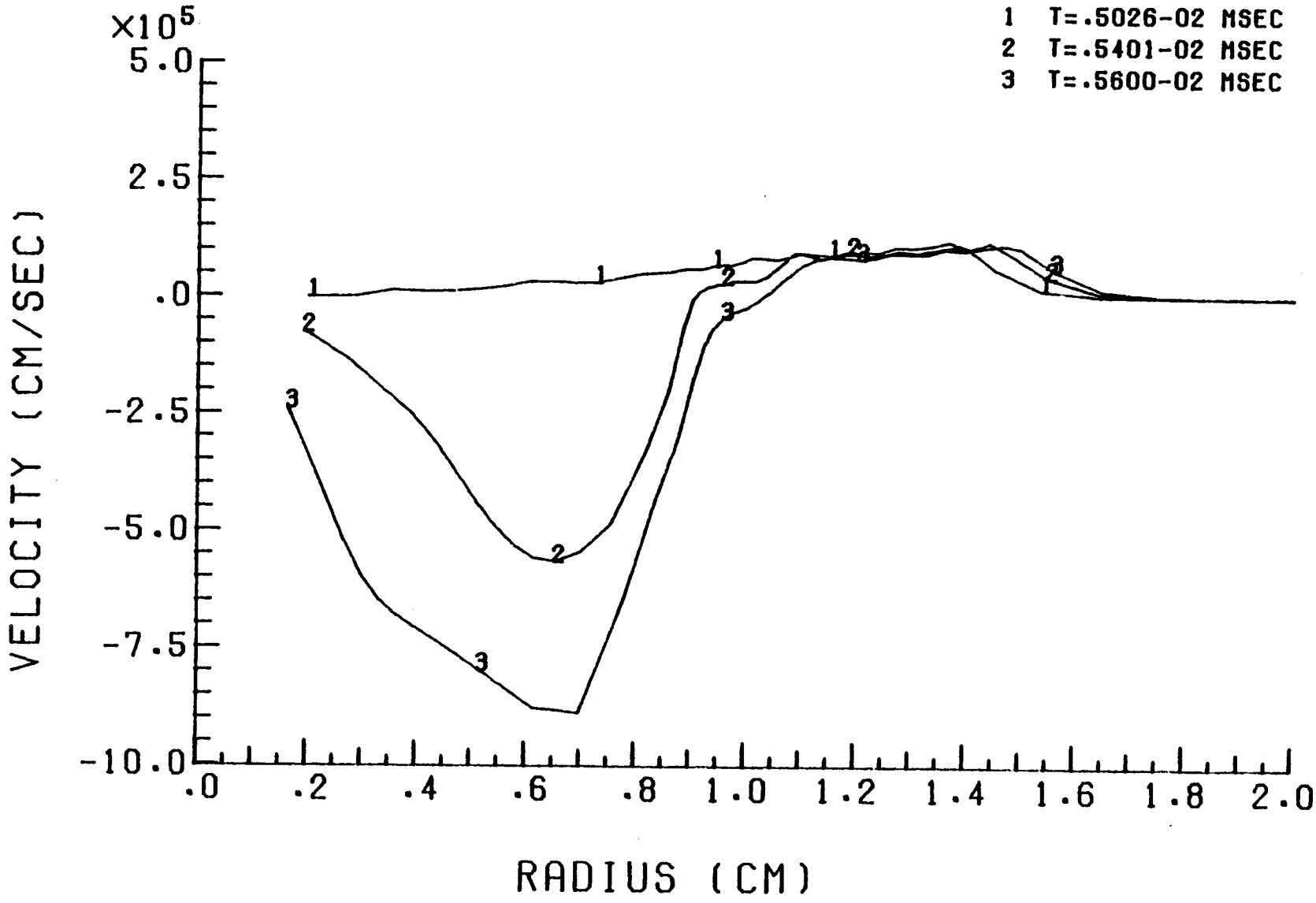


Fig. 4.28. Late fluid velocity profiles in LIBRA channels.

RUN ID = 3617

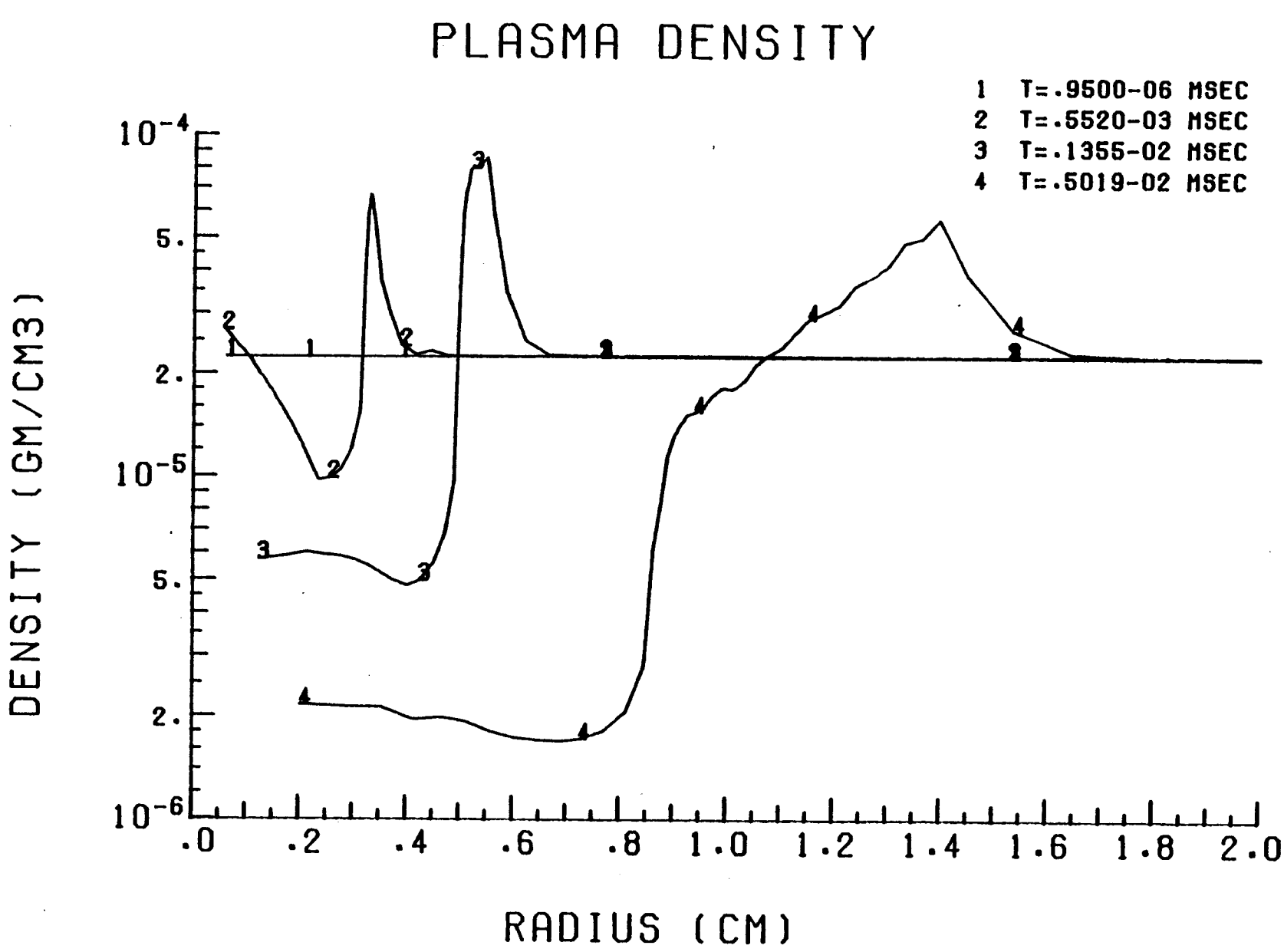


Fig. 4.29. Early plasma density profiles in LIBRA channels.

RUN ID = 3617

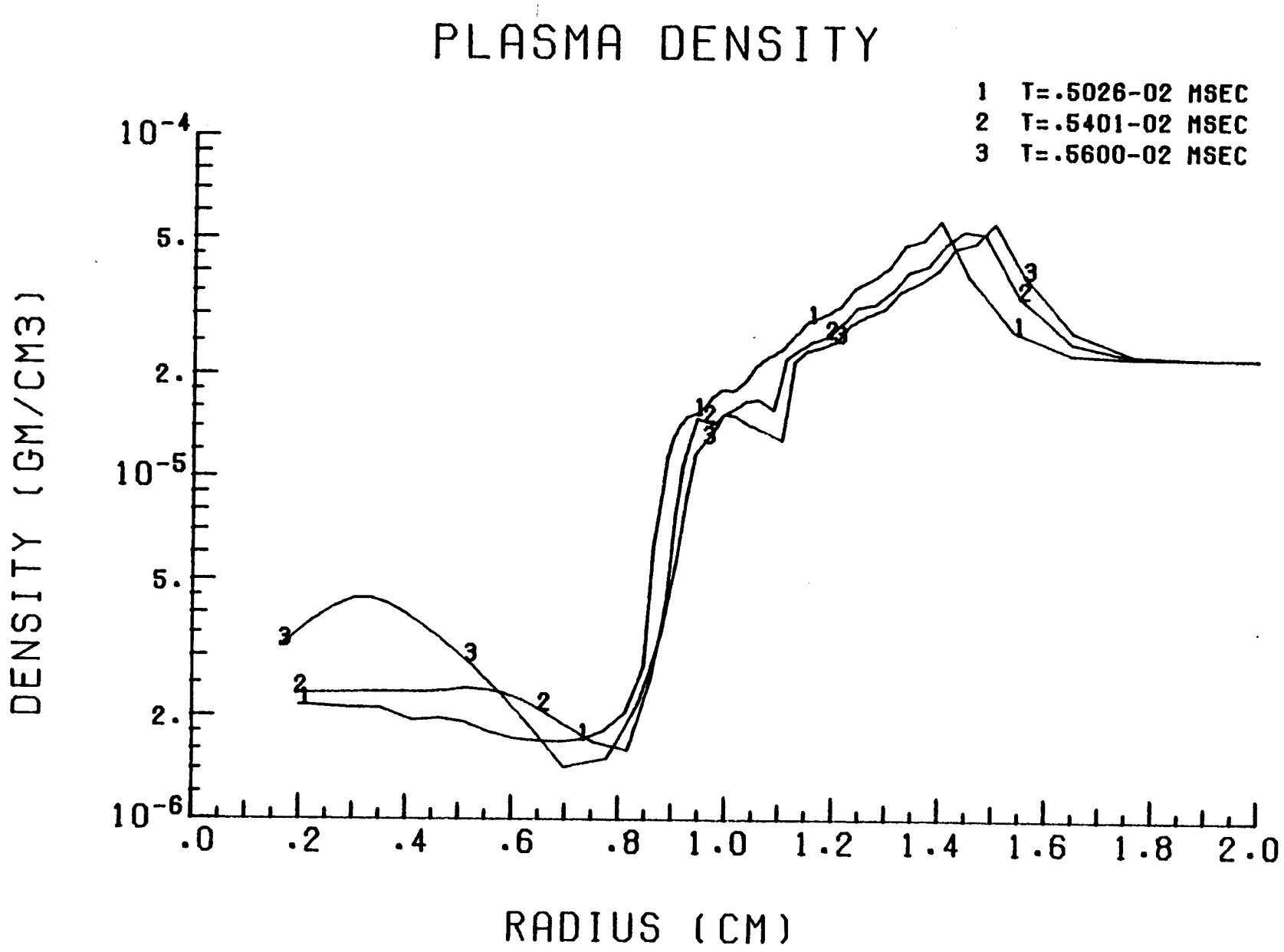


Fig. 4.30. Late plasma density profiles in LIBRA channels.

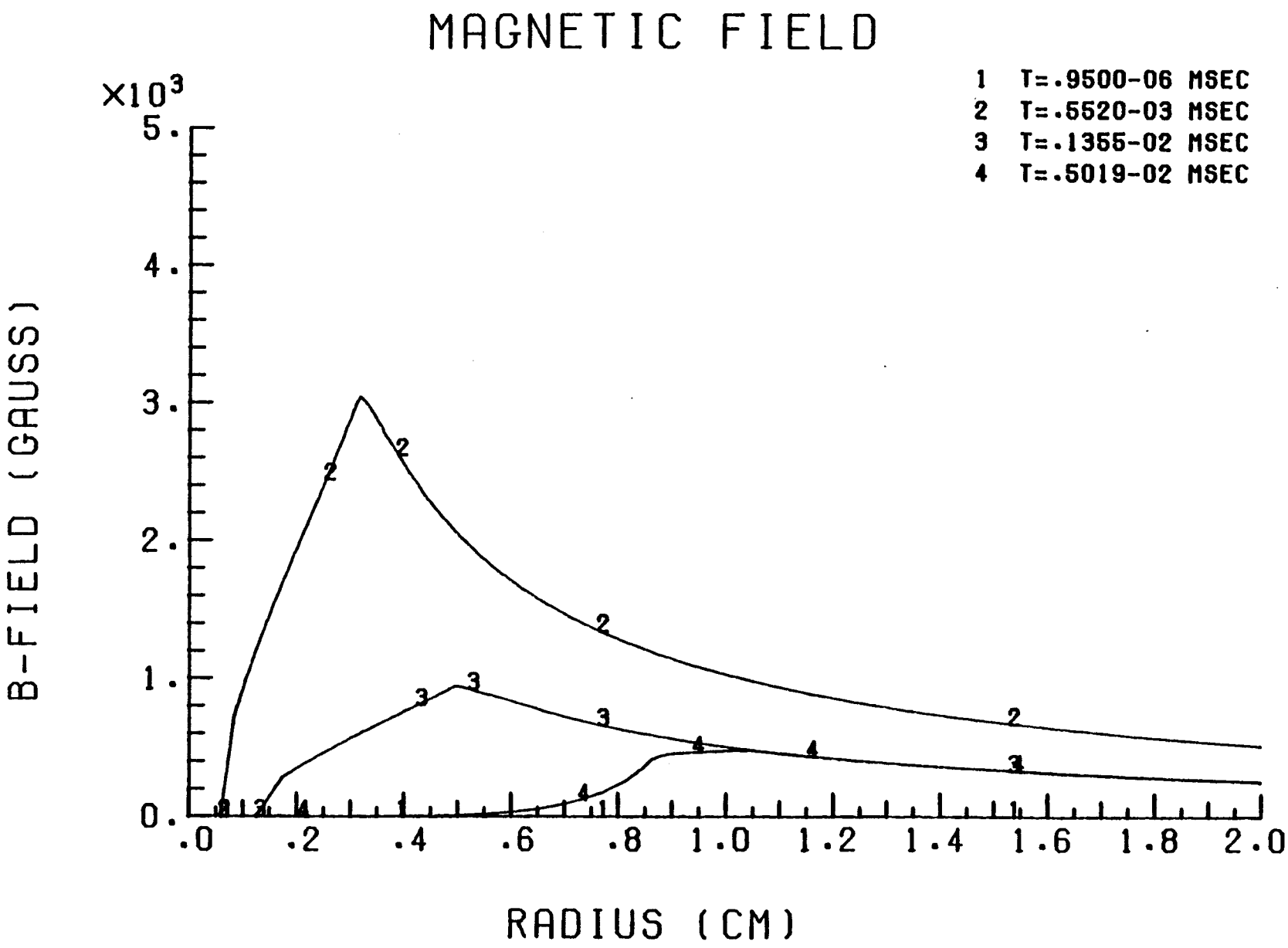


Fig. 4.31. Early magnetic field profiles in LIBRA channels.

RUN ID = 3617

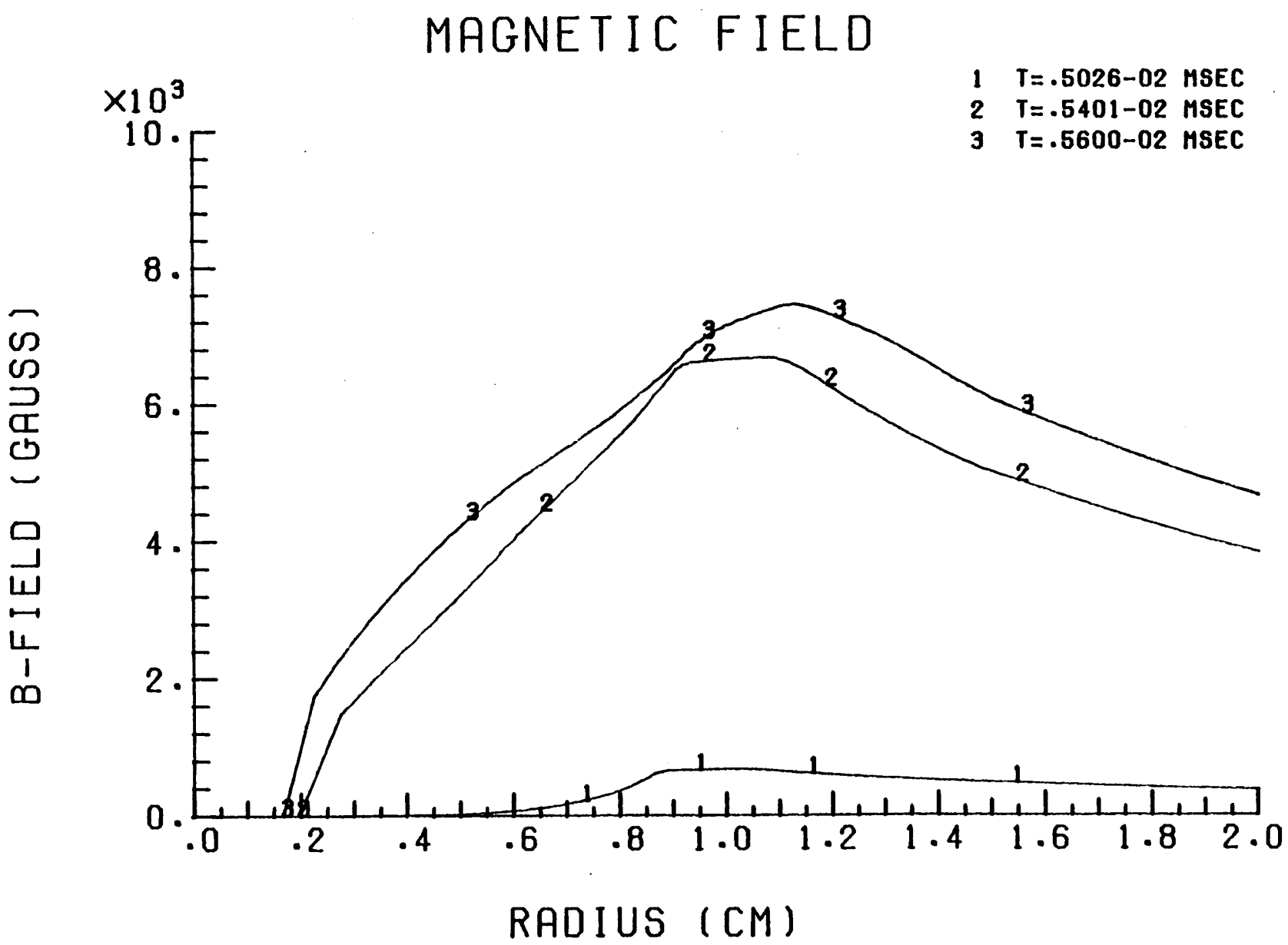


Fig. 4.32. Late magnetic field profiles in LIBRA channels.

RUN ID = 3617

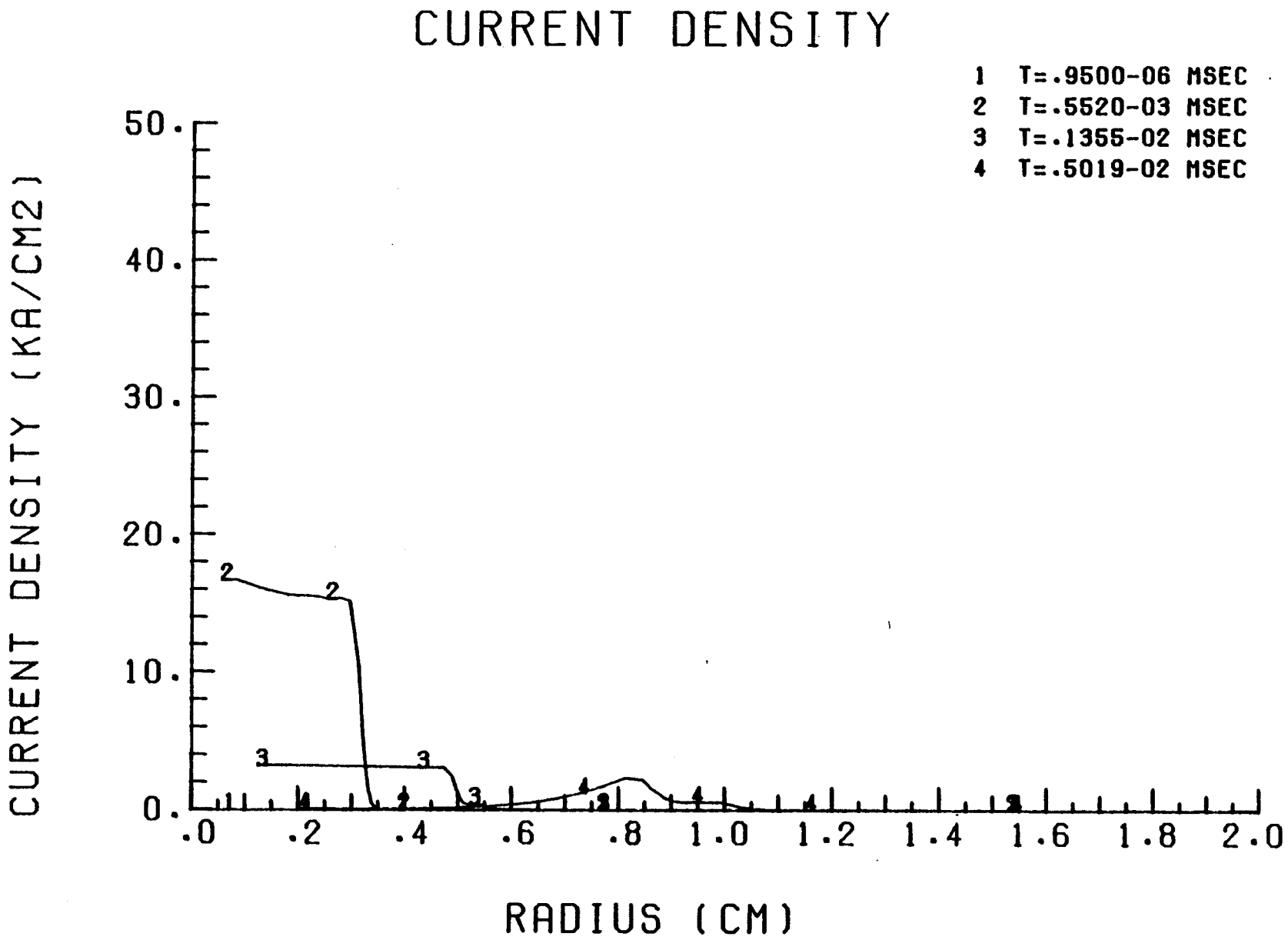


Fig. 4.33. Early discharge current density profiles in LIBRA channels.

RUN ID = 3617

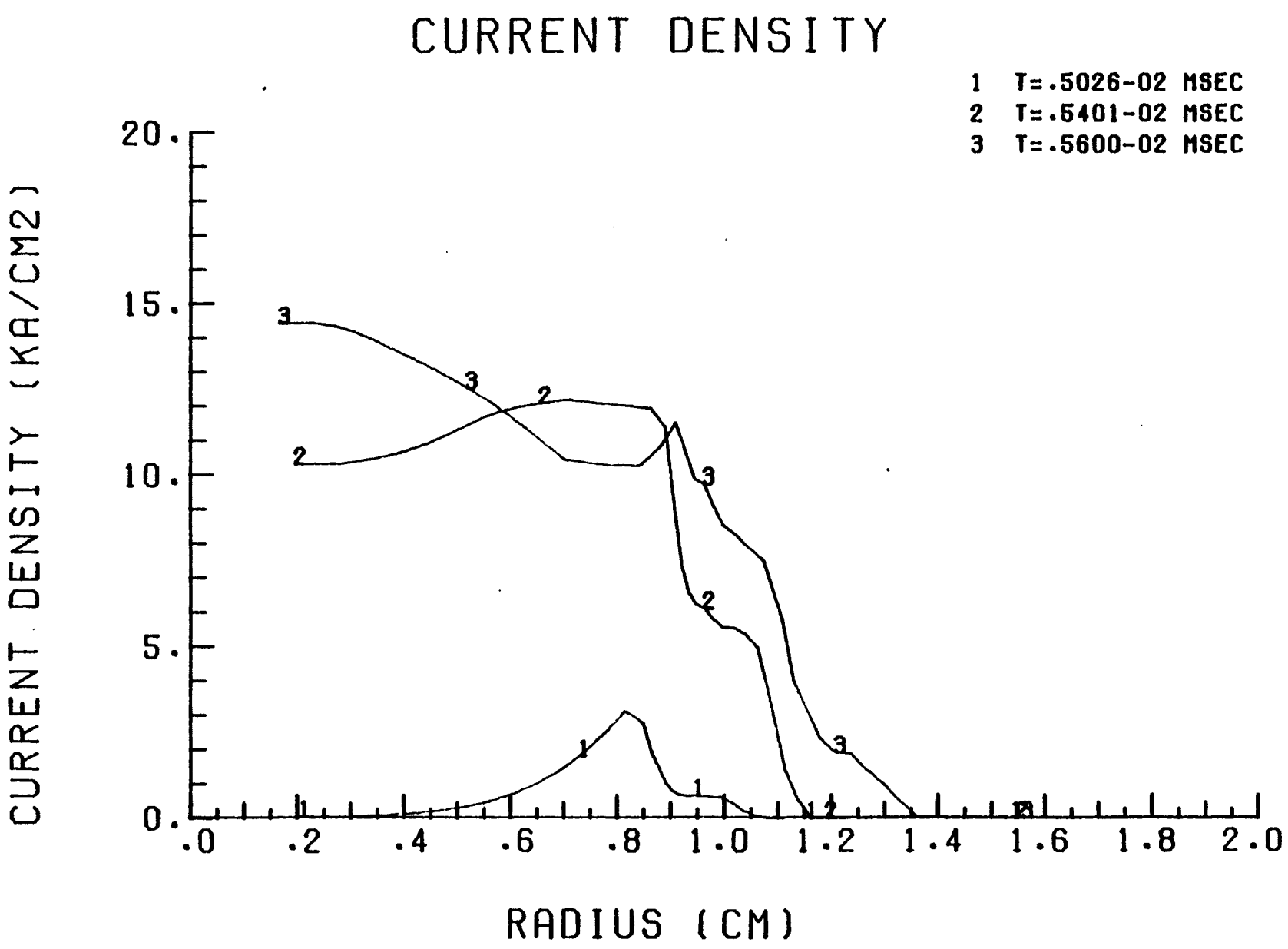


Fig. 4.34. Late discharge current density profiles in LIBRA channels.

RUN ID = 3617

4.34. The plasma temperature profiles, shown in Figs. 4.25 and 4.26, reach a maximum temperature of about 5 eV and fill a region out to about 0.8 cm in radius at 5.6 μs. The hydrodynamic motion is depicted through the fluid velocity, shown in Figs. 4.27 and 4.28, and the plasma mass density, shown in Figs. 4.29 and 4.30. It is seen in these figures that a region of gas out to 0.8 cm is rarefied by a factor of about 10 by a shock wave moving radially outward. The discharge current creates an azimuthal magnetic field, shown in Figs. 4.31 and 4.32. This magnetic field confines the beam ions. The magnetic field reaches a maximum at 5.6 μs and about 1 cm from the center of the channel. At 0.8 cm from the center of the channel, the magnetic field is 7 kG. The magnetic field profiles correspond closely with the discharge current density profiles, shown in Figs. 4.33 and 4.34. The basic conclusion of this simulation is that, if one can generate the current profile shown in Fig. 4.24, a channel 0.8 cm in radius can be formed. It is not known if such a current profile can be generated because of the high inductance of the channels themselves.

## References for Chapter 4


1. I. Smith, D. Garofalo, H. Nishimoto and W. Weseloh, "Design of a 20 MJ, 240 TW Ion Beam Driver for an Inertial Fusion Reactor," Pulse Sciences Inc. Report PSI-TR-224-1 (Sept. 1985).

2. G.A. Moses, R.R. Peterson, R.L. Engelstad, D.L. Henderson, G.L. Kulcinski, E.G. Lovell, I.N. Sviatoslavsky, J.J. Watrous, R.E. Olson, and D.L. Cook, "Preconceptual Design of the Light Ion Beam Fusion Target Development Facility," Transactions of the 11th Symposium on Fusion Engineering, Austin, TX (Nov. 1985).

3. B. Badger et al., "Annual Progress Report for the LIBRA Light Ion Fusion Reactor Project for the Period January - December 1984," Fusion Power Associates Report FPA-84-8 (Dec. 1984).

4. M. Sawan and J. Huang, Trans. Amer. Nucl. Soc. 44, 146 (1982).

5. R. O'Dell et al., "User's Manual for ONEDANT: A Code Package for One-Dimensional, Diffusion-Accelerated, Neutral Particle Transport," LA-9184-M, Los Alamos National Laboratory (1982).

6. R. MacFarlane, Trans. Amer. Nucl. Soc. 46, 271 (1984).

7. B. Badger et al., "HIBALL - A Conceptual Heavy Ion Beam Driven Fusion Reactor Study," University of Wisconsin Fusion Technology Institute Report UWFDM-450 (1981).

8. F. Katz, "Shock Wave Loading of the INPORT Tubes in LIBRA," Preliminary Report, Kernforschungszentrum Karlsruhe, October 1983.

9. W. Heilig and H. Reichenbach, "Measurements of the Unsteady Drag Coefficient of a Circular Cylinder"," Ernst Mach Institut.

10. V.J. Bishop and R.D. Rowe, "The Interaction of a Long Duration Friedlander Shaped Blast Wave with an Infinitely Long Right Circular Cylinder," AWRE Report No. O-38/67.

11. J.R. Banister and L.J. Vortman, "Effects of a Precursor Shock Wave on Blast Loading of a Structure," Report to the Test Director, October 1960, Sandia Corporation.

12. J. Penzien, "Experimental Investigation of the Blast Loading on an Idealized Structure," SC-2124(TR), 1959.

13. M.L. Merritt, "On the Effect of Slow Rise Times on the Blast Loading of Structures," AFSWP-460, Sept. 25 1953.

14. G.A. Moses, R.R. Peterson and T.J. McCarville, "MF-FIRE - A Multifrequency Radiative Transfer Hydrodynamics Code," Computer Physics Communications 36, 249-293 (1985).

15. B. Badger et al., "Annual Progress Report for the LIBRA Light Ion Fusion Reactor Project for the Period January-December 1983," Fusion Power Associates Report FPA-83-8 (Dec. 1983).

16. G. Taylor, "The Formation of a Blast Wave by a Very Intense Explosion - I. Theoretical Discussion," Proc. R. Soc. A201, 169 (1950).

17. M. Uesaka, R.R. Peterson and G.A. Moses, "Equilibrium and Non-Equilibrium Microfireball Behavior in Light-Ion Fusion Systems," Nucl. Fusion 24, 1137 (1984).

18. R.R. Peterson, "WINDOW - A Code to Compute Ion Beam Power Constraints," Fusion Power Associates Report FPA-84-6 (Dec. 1984).

19. J.J. Watrous, G.A. Moses and R.R. Peterson, "Z-PINCH - A Multifrequency Radiative Transfer Magnetohydrodynamics Computer Code," University of Wisconsin Fusion Technology Institute Report UWFDM-584 (June 1984) (Revised March 1985).

## 5. SUMMARY

Progress has been made in ion stopping calculations, to the Z-PINCH computer code and to the LIBRA reactor concept. Improvements have been made to the MEDUSA and Z-PINCH computer codes and the improved versions of these codes as well as the DKR radioctivity code have been given to KfK. The LIBRA reactor concept has evolved into a form with a smaller reactor cavity and optional configuration that would allow pulse shaping.

Dr. Goel's nine month visit to Madison has led to a very fruitful study of the interaction of ion beams and thin foil targets. The MEDUSA code was compared with the PHD-IV code and improvements were made to the ion stopping physics in both. They were both also compared with computational results from NRL. With the confidence that was thus gained in the codes, the experimental conditions in KALIF were simulated.

The LIBRA reactor concept has improved over the last year. Moving the diodes closer to the target increased our confidence in the ability to create the plasma channels. It also reduced the energy lost by the ion beams while they are in the channels. The reduction in the lengths of the channels was only possible because it was found that a smaller reaction chamber will perform at least as well as the larger one. The design of the pulsed power modules has allowed us for the first time to include them in the layout of the design. We have investigated an optional layout that could provide a better pulse shape.